Anyuan Chen

Investigation of Permanent Magnet Machines for Downhole Applications

– Design , Prototype and Testing of a Flux-Switching Permanent Magnet Machine

Thesis for the degree of Philosophiae Doctor

Trondheim, January 2011

Norwegian University of Science and Technology
Faculty of Information Technology,
Mathematics and Electrical Engineering
Department of Electric Power Engineering

NTNU – Trondheim
Norwegian University of
Science and Technology

NTNU
Norwegian University of Science and Technology

Thesis for the degree of Philosophiae Doctor

Faculty of Information Technology, Mathematics and Electrical Engineering
Department of Electric Power Engineering

ISBN 978-82-471-2563-2 (printed ver.)
ISBN 978-82-471-2564-9 (electronic ver.)
ISSN 1503-8181

Doctoral theses at NTNU, 2011:23

Printed by NTNU-trykk

Acknowledgments

The time, from Sep. 2006 to Sep. 2010, spent at the Energy Conversion Group (ENO) will always be one of the most memorable parts of my life. It is the time to finish my four-year PhD study, now I would like to express my gratitude to the people who have helped me in various ways with the research and a pleasant stay at NTNU and in Norway.

First of all, I would like to thank my supervisor Prof. Robert Nilssen for his supervision, guidance and other help throughout the period of my study, particularly for the arranged bicycle trips around Trondheim and the car trip to his hometown Florø that have given me unforgettable experiences.

I would also like to thank my co-supervisor Prof. Arne Nysveen, who not only spared time for reading my papers, provided many good suggests to my thesis, and also financed the machine prototype and two conference trips.

Thank also goes to Prof. Tore Undeland, Prof. Lars Norum and Prof. Marta Monilas for the exchanging ideas and good suggestions to my research during ENOFF seminars.

I would also like to express my gratitude to the fellow PhD candidates Ravindra Ummaneni (now my colleague at Smartmotor) for helping me in all possible ways during my study period, particularly to Nathalie Holtsmark and Muhammud Jafar for the helpful comments on the thesis language. Others at the department I would like to acknowledge for building prototype machine are Oddvar Lamdrø and Vladimir Klibicka.

Finally, I would like to express my heartfelt thanks to my wife, Shelley, who encouraged me to take master education in Sweden and continued to support my PhD study at NTNU. She spent lots of time to take care of our lovely daughter Julia and son Christopher during my study period. Without her supports, I could never have finished my PhD study. I also thank our children for bringing our family lots of pleasure all the time.

Anyuan Chen

Anyuan Chen

陈安源

Trondheim, 03 Jan. 2011

Abstract

The current standard electrical downhole machine is the induction machine which is relatively inefficient. Permanent magnet (PM) machines, having higher efficiencies, higher torque densities and smaller volumes, have widely employed in industrial applications to replace conventional machines, but few have been developed for downhole applications due to the high ambient temperatures in deep wells and the low temperature stability of PM materials over time. Today, with the development of variable speed drives and the applications of high temperature magnet materials, it is increasingly interesting for oil and gas industries to develop PM machines for downhole applications.

Recently, some PM machines applications have been presented for downhole applications, which are normally addressed on certain specific downhole case. In this thesis the focus has been put on the performance investigation of different PM machines for general downhole cases, in which the machine outer diameter is limited to be small by well size, while the machine axial length may be relatively long. The machine reliability is the most critical requirement while high torque density and high efficiency are also desirable. The purpose is to understand how the special constraints in downhole condition affect the performances of different machines.

First of all, three basic machine concepts, which are the radial, axial and transverse flux machines, are studied in details by analytical method. Their torque density, efficiency, power factor and power capability are investigated with respect to the machine axial length and pole number. The presented critical performance comparisons of the machines provide an indication of machines best suitable with respect to performance and size for downhole applications.

Conventional radial flux permanent magnet (RFPM) machines with the PMs on the rotor can provide high torque density and high efficiency. This type of machine has been suggested for several different downhole applications. Flux-switching PM (FSPM) machines, which have the PMs located on the stator and are therefore more reliable, can theoretically also exhibit high torque density and relatively high efficiency. This thesis has put an emphasis on studying this type of machine. Two FSPM machines have been investigated in detail and compared by analytical method, FEM simulation and prototype measuremens. Their operating principle and important design parameters are also presented.

A lumped parameter magnetic circuit model for designing a high-torque FSPM machine is newly introduced and the designed machine is verified by FEM simulations. A prototype machine with an outer diameter of 100 mm and an axial length of 200 mm is built in the laboratory and tested at room temperature. Based on that, the machine performance at an ambient temperature of 150°C is also predicted. The results show that the FSPM machine can provide a high torque density with slight compromise of efficiency and power factor.

Choosing a proper machine type is significantly dependent on the application specifications. The presented results in this thesis can be used as a reference for selecting the best machine type for a specific downhole case.

Publications generated by the PhD research work

Anyuan Chen, Robert Nilssen and Arne Nysveen, "Performance comparisons among radial flux, multi-stage axial flux and three-phase transverse flux PM machines for downhole applications", *IEEE Trans. Ind. Appl.*, vol 46, No.2, pp 779-789, March/April 2010.

Anyuan Chen, Ummaneni, R.B., Nilssen, R., Nysveen, A. " Review of electrical machine in downhole application and the advantages", in the proceeding of *EPE-PEMC 2008*, 1-3 Sep., 2008, Poznan, Poland.

Anyuan Chen, Robert Nilssen and Arne Nysveen, "Harmonic Analysis and comparison of the back EMFs of Four Permanent Magnet Machine with Different Winding Arrangements", in the proceeding of *ICEMS2008*, 17-20, OCT., 2008, Wuhan, China.

Anyuan Chen, Robert Nilssen and Arne Nysveen, "Performance comparisons among radial flux, multi-stage axial flux and three-phase transverse flux PM machines for downhole applications", in the proceeding of *IEMDC2009*, 6-9, May,2009, Miami, USA.

Anyuan Chen, Njål Rotevatn, Robert Nilssen and Arne Nysveen, "Characteristic Investigations of a New Three-Phase Flux-Switching Permanent Magnet Machine by FEM Simulations and Experimental Verification" in the proceeding of *ICEMS2009*,15-18, Nov., 2009 Tokyo, Japan.

Anyuan Chen, Robert Nilssen and Arne Nysveen, "Analytical design of a high-torque Flux-Switching Permanent magnet machine by a Simplified Lumped parameter magnetic circuit model", in the proceeding of *ICEM 2010*, 6-8, Sep. 2010, Rome, Italy.

Anyuan Chen, Robert Nilssen and Arne Nysveen, "Investigation of a Three-Phase Flux-Switching Permanent Magnet Machine for Downhole Applications ", in the proceeding of *ICEM 2010*, 6-8, Sep. 2010, Rome, Italy

Contents

1. Introduction

Energy is the driving force of the global economy. Fig. 1-1 shows the predicted energy requirement from different resources to ensure the development of the global economy from now to 2030[7]. As can be seen from the figure, oil and gas still remain the most important source in the coming decades since the development of renewable resources is not progressing as fast as anticipated. It also takes time for the transfer of the knowledge and experience combined with the industrial capability. The World Energy Technology and climate policy Outlook (WETO2030) projects that world oil production will increase by 65% and gas production will double in 2030 referring to the production in 2000. The situation today is that the total oil production from currently producing fields in the world is declining as shown in the blue area in Fig. 1-2, in which the grey area represents the oil that should be further developed to ensure security of energy supply. How to find and develop the required oil to ensure security of energy supply is a challenge for oil and gas industries today.

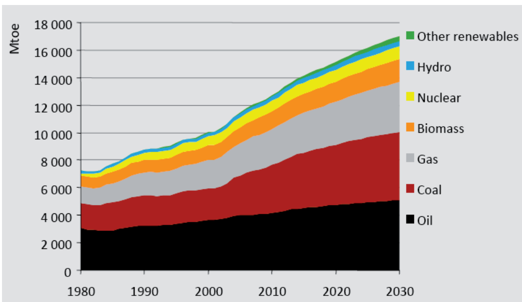

Fig. 1-1 Predicted energy requirement from different energy sources [7]

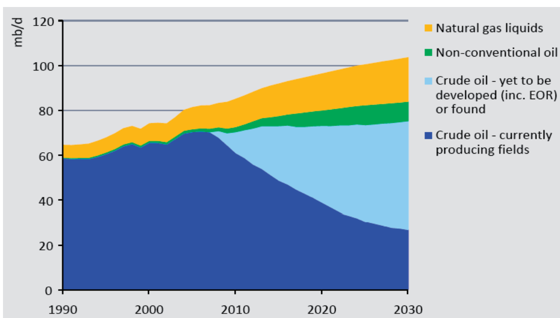

Fig. 1-2 Oil and gas production from current fields and to be developed [7]

1.1 Main sources for more oil and gas

The majority of the increased production of oil and gas in coming decades is from the following two sources [8] [10].

1.1.1 Getting more from "mature fields" in production

These "mature fields" today account for over 70% of the worldwide oil and gas production. The production is gradually declining and the fields will be shut down prematurely if technologies for improving recovery and cost effective operation and maintenance are not put in place. It should be noted that on the worldwide basis a 1% improved recovery provides approximately two-year energy consumption. It is expected that innovative and cost effective technologies should be developed to substantially increase the rate of recovery from today's average of 35% to over 50% for oil and 75% for gas, optimize the efficiency of operation and maintenance while minimizing the environmental impact.

1.1.2 Exploitation of deep and ultra deep offshore reservoirs

A study made by Institut Français du Pétrole (IFP) concluded that 40% of the offshore oil & gas would come from water depths up to 500 m, 20% between 500 and 1500 m and 40% from 1500 to 3000 m. Until 2000, a mere 2% of prospective resources had been explored in deep and ultra deep waters. The global oil and gas hunt for new oil and gas resources is leading us into ever deeper waters and harsher environments. The accelerating trend of the deep reservoirs exploitation is shown in Fig. 1-3.

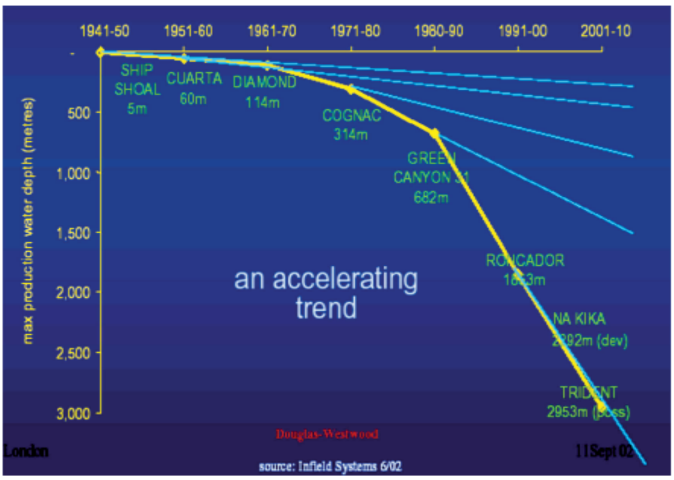

Fig. 1-3 Deep oil and gas development [8]

How to exploit more oil and gas resources in the deepwater and develop them in a safe, efficient and more environmentally friendly way is a challenge. The cost of traditionally fixed or floating facilities for processing, which are today widely used, increases significantly because the platforms are very expensive to build and install, and for the fixed platforms demounting also costs hundreds of millions dollars afterwards. With the conventional technologies many deepwater fields may therefore be uneconomical to develop. Downhole processing, by moving the processing from topside or onshore to downhole can not only eliminate the top platforms or partly reduce the top area, but also generally improve production, ultimate recovery and processing efficiency whilst decreasing environmental impact [8].

With the increase of the seawater depth, the downhole temperature and pressure increase. To help identifying high pressure and high temperature (HPHT) operating environments, safe operating envelopes and technology gaps, HPHT conditions are segmented into 3 tiers defined by reservoir temperatures and pressures as shown in Fig. 1-4. Most HPHT operations to date have taken place under tier I conditions, pressures up to 15,000 psi (1034 bar) and temperatures up to 350°F (177°C). Many upcoming HPHT deepwater gas/oil wells fall into the tier II, so called ultra HPHT with reservoir pressures up to 20,000 psi (1379 bar) and/or temperatures up to 400°F (203°C) and several deep gas reservoirs, for instance on North American land and on the Gulf of Mexico shelf, fall into tier III, extreme HPHT with reservoir pressures up to 30,000 psi (2068 bar) and/or temperatures up to 500°F (260°C) [24].

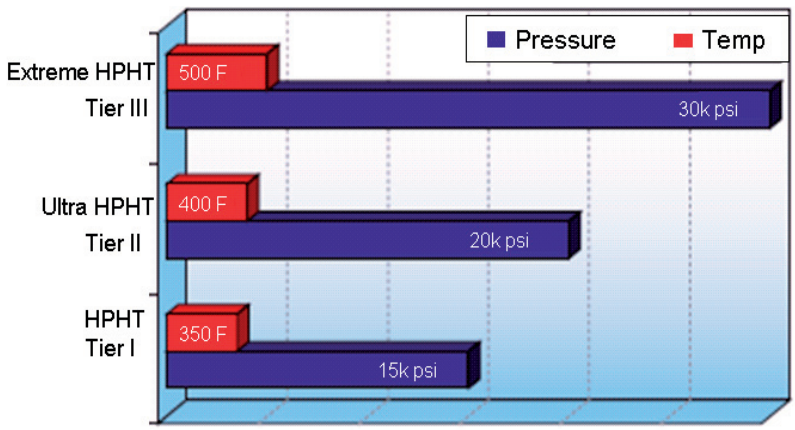

Fig. 1-4 HPHT operations segmented into tiers defined by reservoir temperatures and pressures [24]

1.2 Electrification of downhole applications and Challenges

Electrification of downhole applications has proven to be promising for improving the oil recovery more safely, economically and environmentally friendly, particularly for deepwater offshore wells. However, there are still some challenges associated with the technology due to the harsh HPHT condition, as follows:

Power transmission: How to effectively transmit sufficient power downhole for electrical motors in deep water via a small cross-sectional area is still a challenge. However, by integrating electrical conductors into the tubing, over 200 kW has been successfully transferred over a length of 3.6 km to a downhole electric device. With additional moderate water-cooling conditions, this power can be doubled.

Power electronics: Traditional power electronic design is not sufficient facing HP environment in deep water and possibly high ambient temperatures in downhole bottoms. Today electronics in downhole applications works reliably to about 135°C and function up to around 180°C with an exponential failure rate above 135°C [13]. Currently, downhole motors are usually driven from either onshore or from topside. Newly developed high temperature semiconductor devices can withstand high temperature up to 210°C [122], which makes it possible to drive the motor downhole. One goal of the ongoing research performed by Corac, Dynex and Nottingham University is to develop a complete drive and inverter module that will initially deliver 250 kW of motor drive power in downhole at the ambient temperature of 105°C [18].

Electrical machine: The current standard electrical downhole machine is the induction machine which is relatively inefficient. And the inherent weakness of low starting torque and high starting current limits induction machine to low-torque, high-speed applications. In applications where high torque is required, a mechanical gear is normally added to match the torque, this not only further decrease the system efficiency, also degrades the system reliability. Permanent magnet (PM) machines having higher efficiencies, higher torque densities and smaller volumes, are widely employed in industrial applications to replace conventional machines, but few have been developed for downhole applications due to the high ambient temperatures in deep wells and the low temperature stability of PM materials over time. Today, with the development of advanced technologies and applications of high temperature magnets, it is increasingly interesting for oil and gas industries to develop PM machines for downhole applications.

1.3 Thesis Outline

The objective of the thesis is to investigate different PM machine concepts for downhole applications based upon currently available materials and technologies. A brief outline of the chapters is provided below:

Chapter 2 presents the electrical machine in downhole applications and their advantages.

Chapter 3 reviews the state-of-art about electrical downhole machine and materials. PM machine is likely to become the trend for downhole applications.

Chapter 4 compares conventional radial flux, axial flux and transverse flux PM machines for downhole applications based on analytical approach. Their output torque, torque density, efficiency and power factor are provided as function of the machine axial length and pole numbers.

Chapter 5 studies various topologies of stator PM and rotor PM machines and their characteristics.

Chapter 6 describes two flux-switching (FS) PM machines, called 12/10 and 12/14 pole FSPM machine, with the same stator and winding design, but different rotor pole numbers. Their operation principle has firstly been presented theoretically. Then their output torque, cogging torque, torque ripple, machine inductance and efficiency are studied based on both FEM simulations and prototype measurements.

Chapter 7 newly introduces a simplified lumped parameter magnetic circuit model for analytically designing a high-torque FSPM machine. The design procedure of how to find out the optimal design parameters is also presented. FEM simulations are carried out to verify the results.

Chapter 8 investigates the machine performance at a high temperature based on FEM simulations. The thermal behavior and de-magnetization field are also studied.

Chapter 9 provides the details about the machine prototype. Both FEM simulation and measurement are performed to investigate its characteristics.

Chapter 10 gives the conclusion and some suggestions about future work.

2. Electrification of downhole applications

Currently downhole applications are generally powered by four types of system from topside: mechanical rod connection, pressurized gas, hydraulic power and electrical power systems. This chapter reviews some of the currently available or emerging downhole applications with electrical power system, in which an electrical machine is used instead of the machines driven by other sources. Most of the applications are employed in onshore wells, few in offshore wells. The main reason behind this is the extremely high cost of replacement in failure for offshore applications. The main content in this chapter has been presented in [1].

2.1 Operating Subsurface Valve (SSV)

Fig. 2-1illustrates currently available hydraulic and electro-hydraulic SSVs as well as emerging electric cabled SSVs and future cable free electric SSVs.

The hydraulic SSV systems require two hydraulic power lines for each valve and an instrument cable for the gauges and flow meter. Benefits of this approach are simple valve designs and well proven technology. The main disadvantage is the slow response time for long hydraulic lines. To overcome the drawbacks, an electro-hydraulic system uses electrical signals to operate solenoids that control the delivery of signal pressures to shuttle control valves, which in turn release hydraulic power to activate the tool functions. This system increases the reliability, shortens the response time and reduces the vast number of lines required in purely hydraulic systems. But both hydraulic and electro-hydraulic SSV systems need a hydraulic power unit (HPU), comprising of a low-pressure fluid storage reservoir to store control fluid, a high-pressure pump and a high-pressure storage reservoir (accumulator). The HPU needs a relatively large top space that is a critical issue for offshore applications. Moreover, the hydraulic lines leading from the surface to control values not only frequently cause failure by high fluid leakage rate, but also result in high cost to build up.

In the emerging electric cabled SSVs and cable free electric SSVs (Tubing is used to transmit signals and power) shown in Fig. 2-1 c and d, the valves are directly driven by high torque electrical motors, the response speeds are therefore faster and large volume on the topside occupied by the HPU is released. A valve prototype of a 50W motor driving one-inch variable orifice valve has been presented in [9].

Advantages of electric SSVs:

- No mechanical force, tension or compression required in the tubing to operate valve.
- Valve can be changed to any position at any time regardless of the pressure in the tubing or wellbore or whether the tubing is in tension or compression.
- Fast response and less transmission lines.
- More efficient systems and easier maintenance.

- More environment-friendly.

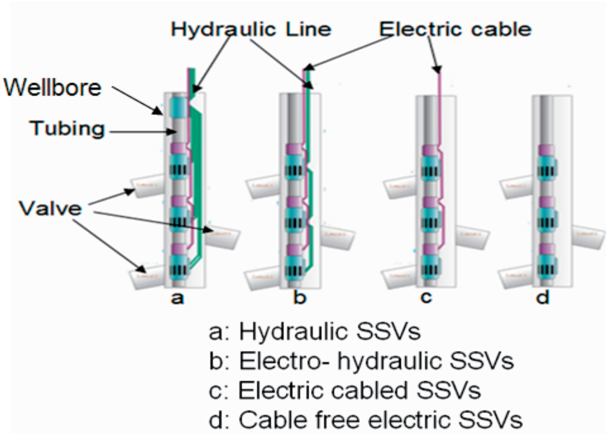

Fig. 2-1 Different SSV technologies [9]

2.2 *Driving Rod Pumps and Progressing Cavity Pumps*

It has long been recognized that production of oil by means of sucker rod pumps or progressing cavity pumps (PCPs) driven by a motor at the surface via a long flexible rod system is very inefficient. Not only are the pumps and the rod connecting the downhole pump very expensive, the rod also usually rubs against the tubing in a number of places and therefore often breaks since most wells are not really "straight". By respectively using downhole linear electrical motors to drive rod pumps or rotation electrical motor to drive PCPs, the abovementioned drawbacks can easily be overcome. The electrically bottom-driven pumps not only eliminate the rod break problem and significantly reduce the tubing wear, but also increase the production by eliminating the couplings, centralizers and rod strings required in surface-driven pumps [11]. Fig. 2-2 shows a simulation comparison between the tubing flow losses for an electrical submersible PCP, where an electrical downhole machine is employed to drive the PCP, and a rod-driven PCP.

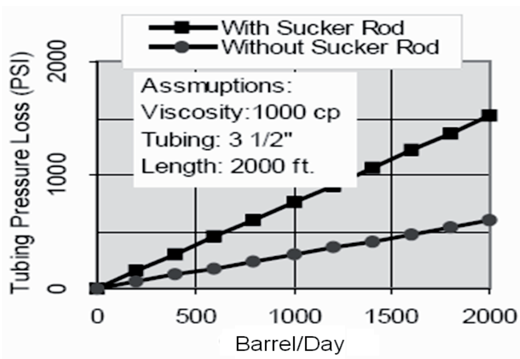

Fig. 2-2 Tubing flow losses [11]

2.3 *Driving Electrical Submersible Pumps (ESPs)*

ESP system, consisting of an electrical motor and a centrifugal pump, can be flexibly located in vertical, deviated even horizontal wells. Due to the robustness, flexibility and reliability, it has been widely installed for artificial lift and downhole oil / water separation (DOWS).

Fig. 2-3 gives the typical application ranges of the five most prevalent artificial lifts: rod pump, progressing-cavity pump, gas lift, hydraulic lift and ESP lift. ESP lift and gas lift have higher capacity and deeper capability than the others and are therefore the standard solution for offshore when artificial lift is required [12]. However, natural gas shortage sometimes limits the use of gas lift, and tubing size and long flow lines also limit the system pressure and hence restrict its efficiency. Moreover, gas lift has reduced benefits as reservoir pressures approach abandonment levels, then ESP lift is normally required to extend field life as shown in Fig. 2-4 [12] [14]. The green area represents production extracted by natural flow, the orange area by gas lift and the blue area by ESP lift. Another important reason to employ ESP lift for offshore wells is that it has less footprint topside while offering the highest yield from most deep-water wells and therefore it has been utilized worldwide [81].

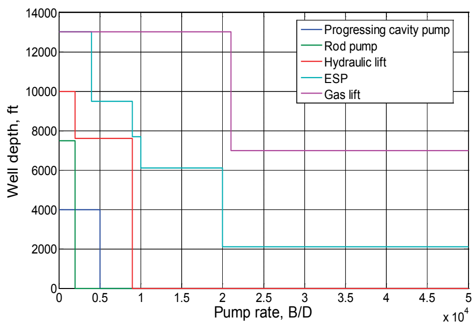

Fig. 2-3 Typical artificial application ranges [14]

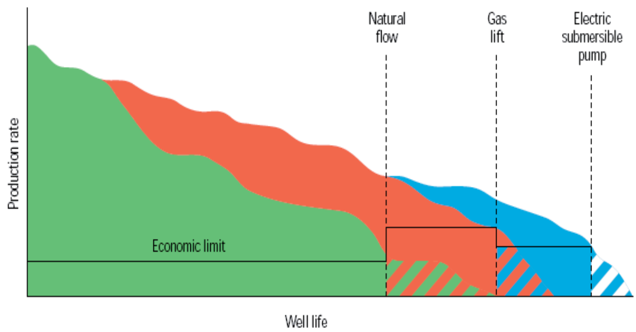

Fig. 2-4 Well life extended by gas & ESP lift [12]

A relatively new technology of ESP DOWS has been developed based on ESP lift systems to reduce the cost of handling produced water as shown in Fig. 2-5, wherein there are two ESPs driven by an electrical motor. One ESP pumps oil-rich stream to the surface while the other one injects water-rich stream to an underground formation so that the cost of treatment and disposal of produced water is significantly reduced. Fig. 2-6 shows a practical production history from an ESP DOWS trial. It was clearly shown that the oil production almost kept constant whilst water production decreased from 300m^3/day to 10m^3/day when an ESP DOWS was installed.

Advantages of ESP [15] [16] [17]:

- Easy to install and low maintenance.
- More compact and deepwater capability.
- High efficiency over 500-1000 barrels/day.
- Good in deviated wells.
- Minor surface equipment needed.
- Increased production and recovery.
- Less environmental impact and cost.

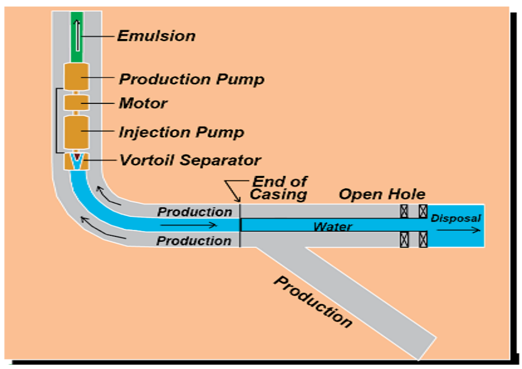

Fig. 2-5 An ESP DOWS system [34]

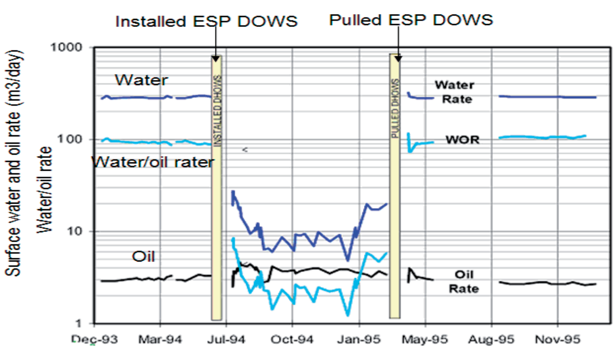

Fig. 2-6 Production history of an ESP DOWS [34]

2.4 *Driving Downhole Gas Compressors*

Downhole gas compression is to boost gas pressure by placing a compressor in close proximity to the source gas reservoir. This can have major economical gains in hydrocarbon recovery in addition to using conventional central gas compression. Fig. 2-7 shows a simulation result of potential yield improvement by downhole gas compression [18]. This application demands the shaft speed in the range of 5,000 to 20,000 rpm that is much faster than the rated speeds of standard induction downhole motors. To match the application speed, standard electrical induction motors have to be coupled with a speed-increasing gearbox. This is also problematic as it is extremely difficult to make a reliable gearbox in the small borehole diameter, and it is also expensive. To eliminate the gearbox, a high-speed PM motor as shown in Fig. 2-8 has been designed and tested for downhole gas compressors.

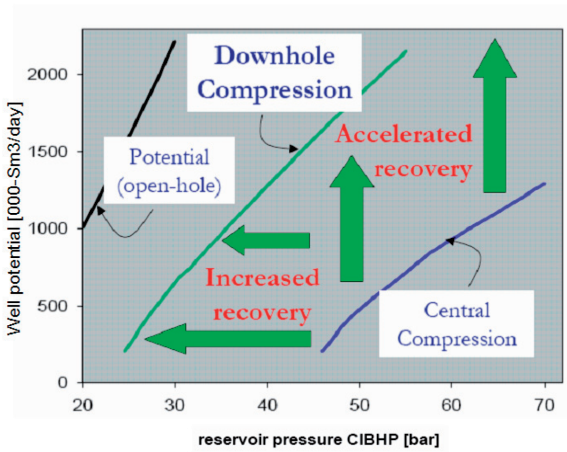

Fig. 2-7 Potential yield improvement by downhole gas compression [18]

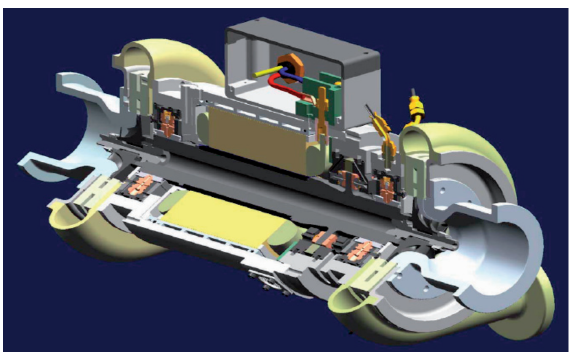

Fig. 2-8 A high speed BLDC downhole motor [18]

Advantage of PM motor driven compressor [18]:

- More compact.
- Increased reliability.
- Increased production.

2.5 As Drilling Motor

In the vast majority of drilling services, downhole power is provided by positive displacement motors (PDMs).The output profile of these motors is well suited to the drilling environment, providing high torque at low rotational speed. However, PDMs have many weaknesses, such as short motor run life, poor performance in high temperature operations, a limited choice of drilling media and the need to compromise the fluids program between drilling and formation requirements. This restricts the operational effectiveness of PDMs in many areas whereas the electric motor offers an efficient and reliable alternative.

Electrical motors allow complete and direct control of the motor functions. Speed may be increased or decreased with a joystick or set through a keyboard instruction as shown in Fig. 2-9. Hydraulic power is required solely for cuttings clearance. This provides better control of the drilling process while allowing circulation flexibility. Another advantage of electrical drilling is that the bottom-hole assembly (BHA) is insensitive to aerated or energized drilling media. In addition, future deep-water developments are likely to make the use of energized drilling fluids more widespread in an effort to reduce the weight of the hydrostatic column. This makes the electrical motor a tool of choice for deep drilling activities. In [19] and [20], two PM drilling motors have been presented.

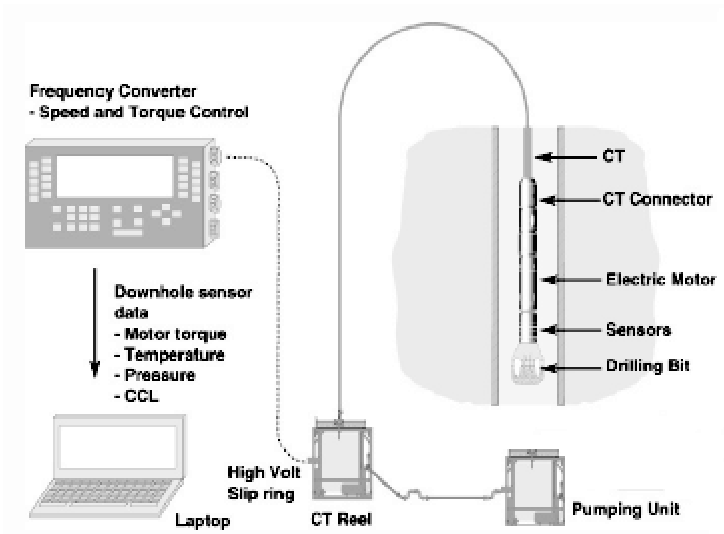

Fig. 2-9 An electrical drilling motor system [21]

Advantages of electrical drilling [19]-[21]:

- Increased reliability of drilling motor extends the mean time between failures of drilling string and reduces drilling costs.
- Electrical motors increase the control and flexibility of the BHA since drilling bit speed is maintained independent of fluid flow rate through direct operator control.
- Suitable for a wider range of drilling environments, particularly for deepwater operations. Electrical motors can operate with a wider range of drilling media than PDMs, such as energized fluids. This makes electrical motors ideal for aggressive under-balanced drilling applications and in deepwater operations.
- Electrical motors could tolerate temperatures up to 200°C with new materials.
- Possible higher rate of penetration.

2.6 As Downhole Generator

Today most downhole tools operate based on battery power, mainly lithium-ion that is limited to 180°C [22]. For very deep wells, the instrumented BHA is critical, but the battery life and higher downhole temperatures constrain their use. The most practical and promising solution to power intelligent downhole tools in HPHT environments is a turbine generator, wherein the turbine converts a small amount of the hydraulic energy in the mud stream to rotary energy, which is then converted to electrical power by an electrical generator.

Advantage of power supply from a HTHP downhole generator:

- More reliable in HTHP environment.
- Suitable for deep wells.

2.7 Conclusion

In this chapter several downhole technologies and applications have been presented and compared. Electrification of downhole applications has presented lots of benefits, such as, increased production, less environment impact, more flexible and less top area required, particularly for deep-water offshore reservoirs that are the exploitation trend for oil and gas industries today.

3. Overview of Electrical Downhole machines

In the previous chapter the electrical machines in downhole applications and their advantages have been presented. This chapter briefly reviews today available electrical downhole machines and gives the comparisons among conventional induction machine, PM machine and switched reluctance machine for downhole applications.

3.1 Basic requirements

The requirements of a downhole machine are significantly dependent on specific applications. In general, an electrical downhole machine should have the following basic characteristics:

1. High reliability and robust for downhole environment

Reliability and robust construction is the most critical requirement for downhole application, particularly in offshore fields. Some offshore operators typically quote US$ 1 million as the cost of changing an electrical submersible pump (ESP). This figure includes the cost of a drilling rig required to install and remove an ESP, personnel cost, offshore transportation, etc, excluding the cost of the ESP itself and the loss of production during the period. Table 3-1 lists the component failure in ESP systems. As can be seen that more than half of the failures occur from the electrical system, in either the motor or cable [26][27].

Table 3-1.Component failures in ESP systems [27].

ESP system component	Percentage of total failures (%)
Assembly (not-specific)	1
Cable	21
Sensor	1
Gas handler	1
Motor	32
Pump	30
Intake	4
Seal/Protector	10
Other	1

2. High torque capability over wide ranges including start-up period

In order to eliminate the gear system required for high torque applications, and hence improving the reliability and efficiency of the whole system, the downhole machine should provide high torque over a wide range.

3. High efficiency

High efficiency is always beneficial for applications, especially in downhole where it is difficult to have an external cooling system for dissipating heat because of the limited cross-sectional area. High efficiency means less loss and hence less heat produced.

4. Easy to control

Due to the harsh HPHT condition, it is challengeable to have measurement device working reliably downhole. Sensor-less control is desirable for downhole applications based on the following advantages [114]:

- Reduction of hardware complexity and cost
- Increased mechanical robustness and overall ruggedness
- Operation in hostile environment
- Higher reliability
- Decreased maintenance requirements
- Increased noise immunity

3.2 *The choice of electrical machine type*

Concerning the demand for high reliability, there are mainly three types of machines considered for downhole applications: induction machine (IM), PM machine and switched reluctance machine (SRM).

3.2.1 Induction machine

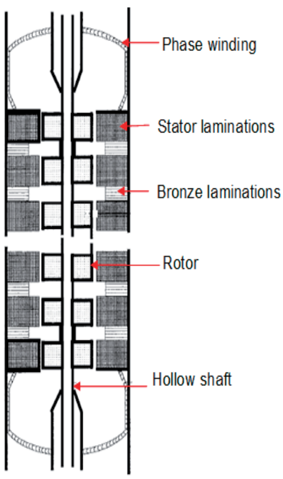

(a)

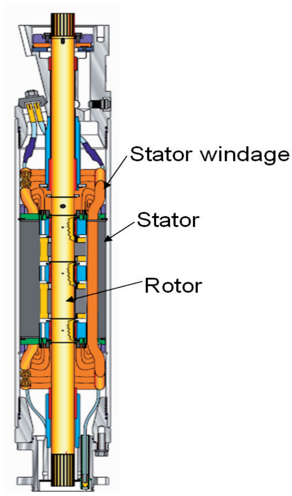

(b)

Fig. 3-1 (a) Structure of a typical multi-rotor induction motor [23] and (b) a standard induction downhole motor [25]

IMs with squirrel-cage rotor are robust, low cost, easy to control and maintenance free. Today they are the standard electrical downhole machine. Fig. 3-1 shows the structure of a typical multi-rotor induction downhole motor [26]. The stator is wound as a single unit and the rotor consists of a number of electrically discrete rotors with bearings between them to accommodate the slender construction. Normally downhole motors are oil-filled, and the oil, having low compressibility, makes it compatible with the high external ambient pressures existing downhole. It also provides bearing lubrication and effective heat transfer for dissipation of the losses radially outward through the motor housing. The outer diameter is typically between 100 to 300 mm and the length is normally from 5 to 10 m, even up to as long as 30 m or longer dependent on applications. The most common power range is from 40 to 200 kW. More power can be achieved with the inclusion of additional motors. The working temperatures are usually limited to 180°C, some specially designed motors can withstand up to 218°C [26][28]. Fig. 3-2 shows the characteristics of a typical induction downhole machine.

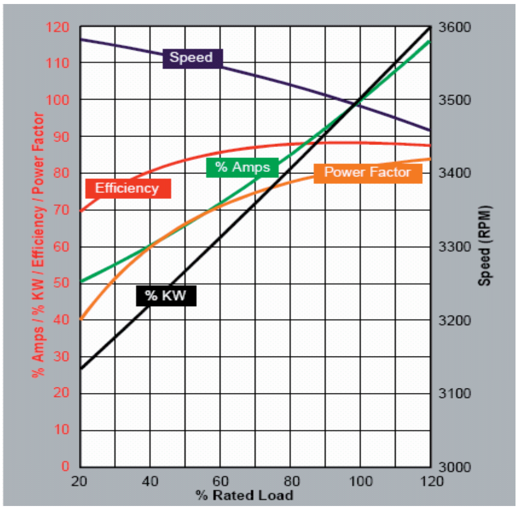

Fig. 3-2 Typical motor characteristics of an induction downhole machine [25]

3.2.2 PM Machine

PM machines, having higher efficiencies, higher torque densities, smaller volumes than conventional IMs, were not employed in downhole applications until recently due to the high ambient temperatures in deep wells and the low temperature stability of PM materials over time.

A permanent magnet DC (PMDC) downhole motor with brushes was presented in [29]. The advantage is that DC current can be transferred to downhole efficiently by reducing the losses over the transmission lines. Further, no variable frequency control is needed, which will save the initial cost. In addition, this machine is very easy to control by simply changing the current value topside. However, there are drawbacks for PMDC machines. The commutator system not only introduces the complex of the machine construction for manufacturing, extra loss over the brushes, more cost for machine prototype, but also frequently causes failure. Furthermore, regular brush replacement is required every 2~ 3 years. In general, this type machine has less reliability compared to a brushless PM synchronous machine (PMSM) and is considered not suitable for offshore downhole applications where the replacement is extremely costly.

With the technology development in variable speed drives (VSDs), PMSM (brushless) becomes the trend for downhole applications.

- A high-torque PMSM capable of withstanding temperatures up to 230°C was designed and tested for electrical drilling [19] [21]. The motor is 2.7 m long and has an outer diameter of 80 mm. Its operating torque is 420 Nm and the peak power is around 20 kW.
- A high-speed PMSM for downhole gas compression was developed [18] as shown in Fig. 2-8.
- A 10-pole interior-mounted PMSM shown in Fig. 3-3 [33] was designed for driving PCPs.
- A PMSM for drilling applications was recently developed as shown in Fig. 3-4 [35].
- One research project focusing on linear PM synchronous machines for downhole drilling is also going on [20].

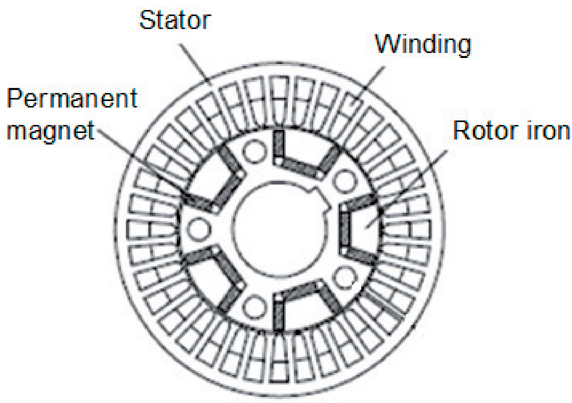

Fig. 3-3 A downhole PMSM [33]

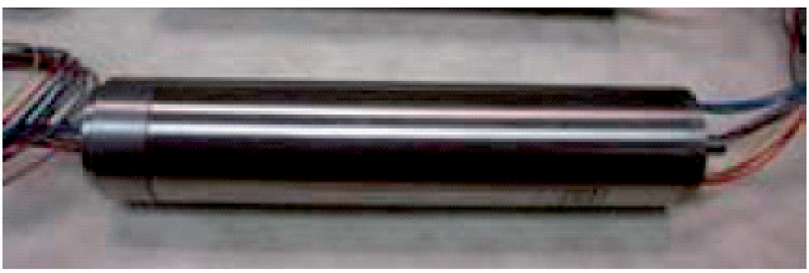

Fig. 3-4 PMSM motor for drilling application [35]

3.2.3 *Switched reluctance machine*

SRMs, shown in Fig. 3-5, having neither magnet nor winding on the rotor, are considered as the most robust machine construction for high temperature applications. They can provide a power density and efficiency comparable to the IMs [104] [106], and they are also cost-effective in production and low-maintenance. Their main drawbacks are high torque ripple, low efficiency and more complicated control system [105] [106] than that of a three-phase drive due to the high non-linearity of the determination of the current-switching angle. Today few have been developed for practical downhole applications.

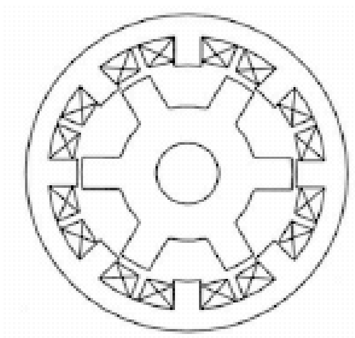

Fig. 3-5 Schematics of a SRM machines [107]

3.2.4 *Comparisons*

Table 3-2 gives a general efficiency comparison between induction and PM downhole motors for different applications. The IMs have an efficiency from 77% to 89% for high-speed applications (driving ESP), and from 60% to 73% for low-speed, high-torque applications (driving PCP). Obviously, the induction motors are inherently unsuitable for low-speed, high-torque applications. One alternative is to install a gearbox to match the normal motor running speed and torque to the pump characteristics. But the re-introduced gear system is not only costly and different to make, it also further decreases the efficiencies of the whole systems. It is evident that the efficiencies of the PM motors, 91-93% for high-speed applications and 85%-89% for high-torque applications [30], are much higher than the IMs. A study shows that the PM motors consume an average of ~ 20% less energy than the IMs [29] [31]. Furthermore, the PM motors have the capability of delivering high torque over whole operation ranges including start-up. Fig. 3-6 shows the performance comparison between two specific induction and PM machines that have the same shaft power, wherein the PMSM is better than the IM in all the aspects.

Table 3-2 Efficiency Comparison of Electrical Downhole Motors

Motor type	Efficiency	Application
IM	77-89%	Driving ESP
IM	60-73%	Driving PCP
PM	91-93%	Driving ESP
PM	85-89%	Driving PCP

Parameter	Down-hole motor		Ratio
	Induction motor EDB36-117B5	Magnet motor 1VEDB36-117B5	
Nominal shaft power, kW	36 (50 Hz)	36 (50 Hz)	
Nominal rotation frequency, RPM	2910	3000	
Nominal required current, A	27,2	23.5	14% lower
Current at zero rate, not more, A	12,5	2,0	84% lower
Efficiency under shaft nominal power, %	83,0	91,5	10% higher
Power factor, COS Φ	0,84	0,96	14% higher
Length of motor, mm	3895 (117 mm OD)	2375 (117 mm OD)	40% shorter
Weight of motor, kg	271	155	43% lighter

Fig. 3-6. Performance comparison: induction motor vs. PM motor [32]

The general performance comparisons among these three type machines are listed in Table 3-3[106] [107].

Table 3-3 Performance comparison among IM, PMSM and SRM machines [106]

	IM	PMSM	SRM
Power density	0	+ +	0
Efficiency	+	+ +	+
Reliability	+ +	0	+
Technical maturity	+	0	0
Controllability	0	+	-

+ + very good, + good, 0 neutral, - bad, - - very bad

The IM features the best reliability at low production cost, but a complicated and expensive field oriented control is required to reach high power and dynamics. It has high efficiency at high speed applications, but its maximum efficiency does not reach the value of a PMSM.

The SRM is comparable in power density and efficiency with the IM, but inferior in the others.

The PMSM offers the best power density, efficiency and controllability. This permits a high power machine with small volume, which is preferable for downhole applications.

3.3 High temperature permanent magnets and insulation materials

The performance of a PM downhole machine is significantly dependent on available permanent magnet and insulation materials to date. In this section PM and insulation materials capable of reliable operating at high temperatures are studied.

3.3.1 PM materials

Today new high performance rare earth-transition metal PMs, including *Sm-Co_5, $Sm_2(Ce, Fe, Cu, Zr)_{17}$* and *Nd-Fe-B*, are enabling technologies for the development of PM machines for high temperature applications [73]-[77].

Nd-Fe-B

Neodymium iron boron, *Nd-Fe-B,* have been widely used in PM machines due to their high energy density (BH), high remanence and good coercivity at relatively high temperatures (less than 200°C). This type magnet has the following characteristics:

- High remanence B_r up to 1.42T
- High energy density BH up to 390 kJ/m^3
- High coercivity H_c up to 2388 kA/m
- Good temperature stability, maximum working temperature up to 200°C.
- Curie temperature up to 350°C.
- Temperature coefficient of B_r, -0.11%/°C.

Sm-Co

Samarium cobalt magnets, *Sm-Co*, have been mostly used in electrical machine for high temperature applications due to their very good temperature stability.

- High remanence B_r up to 1.15T
- High energy density BH up to 248 kJ/m^3
- High coercivity H_c up to 800 kA/m
- Good temperature stability, maximum working temperature up to 300°C.
- Curie temperature up to 825°C.
- Temperature coefficient of B_r, -0.045%/°C.

In recent years, extensive research has been carried out to substantially improve the high–temperature performance of the *Sm-TM* PMs, the maximum operating temperature of the PMs has been increased from around 300°C to as high as 550°C.

3.3.2 Insulation materials

High temperature insulations for motor applications have also been developed. For temperatures above 300°C, an insulation system is used in which inorganic insulating materials, such as synthetic fluoride mica, reconstituted mica and heat resistant glass, are used as the main materials, with very small amounts of silicone resin to improve the processing ability and the mechanical properties. In [78] and [80] thin insulation materials for slot insulation and layer insulation, insulation materials for wedges, impregnants, and lead wire insulation were tested. In functional tests using the stator windings, the windings did not break down until 16000 h at 350°C, 14000 h at 400°C. An inorganic insulation system up to 350°C was presented in which ceramic wire and a heat-resistant, glass cloth-backed silicone mica insulating sheet were used and impregnated with ceramicizable silicone in [79].

3.4 Conclusion

Today's standard electrical downhole motors are energy inefficient. With the development of advanced control technologies and high-temperature PM and insulation materials, a PMSM having higher torque density, higher efficiency and less volume is preferable for downhole applications.

4. Performance Comparisons of Different PM Machines

The current standard electrical downhole machine is the induction machine which is relatively inefficient as discussed in the previous chapter. Today, it is increasingly interesting for oil and gas industries to develop PM machines for downhole applications [36] where the machine outer-diameters are limited by well sizes, but the axial lengths can be relatively long.

This chapter compares the performance of conventional radial flux (RF), multi-stage axial flux (AF) and three-phase transverse flux (TF) PM machines for downhole applications, which has partly been published in [2] and [4]. Three machine prototypes are chosen and optimized individually in terms of maximum torque density based on some common constraints without considering the mechanical construction and machine manufacturing problems. The comparisons are focused on the torque density, machine efficiency and power factor with respect to their pole numbers and machine axial lengths based on analytical calculations.

4.1 Different PM machines and their basic characteristics

According to the traveling direction of their magnetic field in the air gap, PM machines are categorized into RFPM, AFPM and TFPM machines. Each type of the machines has its general characteristics.

4.1.1 Conventional RFPM machine

The most common RFPM machine structure is with one external cylindrical stator and one internal cylindrical rotor. RFPM machines are widely used in industrial applications thanks to their high torque, compactness and high efficiency. This type of machine has various topologies that will further be discussed in the next chapter. Disregarding the different topologies, their general characteristics of RFPM machines are:

- Simple construction.
- High reliability.
- High efficiency.

4.1.2 AFPM machine

AFPM machines are used in several applications where the power density requirements are very high. Usually, there is some amount of forced cooling provided for continuous operation. There are four different machine configurations discussed in [38]and [63], which are single-side slotted, single-side slot-less, double-side slotted and slot-less. Typically, AFPM machines have a disc shape where the ratio of the axial length over its outer diameter is small, less than 1. The investigation in [39] shows when the ratio is less than 0.3 with high pole number (>10 poles), the disc-type AFPM machines can provide both a higher electromagnetic torque and a higher torque density than the RFPM machines.

When the ratio is greater than 1, the conventional RFPM machines are better [39] [41]. In [63] a multi-stage AFPM machine was presented for direct-drive railway traction applications as shown in Fig. 4-1. For a multi-stage machine, the whole machine consists of several double-side AFPM machines, which can have either NN type or NS type as shown in Fig. 4-2.

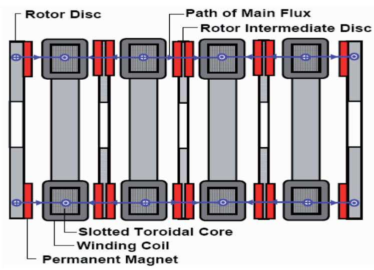

(a)

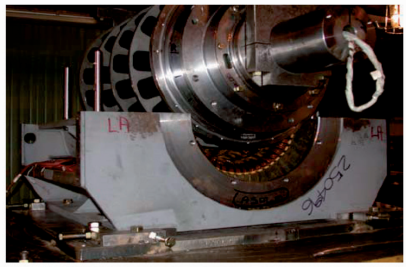

(b)

Fig. 4-1 A four-stage AFPM machine (a) Schematic representation, (b) the prototype [63]

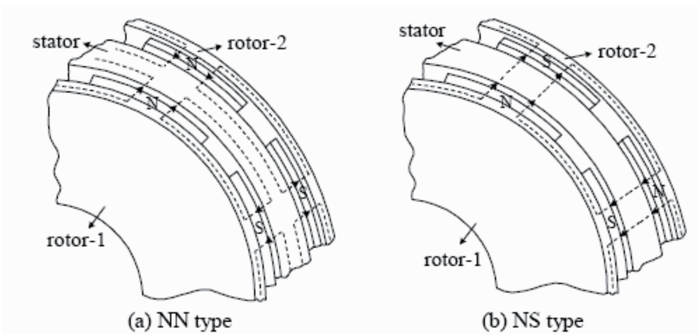

Fig. 4-2 Typical two type AFPM machines (a) NN type, (b) NS type [40]

The common characteristics of AFPM machines are:

- Disc-shape construction for a single-stage machine.
- Normally a forced cooling system is required.
- High power density.

4.1.3 TFPM machine

A TFPM machine utilizes a magnetic circuit that is in a direction perpendicular to the direction of motion and current as shown in Fig. 4-3(a). The increase of electrical loading does not influence magnetic loading since they locate in axial direction and in circumference, respectively. So it is capable of producing power densities much higher than a conventional machine [37]. The high energy density values have taken TFPM machines into high regards in aerospace and other critical applications.

The advantages of TFPM topology against RFPM machines are [64]:

- Increase of pole number does not reduce the magneto-motive force per pole
- Magnetic loading and electrical loading can be varied without compromising the dimensions
- Very simple armature coils
- No end winding
- Possibly very high torque density for high pole machines

The disadvantages of TFPM machines include complex construction with three-dimensional magnetic fields and low power factor. The use of lamination in TFPM machines is complicated, now the application of soft magnetic composite materials makes manufacturing of TFPM machines easier as shown in Fig. 4-3(b), but this increases production costs considerably. Some researches show it is extremely difficult to reach a rated power factor of 0.7 and that other properties have to be sacrificed [45] [65]. The low power factor implies not only substantially increased winding losses, but a required over-rating of the inverter for power supply. Cogging can also be a problem. In TFPM machines, the stator tooth span is approximately equal to a pole span. Hence, cogging reduction by skewing is inefficient and fractional pitch winding is unavailable. The amount of the cogging can be reduced by designing a machine with a lower magnet loading and a higher current loading.

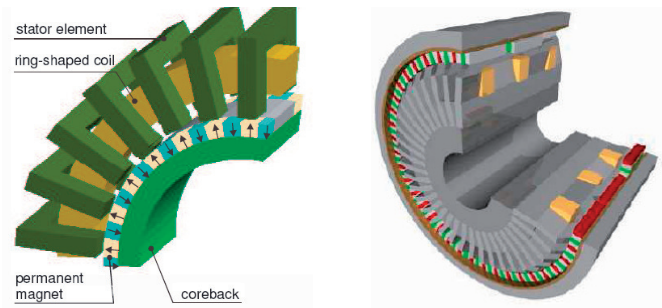

(a) (b)

Fig. 4-3 (a) TFPM machine (b) TFPM with soft magnetic composite [48]

4.2 Three Chosen Machine Prototypes

Each of the RFPM, AFPM and TFPM machines has many construction variations depending on specific applications. In downhole applications, machine construction is chosen based upon following considerations:

- Cylindrical shape: Suitable for cylindrical wells.
- Internal-rotor machines: Normally, with the same dimensions external-rotor RFPM and TFPM machines could provide higher torque density than internal-rotor machines since the former can have greater air gap radius, but it is not the case in downhole applications where the machines need to be enclosed to protect the moving rotors from the harsh conditions within a

small radial space. The internal-rotor machines can use their stator yokes to achieve this function and may have greater outer diameters by eliminating the extra shields required for the external-rotor machines. For AFPM machines an extra shield is always needed. However, this is not taken into account in the investigations presented in this chapter.

- Three-phase machines: Considering the machine self-starting and standard control systems.
- Multi-stage AFPM machines: To provide good performance, a single-stage AFPM machine usually has a disc shape, so it is not practical to design a single-stage AFPM machine with a long axial length. Multi-stage AFPM machines having n+1 stators/rotor and n rotors/stator can have a long axial length by increasing the number of stages.
- Single-sided TFPM machines: Double-sided TFPM machines can usually provide higher torque by fully utilizing the magnetic flux, but they need more radial space and it is challengeable to manufacture them within a small radius. Single-sided TFPM machines are therefore chosen here.

Summarizing the aspects above-mentioned, internal-rotor RFPM, multi-stage AFPM and single-sided TFPM machines with cylindrical shapes as the example shown in Fig. 4-4 are selected to investigate their performances.

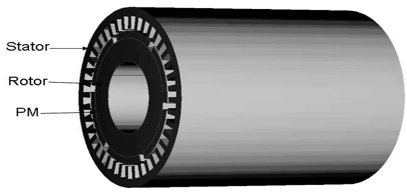

(a)

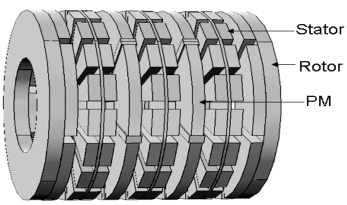

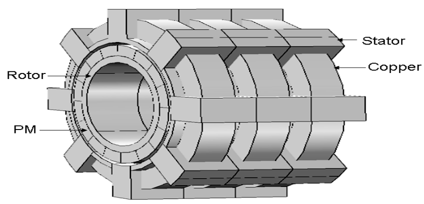

(b) (c)

Fig. 4-4 Example of three machine types (a) RFPM (b) Multi-stage AFPM (here 3 stages) (c) Three-phase TFPM machines

4.3 Machine Constraints

To fairly perform comparisons among the three type machines, some constraints have to be given as follows:

- The pole number is freely chosen, but the pole pitch should not be less than 10 mm to limit the inter-pole flux leakage of the machines [45] [47].
- The maximum flux density in the air gap is limited to 0.9T in order to confine the flux leakage in the TFPM machine.

- The saturation flux density in the iron parts is chosen to be 1.8T except in the tooth iron of the TFPM machine where it is assumed to be 0.9 T to limit the flux leakage. And all the iron parts are assumed to be ideal with infinite permeability.
- An application with a constant speed of 1000 rpm.
- Rectangular open slot with two-layer, full pitch winding and q=1 (slot per pole per phase) for all the RFPM and AFPM machines.
- Only small current densities and electrical loadings are considered. Both the long distances from the topside to downhole and the small radial space limited by wells make it difficult to have a forced cooling system downhole for dissipating heat. For low speed applications like this case (1000 rpm), the dominant loss in the machines is the copper loss which is proportional to the square of machine current. According to [42], a current density of 4 A/mm^2 and an electrical loading of 20 kA/m are appropriate values for an enclosed machine with no external cooling.
- Only slotted machines with surfaced-mounted PM are selected. To produce the same electromagnetic torque with the same dimensions, slotted machines usually have higher magnetic loading and less electrical loading compared with slot-less machines that generally have less magnetic loading, but higher electrical loading. In the case of downhole applications, the selected electrical loading is relatively small; therefore, slotted machines with high magnetic loading are selected.

Assumed constraints for the design are listed in Table 4-1.

Table 4-1Assumed Constraints for the Design

Parameters	Symbol	Values
Well diameter	D_o	100 mm
Machine axial length	L	0.1~1 m
Saturation flux density	B_{sat}	1.8 T
Air gap	g	1.5 mm
Ambient temperature	θ	150 ºC
Speed	ω_m	1000 rpm
Copper resistivity @20 ºC	ρ_{cu}	1.72 10^{-8} Ω/m
Current density	J	4 A/mm2
Electrical loading	S	20 kA/m
PM remanence @20ºC	B_r	1.2 T
PM temperature coefficient	k_{pm}	-0.00045 K^{-1}
Specific loss factor	W	2.7 W/kg
Winding fill factor	k_f	0.6
PM relatively permeability	μ_{pm}	1.05
Temperature coefficient (Cu)	α_{cu}	0.0039 K^{-1}

4.4 Comparison Procedure

4.4.1 Electromagnetic Torque Calculation

The electromagnetic torques developed at the machine air gaps of the RFPM and AFPM machines can be expressed as (4.1)[43][[49].

$$T = \begin{cases} \dfrac{1}{2} k_t k_\sigma \pi S B_{g1} D_o^2 \lambda^2 L & \text{RF} \\ k_t k_\sigma \pi S B_{g1} R_{so}^3 \lambda (1-\lambda^2) & \text{AF} \end{cases} \quad (4.1)$$

where B_{g1} is the *rms* value of the fundamental air-gap flux density, λ is the ratio of D_i/D_o, here D_i and D_o are respectively the machine inner- and outer-stator diameters, and for the RFPM and TFPM machines D_o equals to the well diameter. L is the active axial length of the machine. k_t is the machine constant that depends on both the actual air-gap flux density distribution and the winding arrangement. For square-wave flux density distributions and full pitch windings, its value is unity. Here it is assumed to be the case. k_σ is the fringing factor representing the amount of flux from the air gap to the stator teeth and it is determined by (4.12). S is the electrical loading with unit in A/m. R_{so} is the outer-stator radius of the AFPM machines and it is dependent on pole number p and evaluated by (4.40) [39] (see Fig. 4-11).

The torque expression of the TFPM machines is derived as follows:

The electromagnetic torque produced by an electrical machine can be calculated by

$$T = m E_{ph} I_{ph} / \omega_m \,. \quad (4.2)$$

where m is the phase number, E_{ph} is the induced phase voltage, and for the TFPM machines it can be expressed as (4.3)[49]. I_{ph} is the phase current and determined by (4.4), ω_m is the mechanical angular speed and calculated by (4.5).

$$E_{ph} = 2 k_\sigma \pi f_e n_s k_\sigma D_o \lambda B_{g1} l_m \quad (4.3)$$

where l_m is the magnet depth (see Fig. 4-16), n_s is the number of turn in one phase, f_e is the electrical frequency.

$$I_{ph} = \pi D_o \lambda S / n_s \quad (4.4)$$

$$\omega_m = 4\pi f_e / p \quad (4.5)$$

Substituting (4.3)-(4.5) into (4.2), the torque expression for the TFPM machines is obtained as

$$T = \frac{1}{2} k_\sigma m p \pi S B_{g1} D_o^2 \lambda^2 l_m \,. \quad (4.6)$$

4.4.2 Fringing Factor Evaluation

Fig. 4-5 depicts the magnetic flux paths in the air gap of one pole in a surfaced mounted PM machine, where part of the flux from the magnet does not go through the air gap for torque production. To take this into account, a fringing factor k_σ defined by (4.7) is employed for torque calculations.

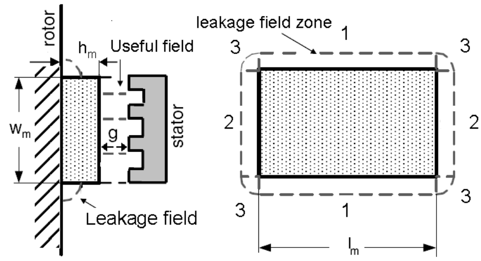

(a) (b)

Fig. 4-5 Magnetic flux distribution

(a) cross-section in flat form (b) leakage field between the PM and rotor yoke

$$k_\sigma = \frac{P_g}{P_g + P_{lk}} \tag{4.7}$$

where P_g and P_{lk} are individually the main air-gap permeance and leakage permeance, and they are respectively evaluated by (4.8) and (4.9).

$$P_g = \mu_0 \frac{A_m}{k_c g} \tag{4.8}$$

$$P_{lk} = 2P_1 + 2P_2 + 4P_3 \tag{4.9}$$

where k_c is Carter's coefficient that takes care of the stator slot effect in the air gap and can be calculated from (4.10) after machine magnetic designs. For the TFPM machines, k_c is assumed to be 1.1. g is the air gap length. A_m is the magnet surface area in magnetizing direction. P_1, P_2 and P_3 are respectively the permeance in the leakage zone 1, 2 and 3 in Fig. 4-5(b). The description of the leakages field and the formulae to evaluate their permeances have been presented in [49] and are employed here, and then the fringing factors for the RFPM and AFPM machines can be approximated by (4.12), in which it is clearly shown that the value decreases, which means the flux leakage increases, with an increase of the pole number.

The carter's coefficient is calculated as [49]

$$k_c = \tau_{slot} / \left(\tau_{slot} - \gamma g\right) \tag{4.10}$$

where

$$\gamma = \frac{4}{\pi}\left[\frac{W_s}{2g}\arctan\left(\frac{W_s}{2g}\right) - \ln\sqrt{1+\left(\frac{W_s}{2g}\right)^2}\right] \tag{4.11}$$

where τ_{slot} and W_s are respectively the slot pitch and slot width.

$$k_\sigma = \begin{cases} \dfrac{D_o \lambda L \pi}{D_o \lambda \pi (L + 0.52 k_c g) + k_c g p (1.04 L + 0.308 h_m)} & \text{RF} \\ \dfrac{R_{so}^2 (1-\lambda^2)}{R_{so}^2 (1-\lambda^2) + 0.52 k_c g R_{so} (1+\lambda) + k_c g p (1.04 l_m + 0.308 h_m) / \pi} & \text{AF} \end{cases} \tag{4.12}$$

where h_m is the magnet thickness.

For TFPM machines, typically the fringing factor is around 0.5 due to the high flux leakage in three dimensions [45][50]. The value of k_σ determined by (4.12) will be much greater than this value. So for the discussed TFPM machines the value of k_σ calculated by (4.12) is modified to a value close 0.5 by multiplying a correcting coefficient of 0.6. To obtain a more accurate value for a specific case, FEM simulations are required.

4.4.3 Power Factor Calculation

Compared to the reactance of the armature winding, the winding resistance is generally negligible, and then the power factor can be approximated by

$$PF = \frac{E_{ph}}{\sqrt{E_{ph}^2 + (\omega_e L_s I_{ph})^2}} . \tag{4.13}$$

where ω_e is the electrical angular speed. E_{ph} can be expressed in terms of ω_e by (4.14) and I_{ph} is evaluated from (4.4) or (4.15). L_s is the synchronous inductance determined by (4.16).

$$E_{ph} = \begin{cases} 2 k_t k_\sigma n_s \omega_e D_o \lambda B_{g1} L / p & \text{RF} \\ 2 k_t k_\sigma n_s \omega_e B_{g1} R_{so}^2 (1-\lambda^2) / p & \text{AF} \\ k_\sigma n_s \omega_e D_o \lambda B_{g1} l_m & \text{TF} \end{cases} \tag{4.14}$$

$$I_{ph} = \begin{cases} \dfrac{\pi \lambda D_o S}{2 m n_s} & \text{RF} \\ \dfrac{\pi \lambda R_{so} S}{m n_s} & \text{AF} \end{cases} \tag{4.15}$$

$$L_s = L_m + L_{lk} \tag{4.16}$$

where L_m is the magnetization inductance evaluated by (4.17)[49]-[51]. L_{lk} is the leakage inductance and approximated from (4.18) by only considering the slot leakage inductance and end winding inductance [49]-[52].

$$L_m = \begin{cases} \dfrac{4m\mu_0 (k_t n_s)^2 D_o \lambda L}{k_c \pi p^2 (h_m + g)} & \text{RF} \\ \dfrac{4m\mu_0 (k_t n_s)^2 R_{so}^2 (1-\lambda^2)}{k_c \pi p^2 (h_m + g)} & \text{AF} \\ \dfrac{\mu_0 n_s^2 \pi \lambda D_o l_m}{4k_c (h_m + g)} & \text{TF} \end{cases} \tag{4.17}$$

$$L_{lk} = \begin{cases} \dfrac{4\mu_0 n_s^2 l_m}{pq} \left(\dfrac{h_s}{3W_s} + \dfrac{0.3 q l_{end}}{l_m} \right) & \text{RF and AF} \\ \mu_0 n_s^2 h_s \pi \lambda D_o (1+k_i) / 6W_s & \text{TF} \end{cases} \tag{4.18}$$

where k_i accounts for the leakage inductance between the stator cores of the TFPM machines. In general, k_i <0.2 ~ 0.3[50]. Here 0.2 is selected. H_s is the slot height. L_{end} is the end winding length and evaluated from (4.33), (4.38) or (4.39).

Now the power factor for each type machine can be calculated by substituting(4.4), (4.14)-(4.18) into (4.13). It should be noted that the power factor is independent of n_s and ω_e when neglecting the winding resistance.

4.4.4 Efficiency approximation

The copper loss is calculated by

$$P_{cu} = k_f J^2 A_{cu} \rho_\theta l_{cu} \,. \tag{4.19}$$

where A_{cu} is the copper area, J is the current density, k_f is the winding fill factor, l_{cu} is the copper length including the end windings, ρ_θ is the copper resistivity at temperature T_θ and is calculated by

$$\rho_\theta = \rho_{20} (1 + \alpha_{cu} (T_\theta - 20^\circ)) \,. \tag{4.20}$$

where α_{cu} is the temperature coefficient.

The iron loss in each iron part is approximated by [44]

$$P_{Fe} = 0.078 W f (100 + f) B_{Fe}^2 G_{Fe} 10^{-3} \,. \tag{4.21}$$

where W is the specific loss factor in W/kg, G_{Fe} is the weight of the iron part, while B_{Fe} is the peak flux density in the corresponding iron part. For the RFPM and the AFPM machines, it is assumed that there is no iron loss in the rotor iron parts. And for the TFPM, a flux density of 0.9 T is used to evaluate the loss.

The efficiency is then evaluated by

$$\eta = T\omega_m / (T\omega_m + P_{cu} + P_{Fe}) \,. \tag{4.22}$$

4.4.5 Torque Density and Apparent Power Evaluation

The torque density here is defined as the ratio of electromagnetic torque to overall machine volume including end-windings

$$\xi_T = \frac{4T}{\pi D_o^2 L_{tot}} \tag{4.23}$$

where L_{tot} is the total machine axial length.

The required apparent power is evaluated by

$$S_{in} = T\omega_m / (\eta PF) \,. \tag{4.24}$$

4.5 Optimal Design Variables

As clearly seen from (4.1) and (4.6) the key variables for each machine design are B_g (B_{g1}) and λ. In order to obtain the optimal machines having the highest torque density, their optimal values addressing to the maximum torque densities with respect to different pole numbers and machine axial lengths are investigated by assuming k_σ =1 for the RFPM and AFPM machines and k_σ =0.5 for the TFPM machines. The values are recalculated later after the machine designs by (4.12) for machine performance evaluations.

4.5.1 RFPM Machines

4.5.1.1 Magnetic design

To avoid magnetic saturation, the thickness of the stator back iron and rotor back iron should be the same and are obtained as:

$$H_{sb} = \frac{\alpha_{pm} B_g \pi \lambda D_o}{2pB_{sat}} \tag{4.25}$$

The teeth height:

$$H_t = \frac{(1-\lambda)D_o}{2} - H_{sb} \tag{4.26}$$

Assuming that all the flux produced by the magnets goes through the stator teeth, the total stator tooth width without saturation is calculated by

$$W_{st-total} = \frac{\lambda D_o \pi B_g \alpha_{pm}}{B_{sat}} \tag{4.27}$$

In order to get maximum copper area, taper teeth is assumed, thus the copper area is calculated as:

$$A_{cu} = \pi\left((D_o/2 - H_{sb})^2 - (D_o/2 - H_{sb} - H_t)^2\right) - H_t W_{st-total} \tag{4.28}$$

The slot pitch is determined by

$$\tau_{slot} = \frac{D_o \pi \lambda}{mpq} \tag{4.29}$$

The slot opening is

$$W_s = \tau_{slot} - \frac{W_{st-total}}{mpq} \tag{4.30}$$

And the magnet thickness is

$$h_m = \frac{\mu_{pm} k_c g B_g}{\mu_0 \left(B_a - B_g\right)} \tag{4.31}$$

where k_c is determined by (4.10), B_a is the magnet remanence at the ambient temperature T_θ and it is determined by (4.32) to take the PM temperature coefficient into account.

$$B_a = B_r \left(1 + k_{pm}(T_\theta - T_0)\right) \tag{4.32}$$

4.5.1.2 End winding approximation

The method presented in [39] for calculating the end-winding length of RFPM and AFPM machines is employed here. The equivalent length of half the end connect of a winding coil in the RFPM machine is approximated as

$$l_{end\_RF} = \pi^2 (\lambda D_o + H_t) / 2p \, . \tag{4.33}$$

where H_t is the tooth height determined by magnetic design of the stator core.

For a specific RFPM machine the total machine axial length is evaluated by

$$L_{tot} = L + l_{ea} \, . \tag{4.34}$$

where l_{ea} is the axial length of the end-winding encumbrance and is assumed as [39]

$$l_{ea} = 2 l_{end\_RF} / \pi \, . \tag{4.35}$$

4.5.1.3 Optimal Parameters

The torque density can now be calculated by insetting (4.1) and (4.33) - (4.35) into (4.23) for a given pole number and machine length. It should be noted that, to calculate the torque from (4.1), S=20 kA/m is used for the machines with small λ values, which have enough space for copper in their stators. For the machines with big λ values, the machine current is limited by the available copper area, and the electrical loading is then determined by

$$S = A_{cu} J k_f / \pi D_o \lambda \, . \tag{4.36}$$

Fig. 4-6 shows an example of the result for 6-pole machines with an axial length of 0.5 m, varying B_g from 0.4 to 1.0 T and λ from 0.3 to 0.8. It is clearly seen that the torque density at a specific B_g first increases along with an increase of λ until reaching its maximum value, then decreases with a further increased λ leading to a reduced copper area which determines the electrical loading by (4.36). For each B_g there is an optimum λ to obtain maximum torque densities that increases along with an increase of B_g. As a constraint given in the subsection of Machine Constraints, B_g =0.9T is chosen for the RFPM machines.

It is also observed from Fig. 4-6 that the optimal λ value increases along with a decrease of the air-gap flux density due to a thinner stator yoke needed to avoid the iron saturation. It is well-known that the required yoke thickness is inversely proportional to pole number p for RFPM machines. To obtain the optimal λ with respect to the pole number, one computer program is made in MATLAB to investigate the torque densities of the machines with B_g =0.9T, p varied from 4 to 28 and λ varied from 0.3 to 0.8. Fig. 4-7 provides the analytical results, and the curve can be approximated by the following simplified expression

$$\lambda = 0.8 - 0.8 / p \,. \tag{4.37}$$

For the RFPM machines it is obvious that the optimal values of λ and B_g are independent of the machine axial length.

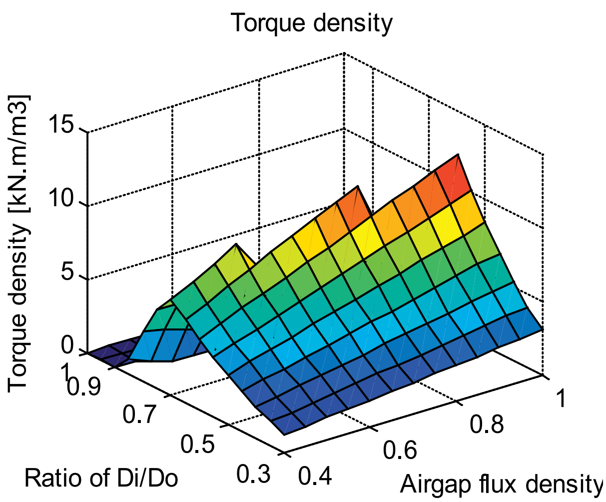

Fig. 4-6 Torque density with respect to different λ and B_g

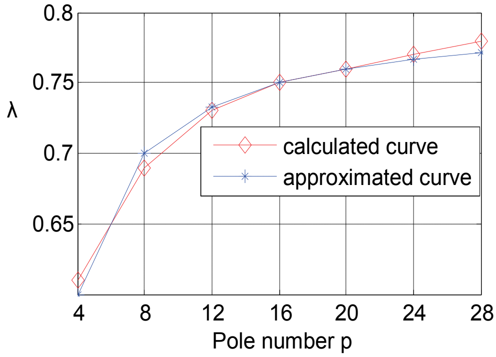

Fig. 4-7 Optimal λ for different pole numbers

So far the air-gap density B_g =0.9 T is chosen for all the RFPM machines and the optimal values of λ are evaluated from (4.37) for different pole machines, disregarding the axial length of the machines. After the machine magnetic design the fringing factor and power factor can respectively be evaluated by (4.12) and (4.13). And then the output torque, machine efficiency and torque density with respect to the pole number and axial length can be investigated by (4.1), (4.22) and (4.23). The results are shown in Fig. 4-8. The maximum output torque is up to 75 Nm as shown in Fig. 4-8(b) and the maximum apparent power required is 8.8 kVA determined by (4.24).

4.5.1.4 Conclusions and explanations for the analytical results

1. More torque density can be achieved by an increase of the pole number due to the reduction of the end-winding length in axial direction evaluated from (4.33) and (4.35), and the increase of the inner-stator radius determined by (4.37).
2. The machines have high efficiencies, more than 90%, which first increases along with an increase of the pole number to the maximum value of around 95% for 8-pole machines and then decreases. By increasing the pole number, the machine torque increases and the stator copper loss decreases due to reduced end winding length, which implies increased machine efficiency. On the other hand, both eddy current loss and hysteresis loss increase since the operating frequency increases proportionally to the number of poles in order to achieve the desired speed. This will decrease the machine efficiency. There is a trade off between them.
3. For the machines longer than 0.2 m, the torque density is almost independent of the machine axial length because the end-winding length in axial direction is negligible compared to the active winding length of the machines.
4. Thanks to the large equivalent air gap, small outer diameter and low electrical loading, the machines have a high power factor. This value slightly decreases along with an increase of the pole number due to the increase of the flux leakage in the air gap determined by (4.12).

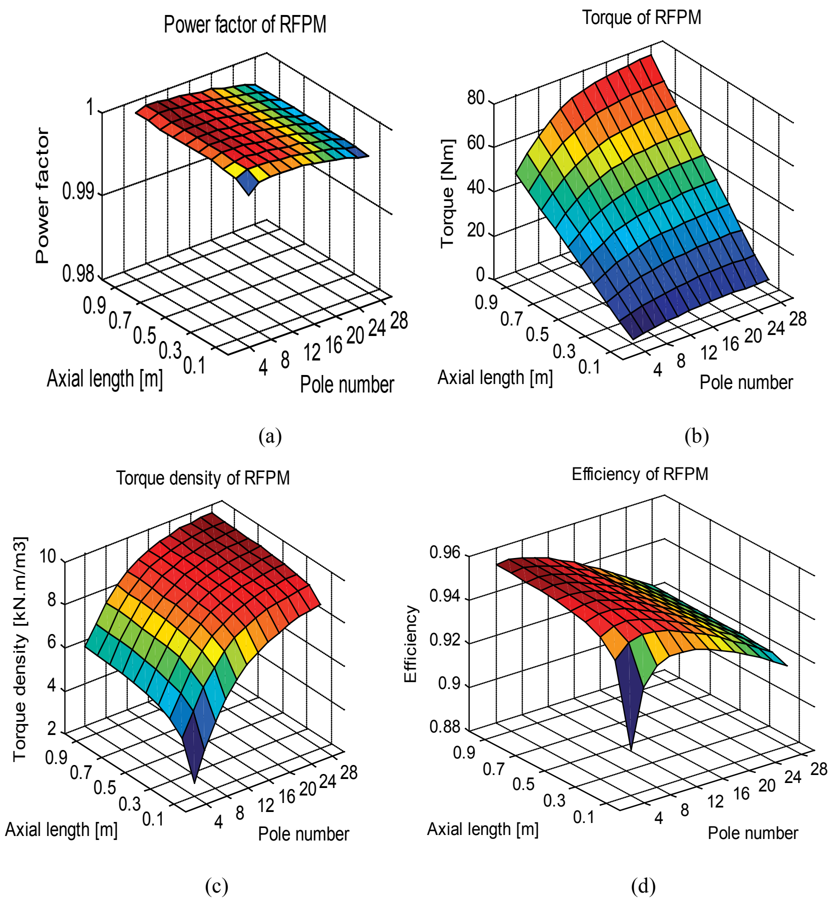

Fig. 4-8 Performance parameters of the RFPM machines (D_o = 100 mm) as functions of axial length and pole number (a) Power factor (b) Output torque (c) Torque density (d) Machine efficiency

4.5.2 AFPM Machines

Multi-stage AFPM machines may have either the same or different magnet polarity at both sides of each stator, so are respectively called NN-type or NS-type machines [46], as the example shown in Fig. 4-9. In the NN-type machine, the yoke iron in each stator and rotor is needed for guiding magnetic flux, whilst it is only required at the two ends in the NS-type machine. In the NN-type machine, the stator current flows in reverse direction in each of the back-to-back stator slots. A back-to-back wrapped winding structure as in Fig. 4-10 (a) is used in this topology. The back-to-back wrapped winding is one in which the windings are wrapped around the stator periphery in much the same manner as the winding of a toroid. Whereas, in the NS-type machine, the stator current flows in the same direction in each of the back-to-back stator slots in order to create torque, so a lap winding as in Fig. 4-10 (b) is employed. Fig. 4-11 depicts their winding sketches.

4.5.2.1 End winding evaluation

The equivalent length of half the end connects of a winding coil in the NN-type and NS-type AFPM machines are respectively evaluated by (4.38) and (4.39) [39].

$$l_{end\_NN} = \alpha_{pm}\pi^2 B_g R_{so}\left(1+\lambda\right)/(pB_{sat}) \tag{4.38}$$

$$l_{end\_NS} = \frac{\pi D_o \sin\left(\pi/p\right)}{4} + \left(\frac{\pi}{2} - \frac{\pi}{p}\right)\frac{\lambda D_o \tan\left(\pi/p\right)}{2} \tag{4.39}$$

$$R_{so} = \begin{cases} \dfrac{D_o/2}{\sin\left(\pi/p\right) + \cos\left(\pi/p\right)}; & \text{NS type} \\ \dfrac{pB_{sat}D_o}{2pB_{sat} + B_g\alpha_{pm}\pi(1+\lambda)}; & \text{NN type} \end{cases} \tag{4.40}$$

where α_{pm} is the magnet coverage, here it is assumed to be unity, B_{sat} is the iron saturation flux density, B_g is the flux density in the air gap over the magnets, and its distribution is assumed to be a square waveform. The relationship between B_{g1} and B_g is

$$B_{g1} = \frac{2\sqrt{2}}{\pi} B_g \sin(\alpha_{pm}\frac{\pi}{2}). \tag{4.41}$$

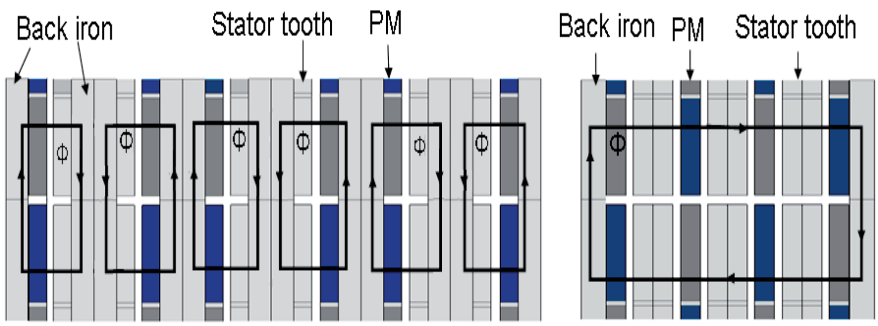

(a) (b)

Fig. 4-9 Side view of (a) NN-type AFPM and (b) NS-type AFPM machines

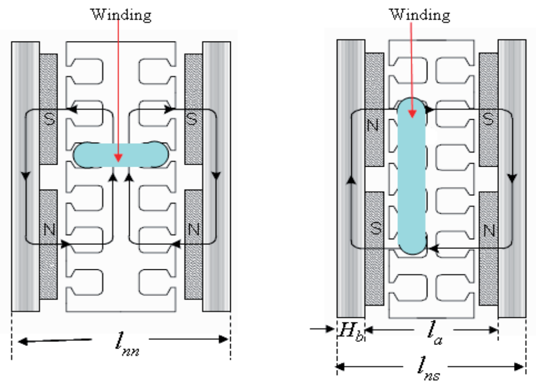

(a) (b)

Fig. 4-10 Single-stage (a) NN-type and (b) NS-type AFPM machines

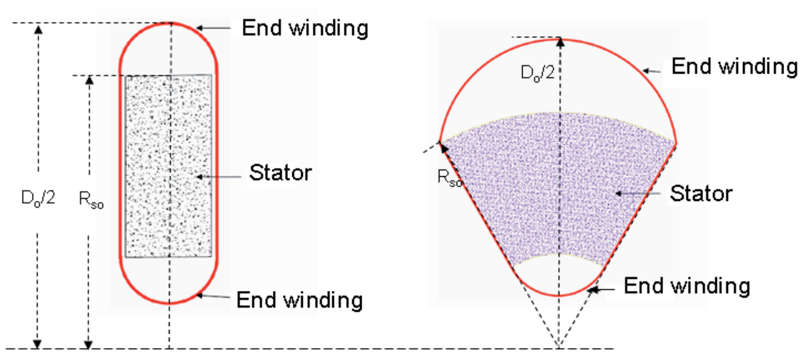

(a) (b)

Fig. 4-11 Sketch of coil geometry of (a) NN-type and

(b) NS-type AFPM machines

Before investigating the performance of the multi-stage AFPM machines, two single-stage machines shown in Fig. 4-10 are studied. The physical structures of the stator and rotor of these two machines are exactly the same except for the thickness of the stator yoke and winding arrangement. Unlike the NN type, the NS type does not require any stator back iron since the main flux travels axially. This feature implies an increase in torque density and efficiency, and a reduction in the stator thickness and iron loss. However, using lap winding in the NS structure results in longer winding length and end winding, which implies smaller outer stator diameter (see Fig. 4-11), higher copper loss, less efficiency and torque density.

4.5.2.2 Magnetic design of single-stage machine

The internal stator H_{sb} of the NN- type machine is determined by

$$H_{sb} = \frac{\alpha_{pm} \pi B_g}{p B_{sat}} R_{so} \left(1 + \lambda\right) \tag{4.42}$$

The rotor iron thickness at the two end of the machine is half of H_{sb}.

The tooth width increases along the radial direction from inside to outside, but the radian of one tooth is constant and it is determined by

$$\alpha_{tooth} = \frac{2\pi \alpha_{pm} B_g}{mpq B_{sat}} \tag{4.43}$$

The stator tooth height is

$$H_t = \frac{2\pi S}{\left(2\pi - mpq\alpha_{tooth}\right) J k_f} \tag{4.44}$$

The tooth height here is the summary of the two tooth depths shown in Fig. 4-9.

Substituting (4.43) into (4.44)

$$H_t = \frac{S B_{sat}}{\left(B_{sat} - \alpha_{pm} B_g\right) J k_f} \tag{4.45}$$

The slot pitch is determined by

$$\tau_{slot} = \frac{2 R_{so} \pi \lambda}{mpq} \tag{4.46}$$

The slot opening is

$$W_s = \tau_{slot} - \lambda R_{so} \alpha_{tooth} \tag{4.47}$$

The PM thickness here including the both sides in a single-stage machine can be calculated as

$$h_m = \frac{2\mu_{pm} k_c B_g g}{\mu_0 (B_a - B_g)} \tag{4.48}$$

where k_c is determined by (4.10)

The axial length is

$$L = \begin{cases} 2H_{sb} + H_t + h_m + 2g & \text{NN type} \\ H_{sb} + H_t + h_m + 2g & \text{NS type} \end{cases} \tag{4.49}$$

The total copper cross-sectional area in the stator is:

$$A_{cu} = 2 H_t \lambda R_{so} \pi \left(1 - \frac{\alpha_{pm} B_g}{B_{sat}}\right) \tag{4.50}$$

The copper loss is calculated by:

$$P_{cu} = A_{cu} k_f J^2 \rho_\theta \left(R_{so} \left(1 - \lambda \right) + l_{end} \right) \tag{4.51}$$

To compare the performance of these two machines, their torque densities are calculated by employing (4.1), (4.40) and (4.23). Fig. 4-12 shows the torque densities with respect to λ and B_g of these two single-stage machines with 24 poles and S=20 kA/m. For the AFPM machines, their axial length can be adapted to ensure a large enough copper area so that the electrical loading is fixed to 20 kA/m. Their maximum torque densities shown in Fig. 4-12 for these two single-stage machine are very close (5.9 kNm/m^3 for the NS-type machine and 5.8k Nm/m^3 for the NN-type machine). The conclusion is also valid for low pole machines from performed analytical calculations.

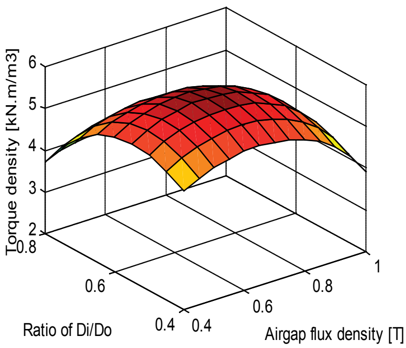

(a)

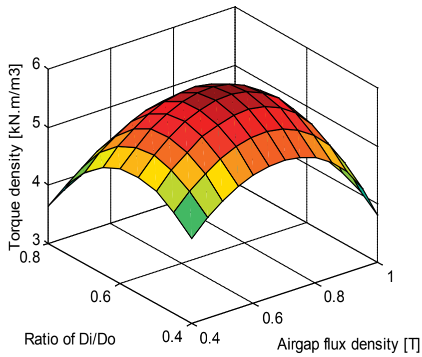

(b)

Fig. 4-12 Torque density of single –stage TFPM machines with respect to λ and air-gap flux density (a) 24-pole NN type (b) 24-pole NS type

For a multi-stage NN-type machine as that in Fig. 4-9, consisting of multiple single-stage NN-type machines, both its electromagnetic torque and axial length are proportional to its stage number, so its torque density is therefore independent of the stage number and is the same as that of a single-stage machine; whereas the torque density of a multi-stage NS-type machine is greater than that of a single-stage one due to the absence of all the yoke iron except at the two ends of the machine. So NS-type multi-stage machines may have greater torque densities and are hence chosen for further investigations.

4.5.2.3 Optimal Parameters

To find the optimal B_g for obtaining maximum torque density, S is fixed to 20 kA/m, B_g is varied between 0.4 and 1T, and for each B_g value, λ is varied from 0.4 to 0.8. Fig. 4-13 (a) shows the maximum torque densities with respect to B_g for 4, 8 and 12-pole machines. An optimal value of B_g =0.7T is found and it is independent of the pole number.

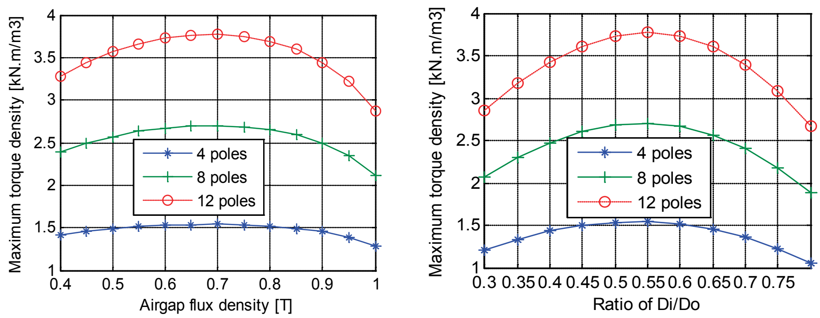

(a) (b)

Fig. 4-13 The maximum torque density of the NS machines with respect to (a) air-gap flux density and pole number (b) ratio λ and pole number

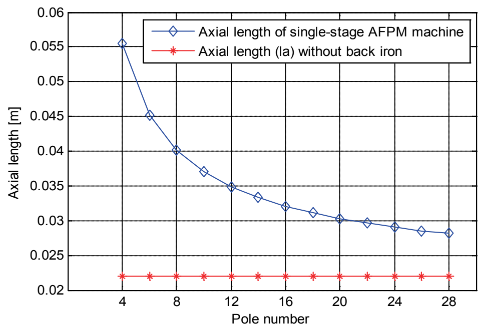

Fig. 4-14 Axial length of single-stage NS type AFPM machines with different pole numbers

To obtain the optimal λ, S is fixed to 20 kA/m, λ is varied between 0.4 and 0.8, and for each λ value, B_g is varied from 0.4 to 1T. Fig. 4-13 (b) shows the maximum torque densities with respect to λ value for 4, 8 and 12-pole machines. The optimal value λ=0.55 is obtained and it is also independent of the pole number.

Fig. 4-14 shows the axial lengths l_{ns} of single-stage NS-type machines with respect to pole numbers, the lengths decrease along with an increase of the pole number due to a thinner back iron required for high pole machines.

For a n stage NS-type machine, the torque density is determined by

$$\xi_T = \frac{4nT_1}{\pi D_o^2\left(nl_a + 2H_b\right)}. \tag{4.52}$$

where T_1 is the torque produced by the corresponding single-stage NS-type machine and determined by (4.1), l_a is the machine axial length without the back iron, H_b is the back iron width (see Fig. 4-10).

For the machine with an axial length L_{tot}, its stage number n is determined by

$$n = (L_{tot} - 2H_b) / l_a . \tag{4.53}$$

if n is not an integer here, the machine torque density is approximated by that of the machine with the nearest integer stage number smaller than n. Since l_a is relatively small as shown in Fig. 4-14, the approximation will not affect the result significantly. It is clear that the machine axial length does not influence the optimal values, but determines how many stage the machine has.

Now the optimal values of B_g = 0.7 T and λ = 0.55 have been found and they are independent of both the pole number and the machine length. Fig. 4-15 presents the power factor, output torque, torque density and machine efficiency with respect to the pole number and the axial length for the multi-stage NS-type AFPM machines. The maximum output torque is up to 50 Nm as shown in Fig. 4-15 (b) and the maximum apparent power is 6.3 kVA evaluated from (4.24).

4.5.2.4 Conclusions and explanations for the results:

1. More torque density can be achieved by an increase of pole number due to the reduction of the thickness of the back iron and the increase of the outer stator radius from (4.40).
2. The machines always have efficiency less than 90%, which first increases along with an increase of the pole number to the maximum value of around 88% for 16-pole machines and then decreases. Just like the RFPM machines, by increasing the pole number the machine torque increases and the stator copper loss decreases due to reduced end winding length, which implies increased machine efficiency. Meanwhile, both eddy current loss and hysteresis loss increase since the operating frequency increases proportionally to the number of poles in order to achieve the desired speed. This will decrease the machine efficiency. The poor efficiency is due to the relatively large amount of end-winding existing in each stage.
3. The torque density and efficiency of a long machine is almost independent of the machine axial length because the back iron width at the two ends is negligible compared to the total machine length. In this case, both the machine torque and loss are almost proportional to the number of stages.
4. The investigated machines have a high power factor that first increases along with an increase of the pole number for low pole machines and then decreases. The reason is that for the low pole machines the active winding length increases rapidly with an increase of the pole number so that the back EMF still increases even though the leakage flux increases in the air gap, whilst for high pole machines, the fringing factor becomes dominant.

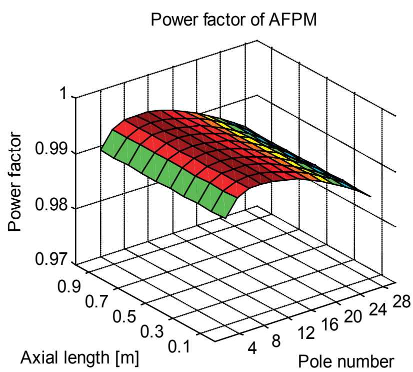

(a)

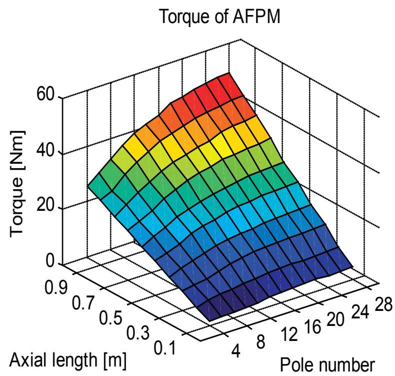

(b)

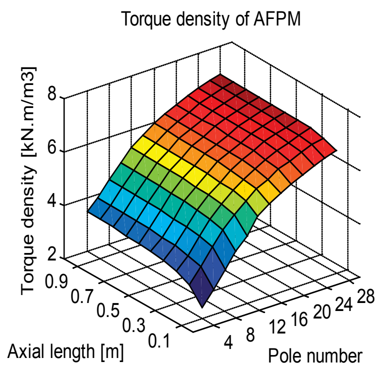

(c)

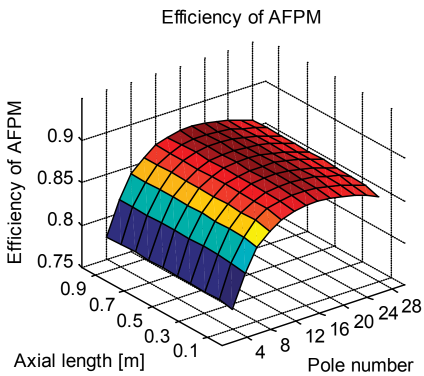

(d)

Fig. 4-15 Performance parameters of the AFPM machines (D_o = 100 mm) as functions of axial length and pole number (a) Power factor (b) Output torque (c) Torque density (d) Machine efficiency

4.5.3 TFPM Machines

A three-phase TFPM machine with an axial length between 0.1 and 1m actually consists of three single-phase machines with an axial length approximately between 0.033 and 0.33 m. These three single-phase machines are identical but with 120º phase shift among the phases. This is achieved by shifting the magnets 120 electrical degrees in the rotors among the phases. So it is sufficient to study a single-phase machine as shown in Fig. 4-16 to investigate the performance of the three-phase machine.

4.5.3.1 Magnetic Design

The stator tooth width and length are chosen to be the same as the magnets, and the air-gap flux density is limited to 0.9 T. The back iron of the U-bridge is chosen to be 1.8T in order to get maximum λ value and hence maximum current.

$$H_{sb} = \frac{\alpha_{pm} l_m B_g}{B_{sat}} \tag{4.54}$$

The width and height of the slots is chosen to be as

$$H_t = \frac{D_o}{2}(1-\lambda) - H_{sb} \tag{4.55}$$

And then

$$W_s = \frac{n_s I_{ph}}{k_f J H_t} \tag{4.56}$$

where I_{ph} is determined by (4.4).

The rotor iron thickness is

$$H_{rb} = \frac{\pi \alpha_{pm} D_o \lambda B_g}{2pB_{sat}} \tag{4.57}$$

The machine total length is

$$L_{tot} = 2l_m + W_s \tag{4.58}$$

where l_m is the magnet depth. In order to limit the flux leakage, the length should not be less than 10 mm.

The copper cross area and length are respectively evaluated by (4.59) and (4.60), this is no end winding in TFPM machines.

$$l_{cu} = \left(D_o \lambda + H_t\right)\pi \tag{4.59}$$

$$A_{cu} = W_s H_t \tag{4.60}$$

4.5.3.2 Optimal parameters

To find the optimal B_g, S = 20 kA/m, l_m =10 mm and k_σ =0.5 (this value is recalculated after machine design) are employed in (4.6). The flux density in the teeth is assumed to be equal to the air-gap flux density since they have the same cross-section area, while the flux density in the stack back iron is assumed to be 1.8 T. Fig. 4-17 shows an example of the torque densities for 6-pole machines with varying λ from 0.3 to 0.8 and B_g from 0.4 to 1 T. It is observed that the torque densities increase along with an increase of B_g, and for each B_g there is an optimal λ to obtain maximum torque density. B_g =0.9 T is chosen for all the considered machines.

To find the optimal λ value with respect to the machine axial length, B_g is fixed to 0.9 T, L_{tot} is varied from 0.03 to 0.33 m, and for each L_{tot} value, λ is varied from 0.3 to 0.8. For short machines, the magnet depth l_m is fixed to 10 mm, and the electrical loading S is determined by (4.36). For long machines, S is fixed to 20 kA/m, and l_m is calculated from (4.58). Fig. 4-18 shows the optimal λ values to obtain maximum torque densities with respect to the machine axial length and the calculated curve can simply be evaluated by

$$\lambda = 0.44 + 0.44 L_{tot} . \tag{4.61}$$

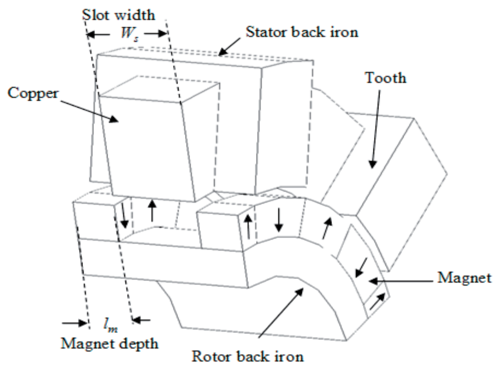

Fig. 4-16 A part of single-phase TFPM machine

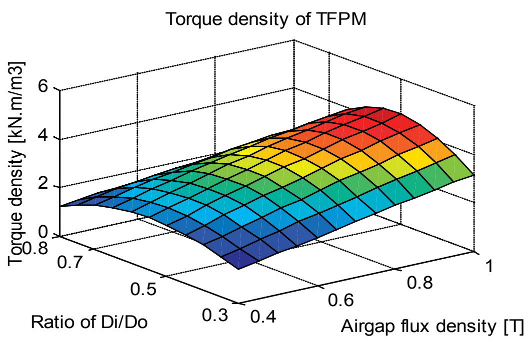

Fig. 4-17 The torque density with respect to the ratio λ and air-gap density (6-pole machines)

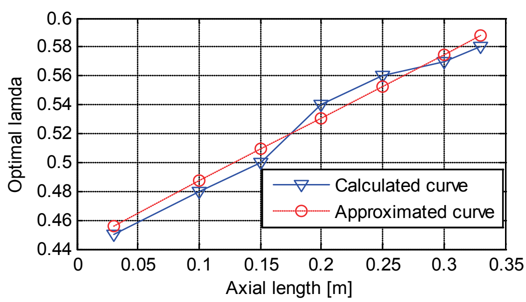

Fig. 4-18 Optimal λ with respect to the machine axial length

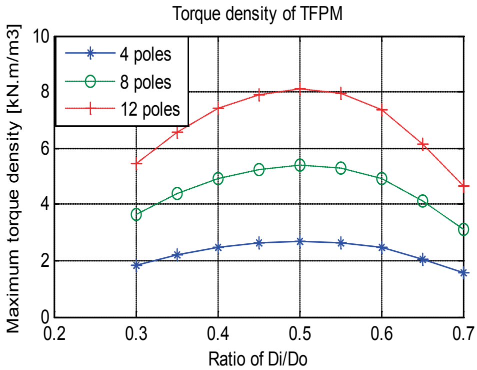

Fig. 4-19 The torque density with respect to the pole number p and ratio λ

The optimal values of λ are independent of the machine pole numbers as shown in Fig. 4-19 where three machines having an axial length of 0.15m with different poles of 4, 8, and 12, are investigated.

Now the air-gap density B_g =0.9 T is chosen for all the TFPM machines and the optimal values of λ are approximated by (4.61) according to their axial lengths, disregarding their pole numbers. Fig. 4-20 shows the power factor, output torque, torque density and machine efficiency with respect to the pole number and axial length for the three-phase TFPM machines. The maximum torque is up to 105 Nm as shown in Fig. 4-20 (b) and the maximum apparent power required is 18.3 kVA from (4.24).

4.5.3.3 Conclusions and explanations for the analytical results

1. The maximum torque density is proportional to the pole number as clearly seen from (4.6), in which the optimal value of λ is independent of the pole number.
2. The maximum torque density first increases along with an increase of the axial length and then decreases. For short machines the magnet depth l_m is fixed to 10 mm, the increased length contributes an increase of the available copper area that determines the electrical loading from (4.36) until the electrical loading up to 20 kA/m, so the torque density increases. For a further increased axial length, it mainly contributes to an increase of the total magnet depth $2l_{m.}$ As can be seen from (4.6) only half of the length l_m appears in the torque calculation, so the toque density decreases.
3. The machines have a much smaller power factor shown in Fig. 4-20 (a) compared to the RFPM and AFPM machines due to the high flux leakage.

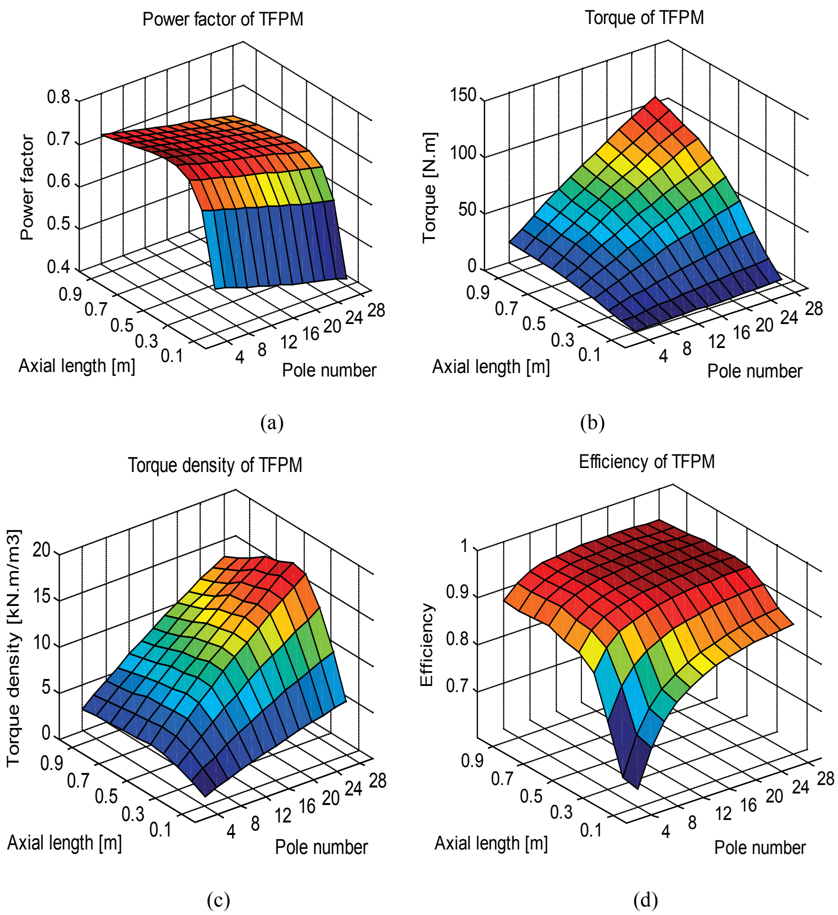

Fig. 4-20 Performance parameters of the TFPM machines (D_o = 100 mm) as functions of axial length and pole number(a) Power factor (b) Output torque (c) Torque density (d) Machine efficiency

4.6 FEM Simulations

From the analytical results presented in Fig. 4-8, an 8-pole RFPM machine could have both high torque density and high efficiency. To verify the result, 2D FEM simulations have been performed for an 8-pole RFPM machine with 24 stator slots as shown in Fig. 4-21. The machine parameters and simulated results are listed in Table 4-2, where the torque density and machine efficiency are calculated without taking the end winding into account, so the values are a little greater than those in Fig. 4-8. The FEM simulation results match satisfactorily with the analytical results.

Table 4-2 Machine Parameters and Results

Parameters	Analytical calculation	FEM
Outer diameter [m]	0.1	0.1
Active axial length [m]	0.5	0.5
Speed [rpm]	1000	1000
Pole number	8	8
Phase number	3	3
Slot/pole/phase	1	1
Stator back iron thickness [mm]	6.9	6.9
Ratio of inner and outer diameter	0.7	0.7
Tooth height [mm]	6.6	6.6
Magnet thickness [mm]	5	5
Relative permeability of iron	infinite	4000
Air gap length [mm]	1.5	1.5
Tooth width [mm]	5	5
Electrical loading [A/m]	10141	10141
Copper loss [W]	74.3	74.5
Stator iron loss [W]	71.9	68.1
Calculated torque [Nm]	29.7	30.2
Torque density [kNm/m^3]	7.6	7.7
Machine efficiency	95.5	95.7

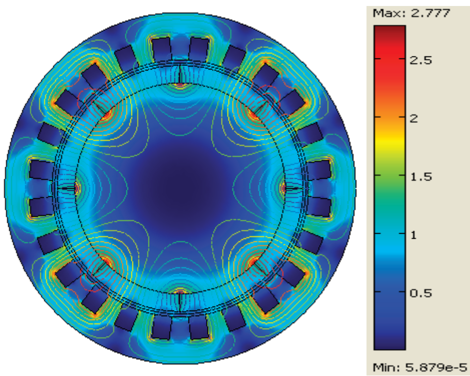

Fig. 4-21 Flux density distribution from the FEM simulation

4.7 Conclusions

By comparing the performances of the RFPM, multi-stage AFPM and three-phase TFPM machines shown in Fig. 4-8, Fig. 4-15 and Fig. 4-20, respectively, under the considered downhole conditions of a small current density, small electrical loading, high temperature, constant speed and without an external cooling system, the following conclusions are obtained:

1) Both the RFPM and the long TFPM machines may have high efficiencies.

2) Both the RFPM and AFPM machines have high power factors.

3) Due to the end winding existing in each stage and the small radial space confining the active winding length, the multi-stage AFPM machines, having low torque density and low efficiency, are not suitable for the downhole applications.

4) The high-pole TFPM machines present the advantage of high torque density as expected. The high-pole TFPM machines with an appropriate axial length may compete with the RFPM machines, but their low power factor limits the machines to low-speed applications.

5) The RFPM machines have simple constructions and therefore are more robust and more reliable than AFPM and TFPM machines.

6) The RFPM machines have reliable construction and can provide high torque density, efficiency and power factor. Therefore, they present the best performance for high- speed downhole applications.

5. Rotor PM and Stator PM Machines

The investigation in the previous chapter shows that RFPM machine topology presents high torque density, high efficiency and high reliability, and is therefore preferable for downhole applications. This type of machine has many construction variations. According to the magnet location, they can be classified as rotor-PM and stator-PM machines [103]. Each of them has several typical topologies. This chapter will briefly study the machine topologies and their main characteristics.

5.1 Rotor-PM Topologies

The rotor-PM topologies are most popular and have typically four different types: surface-mounted, inset, interior-radial and interior-circumferential topologies as shown in Fig. 5-1[103] [113].

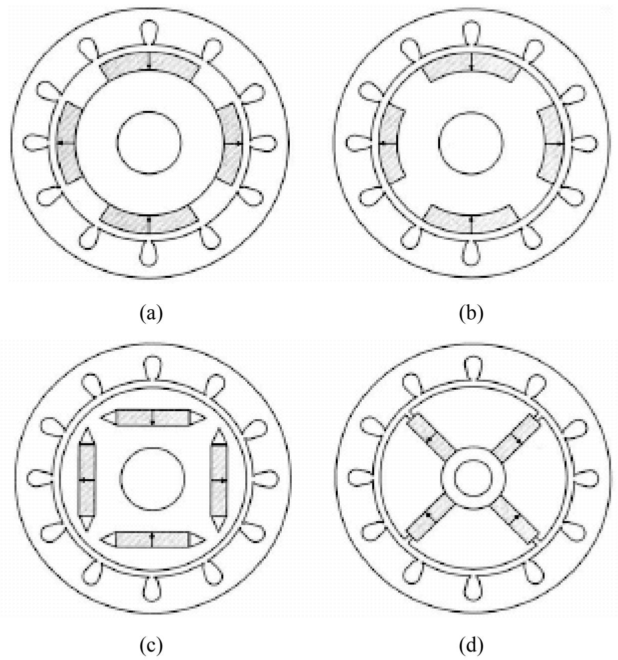

Fig. 5-1 Rotor PM machine topologies (a) Surface mounted (b) Inset (c) Interior radial (d) Interior circumferential [103]

The torque produced by the rotor PM machines consists of two components, the PM torque and the reluctance torque, which are expressed as

$$T = \frac{3}{2} p \left(\psi_{pm} I_q - (L_q - L_d) I_d I_q \right) \tag{5.1}$$

where ψ_{pm} is the winding flux linkage due to the PMs, L_d and L_q are respectively the d- and q- axis inductances, and I_d and I_q are separately the d- and q- axis currents.

5.1.1 Surface-mounted PM machine

The radially magnetized PMs are mounted on a steel-core rotor structure as shown in Fig. 5-1(a). Since the relative permeability of the magnet material is near unity, it acts as a large air gap. The effective air gap is therefore large, making L_d and L_q low and nearly the same. The reluctance torque of this machine is thus almost zero. Because of the constant magnetic gap between the stator and rotor, this machine can provide a square-wave flux distribution and is therefore suitable for brushless DC (BLDC) operation.

5.1.2 Inset PM machine

In the inset arrangement in Fig. 5-1(b), the PMs are inserted in the steel rotor structure. In this configuration, $L_d < L_q$, and with the same magnet size the peak torque developed with the inset magnets is higher than that of the surface-mounted one because of the reluctance torque determined by the second term in the right of (5.1). To produce the same torque, the thickness required for the inset magnet is smaller and hence L_d is larger [113].

5.1.3 Interior-radial PM machine

In this construction, the PMs are buried inside the rotor structure with radial magnetization as shown in Fig. 5-1(c). This machine therefore allows for a high-speed operation because the PMs are mechanically protected. With this configuration the q-axis inductance is larger than the d-axis inductance ($L_q > L_d$), and both L_d and L_q are larger than their corresponding values in the surface-mounted and inset type rotors.

5.1.4 Interior-circumferential PM machine

This arrangement of rotor PMs is shown in Fig. 5-1(d). Because of the flux-focusing effect, this machine yields higher air-gap flux density than the radial PM machine. The circumferential magnetization configuration is particularly advantageous for ferrite magnets that have low flux density because a substantial increase in air-gap flux density can be achieve. This machine is also suitable for high speed applications.

Both the inset and interior PM machines have a sinusoidal air-gap flux distribution and are therefore preferable for brushless AC (BLAC) operation.

5.1.5 Advantages and disadvantages

Disregarding the different rotor PM arrangements, the rotor-PM machines can offer the common advantage of high torque density and high efficiency. However, the magnets on the rotors usually need to be protected from the centrifugal force by employing a retaining sleeve, which is made of either stainless steel or non-metallic fiber. This degrades the cooling capability and hence limits the power density [109]. Furthermore, these machines suffer from the possibility of irreversible demagnetization by armature reaction flux, particularly in high temperature environment that is the case for downhole applications.

5.2 Stator-PM Topologies

The stator-PM machines have the PMs located in the stator as shown in Fig. 5-2. These machines are derived from conventional SRM by introducing PM into the stator to increase their power density and efficiency. These stator PM machines remain the characteristics of simple construction and mechanical robustness, while having significantly improved power / torque density and efficiency. The stator PM machines are typically categorized into doubly salient PM (DSPM), flux-reversal PM (FRPM) and flux-switching PM (FSPM) machines [66][67].

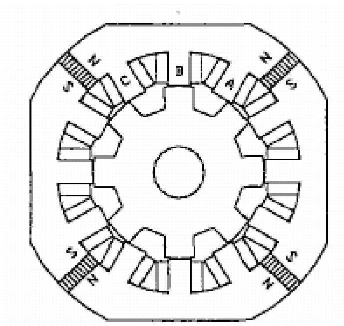

(a)

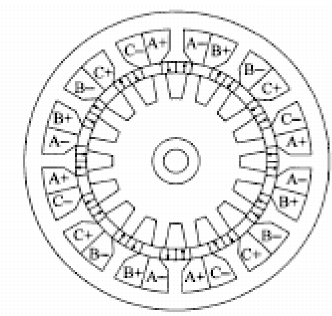

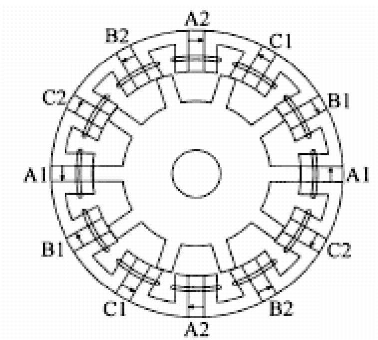

(b) (c)

Fig. 5-2 Stator RFPM machines (a) DSPM [108] (b) FRPM [96] (c) FSPM [56]

5.2.1 DSPM Machine

Fig. 5-2 (a) shows a typical DSPM machine topology [108], in which the magnets are inset in the stator back iron and concentrated windings are employed. Although this machine has a doubly salient construction, the PM torque significantly dominates the output torque, hence exhibiting low cogging torque. Fig. 5-3 (a) presents its operation principle. The variation of the flux linkage in each coil with respect to the rotor position is unipolar. The square-wave EMF makes this machine suitable for conventional BLDC operation. By skewing the rotor, it can also be run in BLAC mode. The main drawback of this machine is the relatively low torque density, as resulted from the unipolar flux linkage.

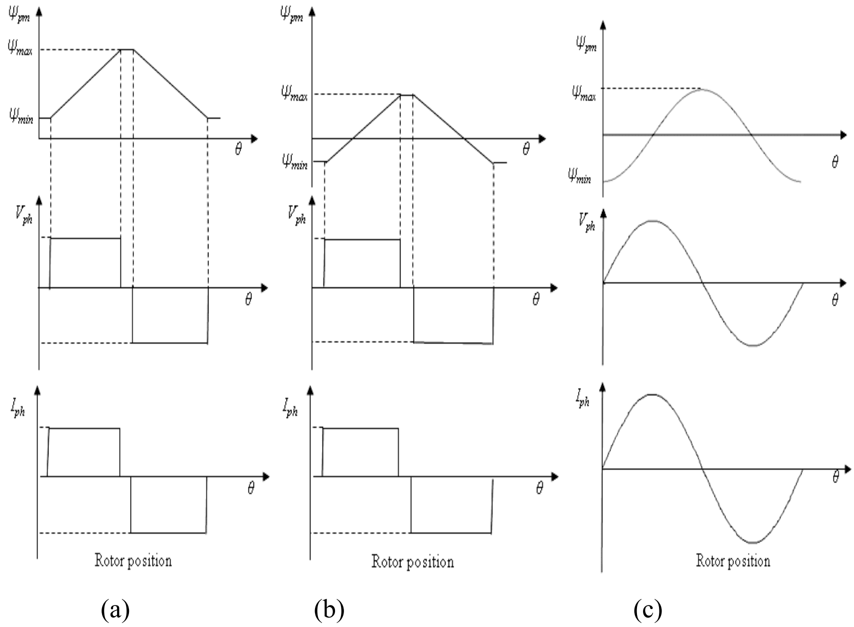

Fig. 5-3 Operation principle of (a) DSPM (b) FRPM (c) FSPM

5.2.2 FRPM machine

The FRPM machine in Fig. 5-2 (b) has the magnets located on the surface of the stator teeth. On each stator tooth surface there is a pair of PMs with different polarities. Unlike DSPM machines, the phase flux linkage of a FRPM machine is bipolar as presented in Fig. 5-3 (b). And hence its torque density is higher than that of a DSPM machine. However, the air-gap flux density in a FRPM machine is limited by the PM remanence B_r, which constrains the machine torque capability. The PMs on the surface of the stator teeth are more prone to partial demagnetization like the stator PM machine, and the flux variation in the PMs results in significant magnet eddy-current losses [103]. Moreover, the surface-mounted PMs make the machine less robust compared to the DSPM machine. This machine prefers to BLDC operation.

5.2.3 FSPM machine

Fig. 5-2 (c) depicts a FSPM machine construction [56] [68], in which the circumferentially magnetized PMs are inset between two stator teeth. The magnetization is reversed in polarity from one magnet to the next, hence it enables flux focusing. The air-gap flux density can reach up to 2.5 T, much higher than that of a DSPM machine, 1.5 T [68], and a FRPM machine, limited by B_r. In addition, the phase flux-linkage variation is bipolar like the FRPM machine. Hence, a FSPM machine can have much higher torque capability than a DSPM machine. The investigation presented in [68] shows a FSPM machine can provide 2.45-3 times higher torque than a DSPM machine with the same current density or copper loss. Thanks to the flux focusing, a FSPM machine can also provide higher torque density than a FRPM machine with the same current density as shown in Fig. 5-4 [110]. Furthermore, since the windings and the magnets are magnetically in parallel, rather than in series as in FRPM machines, the influence of the armature reaction field on the working point of the magnets is almost eliminated. As a result, the electric loading and the specific torque capability of the FSPM machine can be higher than that of the FRPM machine.

The sinusoidal back-EMF waveform as shown in Fig. 5-3(c) indicates that the machine is suitable for BLAC operation.

In summary, among the above-mentioned stator-PM prototypes the FSPM machine topology presenting both high torque capability and reliability is therefore chosen to compare with the rotor-PM machines for downhole applications.

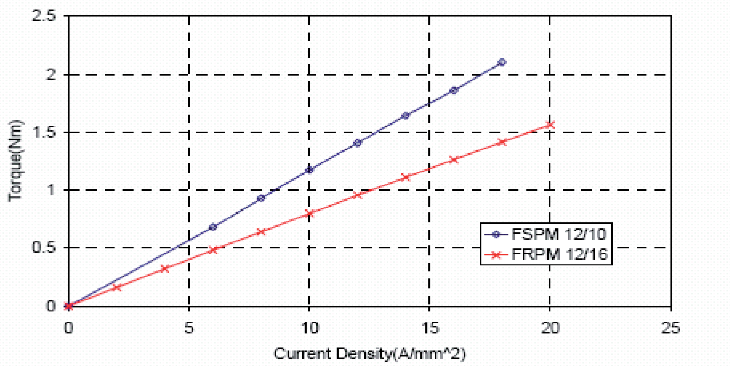

Fig. 5-4 Torque comparison of 12/10 FSPM and 12/16 FRPM machines [110]

5.3 Comparison of stator PM machines and FSPM machines

Some comparative studies about rotor-PM machines and FSPM machines have been presented in [54], [69] and [103]. The advantages of the FSPM topology against the rotor-PM topologies are as follows:

1) Better cooling capability: PMs in the stator make it easier to dissipate heat from the stator surface, thereby, to limit the temperature rise of the magnets.

2) Less de-magnetization field from armature reaction because the windings and the magnets are magnetically in parallel. As a result, the electric loading and the specific torque capability of the FSPM machine can be higher.

3) Comparative or even better torque capability based on 1) and 2).

4) Only steel on the rotor makes the FSPM machines more robust.

Additionally, the FSPM machines have concentrated windings, which result in less copper loss and are also easy to manufacture.

However, the FSPM machines introduce additional rotor iron loss caused by the flux variation in the rotor iron. This may lead to a lower efficiency. For the relatively low speed applications considered here (1000 rpm), the iron loss is normally minor compared to the copper loss. So the efficiency difference should not be significant.

Table 5-1gives the comparisons.

Table 5-1 Performance comparison between FSPM and rotor-PM machines

	Torque density	Reliability	Cooling capability	Efficiency
FSPM machine	Equal /better	Better	Better	Less
Rotor-PM machine	Equal /less	Less	Less	Better

5.4 Conclusion

This chapter has studied different rotor-PM and stator-PM machine topologies. In general, the former has the capability of providing high torque and efficiency. Some stator PM machines have already been presented for downhole applications as mentioned in chapter 3. FSPM machine topology, one of the stator-PM machines, also presents the same high torque capability as the rotor-PM machines (even higher) with higher reliability. It is preferable for reliability premium applications and presents a promising potential for downhole applications as an alternative to the stator PM machines. Therefore it is chosen to be further investigated in next chapter.

6. Flux Switching Permanent Magnet Machines

Today FSPM machines have been presented for different applications, such as in aerospace, automotive and wind energy applications [60][93][94]. Due to the doubly salient construction, the performance of a FSPM machine is very sensitive to the combination of the stator and rotor pole numbers. This chapter firstly reviews different FSPM machines and their characteristics. Then a FSPM machine with 12 stator teeth and 14 rotor poles (12/14) is studied in detail and compared to the same machine but with 10 rotor poles. Their back EMF, cogging torque, electromagnetic torque and machine inductance are investigated by FEM analysis and measurements. The 12/14 pole prototype machine is built based on an existing 12/10 pole machine. Finally, the 12/14 pole machine is optimized by FEM analysis to further improve its output torque. Most content in this chapter has been presented in [3].

6.1 Review of different FSPM machines

In general, the stator and rotor pole number of a FSPM machine should be chosen as:

$$P_s = k_1 m \ (k_1 = 1, 2...) \tag{6.1}$$

$$P_r = P_s \pm k_2 \ (k_2 = 1, 2...) \tag{6.2}$$

where P_s and P_r are respectively the stator pole and rotor pole numbers, k_1 is an integer number when m is an even number, but for an odd number m it should be an even number. In order to balance the radial magnetic force, P_r should be an even number [55]. To obtain the maximum torque, P_r should be chosen close to P_s.

Different FSPM machines with various stator and rotor pole combinations and their characteristics have been presented [53][55] [57] [95][96], and are summarized below:

- A 4/2 one-phase FSPM machine shown in Fig. 6-1 (a) was presented for low cost and low torque applications [95][111].
- An 8/6 two-phase FSPM machine in Fig. 6-1 (b) was investigated in [112].
- 12/10 three-phase FSPM machine topology has been presented for different applications because of its essentially sinusoidal three-phase back-EMF suitable for standard control systems and relatively small torque ripple [53][56][58]. 12/14 and 12/16 machine topologies were also studied [55] [57]. Compared to the 12/10 machine, the former can provide higher torque, whilst the latter can't. The 12/14 machine also has a sinusoidal back EMF as the 12/10 one.
- 6/4, 6/5 and 6/8 machine constructions in Fig. 6-2 were proposed and studied [57] [110] in order to reduce the iron loss and magnet eddy-current loss whilst maintaining the torque capability of the three-phase FSPM topologies

with 12 stator poles. At the same mechanical speed smaller rotor pole number means less electrical frequency, and hence less iron loss and magnet eddy current loss. The 6/5 machine also has a symmetrically sinusoidal three-phase back-EMF and presents higher torque capability than the other two. Compared to the 12/10 machine, the torque capability of the 6/5 machine is also slightly higher [110]. But this machine presents a significantly unbalanced radial force due to the odd rotor pole number [57], which is undesirable for downhole applications. The unbalanced radial force can be reduced by skewing the rotor. However, skewing the rotor not only increases the manufacturing complexity, but also degrades the machine's torque capability.

- Multiphase FSPM machines (four, five and six phases) with high number of stator and rotor poles were studied for aerospace applications [94]. These machines are considered unsuitable for downhole applications because of two reasons: a) The small well sizes constrain the machine within low pole numbers to limit the flux leakage in the air gap; b) Non-standard complex control systems are required.

Among the above-mentioned machines the three-phase 12/10 and 12/14 machines are chosen to be further investigated for downhole application, based on their following advantages:

- Sinusoidal three-phase back EMF suitable for standard control systems.
- High torque capability
- Balanced radial force
-

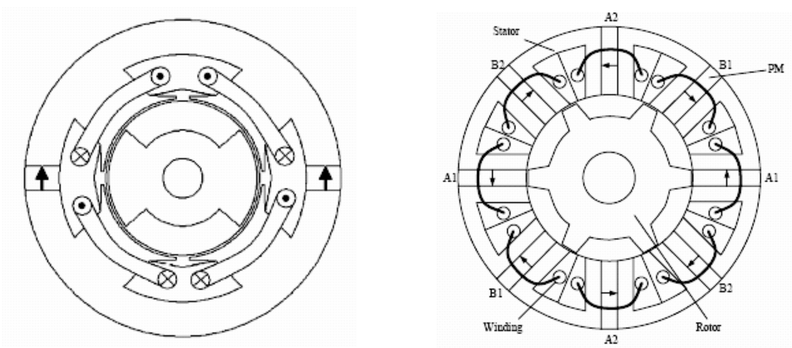

(a) (b)

Fig. 6-1 FSPM machines (a) 4/2 one-phase [95] (b) 8/6 two-phase [112]

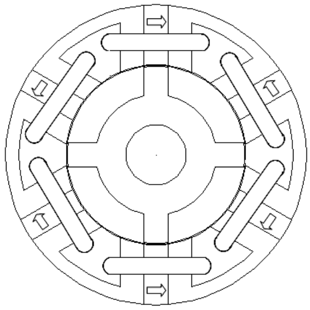

(a)

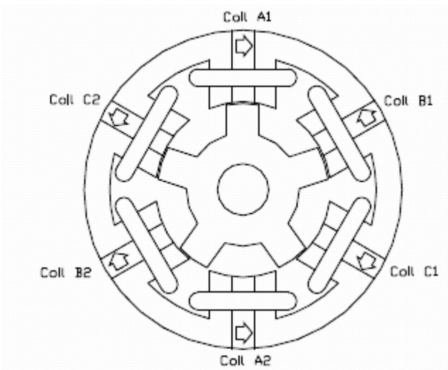

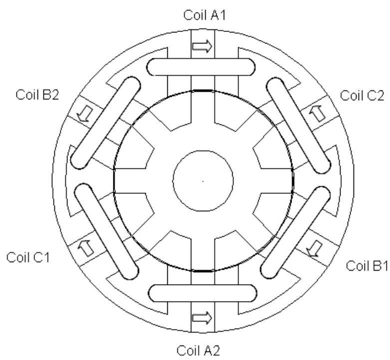

b) (c)

Fig. 6-2 Different three-phase FSPM machines (a) 6/4 (b) 6/5 (c) 6/8 [110]

6.2 Machine Construction

Fig. 6-3 shows two initially designed 12/10 and 12/14 pole three-phase FSPM machines, in which the stator tooth width W_{st}, permanent magnet thickness l_{pm}, stator back iron thickness H_{sb}, stator slots opening W_s and rotor tooth width W_{rt} are chosen to be the same and equal to ¼ the stator pole pitch as shown in Fig. 6-4. Both machines have exactly the same physical construction, magnet arrangement and winding design except their rotor pole numbers. In both machines each phase winding consists of four coils and each coil is concentrated around two stator teeth with a magnet inset in between. The magnets are circumferentially magnetized and the magnetization is reversed in polarity from one magnet to the next. For each phase the flux in coils 1 and 2 are respectively the same as that in the corresponding phase coils 3 and 4 due to the symmetrical machine constructions.

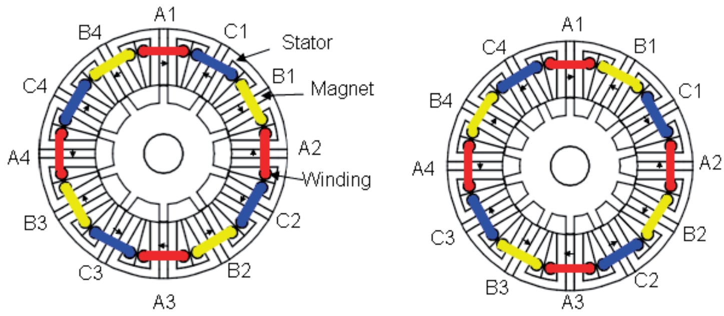

(a) (b)

Fig. 6-3 (a) 12/10 pole (b) 12/14 pole machines

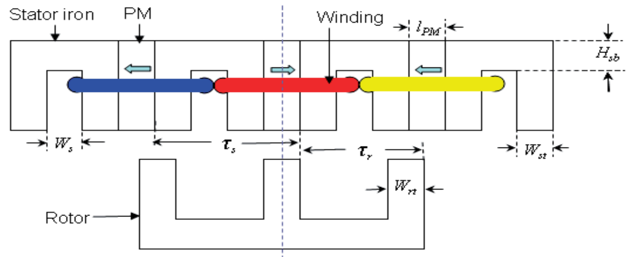

Fig. 6-4 Part of the machine in a plain form

6.3 Operating principle

The electromagnetic torque of a PM machine can be expressed as [97]

$$T_{em} = \frac{\partial W_c}{\partial \theta}\bigg|_{\text{i=constant}} = N_s i \frac{d\Phi_{pm}}{d\theta} + \frac{i^2}{2}\frac{dL_s}{d\theta} - \frac{\Phi_{pm}^2}{2}\frac{dR_g}{d\theta}. \qquad (6.3)$$

where W_c is the co-energy, θ is the mechanical angle, i is the phase current, Φ_{pm} is the mutual flux linking the magnets and the phase coils, N_s is the number of turns, L_s is the phase inductance and R_g is the air-gap reluctance.

The first term in the right side of (6.3) is the PM torque component due to the interaction between the PM flux linkage and the armature current. The second term is the reluctance torque component caused by the inductance variation at different rotor position. For the FSPM machines, it is negligible compared to the PM torque component [53]. The last term in (6.3) is the cogging torque, for conventional PM machines, it is produced by the interaction between the stator slots and the rotor permanent magnets (the source of the varying air-gap reluctance). However, for the FSPM machines having doubly salient topology with magnets in the stator, the cogging torque is due to the interaction of doubly salient stator and rotor structures. As in the conventional PM machines, the average of cogging torque in FSPM machines is also zero and therefore does not contribute to the average output torque. So it is only the PM torque component that dominates the output torque, which can be expressed as (6.4) by insetting $\theta = \omega_m t$.

$$T = N_s i \frac{d\Phi_{pm}}{d\theta} = \frac{N_s i}{\omega_m} \frac{d\Phi_{pm}}{dt}. \tag{6.4}$$

where ω_m is the mechanical angular speed.

Both machines have the same operating principle, so the 12/14 machine as an example is analyzed.

In the FSPM machines each coil is wound around two stator teeth with a magnet inset in between, so the flux direction in the two stator teeth is always opposite as shown in Fig. 6-5. The effective flux in the coil is therefore the summary flux in the two stator teeth, and its value varies with respect to the rotor position. In Fig. 6-5 (a) and (c), the fluxes in the two teeth are equal but in opposite direction, so the effective flux in the coil is zero. In Fig. 6-5 (b) and (d) the effective flux reaches its maximum value, but their flux directions are opposite.

In order to simplify the analysis of flux variation, the following assumptions are made:

- The iron has infinite permeability.
- The air-gap flux is evenly distributed under the overlapped area of the stator teeth and rotor teeth.
- The fringing flux is neglected.

With the above assumptions, the flux through a stator tooth increases linearly when a rotor tooth begins overlapping with the stator tooth until they fully align. In this case, the flux variations coupling coils A_1 and A_2 with respect to the rotor position can be analytically figured out and are shown in Fig. 6-6(a). The summary flux variation in the two coils is basically sinusoidal. And among the flux waveforms of three phases there is 120° electrical degree shift as given in Fig. 6-6(b) in which the summary fluxes in coils A_1 and A_2, B_1 and B_2, as well as C_1 and C_2 are presented. It should be noted that the positions of phase *b* and *c* in the 14-pole machine have interchanged compared to those in the 10-pole one as shown in Fig. 6-3.

To take the iron saturation and fringing flux into account, FEM simulations are employed to investigate the flux variation. Fig. 6-7, as an example, shows the summary flux in coils A_1 and A_2, which is essentially sinusoidal. Its period expressed in mechanical degree is

$$\theta_{\tau r} = \frac{2\pi}{P_r}. \tag{6.5}$$

where P_r is the rotor pole number.

Then the flux that couples one phase coil can be expressed as

$$\Phi_{pm} = \Phi_{max} \sin(P_r\theta)\,. \tag{6.6}$$

where Φ_{max} is the peak value of the summary flux in the four coils of one phase.

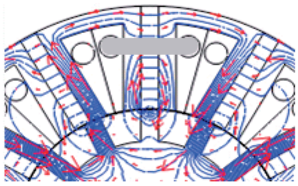

(a)

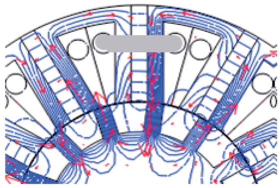

(b)

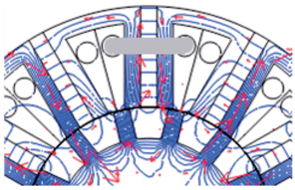

(c)

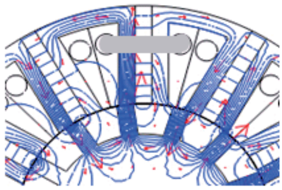

(d)

Fig. 6-5 Flux in a coil at different rotor position (a) zero flux coupling the coil (b) maximum flux (c) zero flux coupling the coil (d) maximum flux in opposite direction of (b)

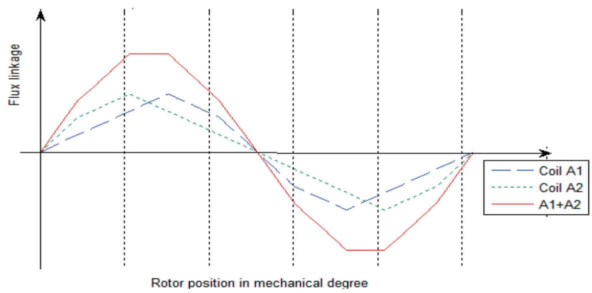

(a)

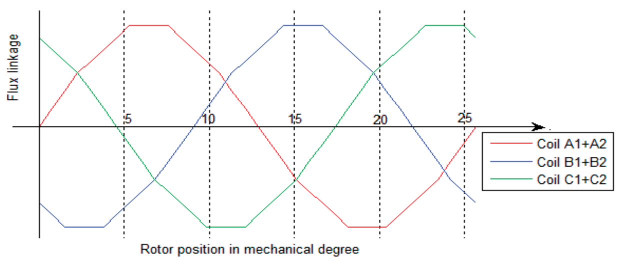

(b)

Fig. 6-6 (a) Flux in coil A_1, A_2 and A_1+A_2 (b) Flux in A_1+A_2, B_1+B_2 and C_1+C_2 of 12/14 pole machine by analytical calculations

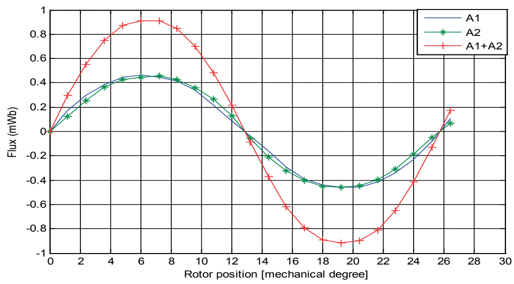

Fig. 6-7 Flux in coil A_1, A_2 and their summary by FEM

It is shown in Fig. 6-7 that the summary flux in coils A_1 and A_2 reaches its maximum value when the rotor rotates a distance of τ_r /4 from the zero flux position (q-axis position) in Fig. 6-5 (a). At the maximum flux position, d-axis position, the fluxes in coil A_1 and A_2 are the same, $\Phi_{A1}(\tau_r/4) = \Phi_{A2}(\tau_r/4)$, as shown in Fig. 6-8. So the maximum summary flux in the four coils of phase a can be calculated as

$$\Phi_{\max} = 2\left(\Phi_{A1}(\tau_r/4) + \Phi_{A2}(\tau_r/4)\right) = 4\Phi_{A1}(\tau_r/4). \tag{6.7}$$

Fig. 6-9 depicts the flux paths coupling coil A_1 at the q-axis position. The effective flux $\Phi_{A1}(\tau_r/4)$ for torque production can be evaluated by

$$\Phi_{A1}(\tau_r/4) = \Phi_{1e} + \Phi_{2e} - \Phi_{3l}. \tag{6.8}$$

where Φ_{1e} and Φ_{2e} respectively represent the effective flux in coil A_1 produced by magnets *PM1* and *PM2* (see Fig. 6-9), whilst Φ_{3l} represents the flux produced by *PM3* passing through stator tooth *P4*.

Eq. (6.8) can be re-written as

$$\Phi_{A1}(\tau_r/4) = k_\sigma W_{st} L B_t. \tag{6.9}$$

where W_{st} is the stator tooth width, B_t is the average flux density in the top of stator tooth *P3*, k_σ is the flux leakage factor taking the leakage flux Φ_{2l} and Φ_{3l} into account, and k_σ is always less than unity and evaluated by

$$k_\sigma = \frac{B_t W_{st} L - \Phi_{2l} - \Phi_{3l}}{B_t W_{st} L}. \tag{6.10}$$

Assuming all the coils of each phase are connected in series, then the induced phase EMF can be evaluated by

$$e(t) = \frac{n_s}{4}\frac{d\Phi_{pm}}{dt}. \tag{6.11}$$

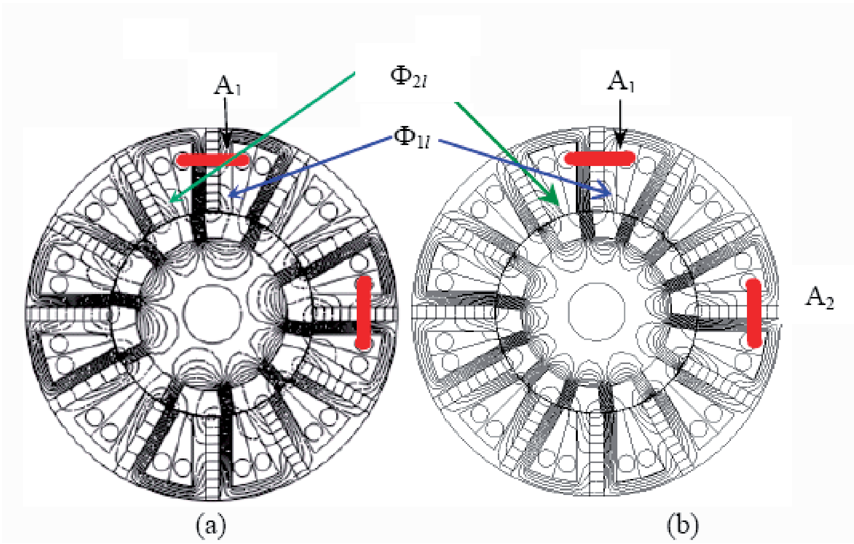

Fig. 6-8 Flux distribution at *d*-axis position of coil A (a) 12/10 pole machine (b) 12/14 pole machine

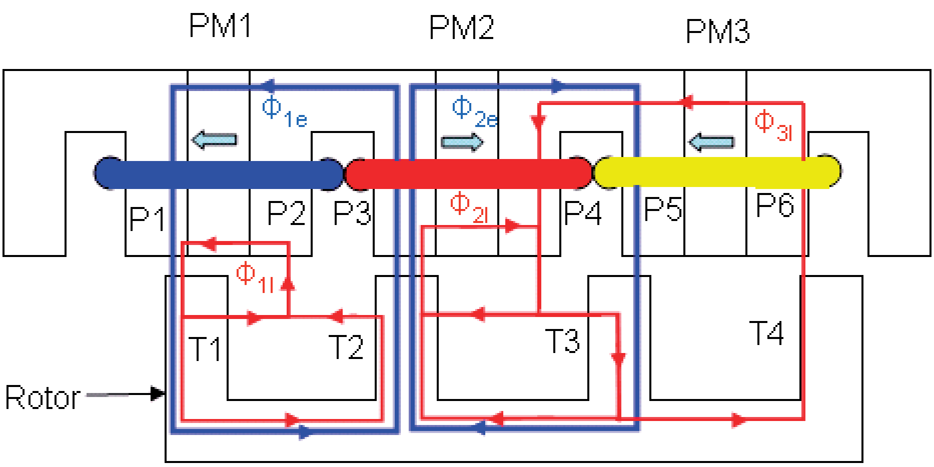

Fig. 6-9 Flux paths coupling winding shown in Fig. 6-8

Substituting (6.6), (6.7) and (6.9) into (6.11) and expressing θ in terms of ω_m and t yields

$$e(t) = k_\sigma n_s P_r \omega_m W_{st} L B_t \cos(P_r \omega_m t)\,. \qquad (6.12)$$

Assuming the phase current is in phase of the induced phase voltage, the output torque produced by a FSPM machine can be written as (6.13) from (6.4).

$$T = \eta m E_{ph} I_{ph} / \omega_m . \tag{6.13}$$

where m is the phase number, η is the machine efficiency to take iron loss and copper loss into account, E_{ph} is the *rms* value of the induced phase voltage and can be expressed as (6.14) from (6.12). I_{ph} is the *rms* value of the phase current and is determined by (4.15).

$$E_{ph} = k_\sigma n_s P_r \omega_m W_{st} L B_t / \sqrt{2} \tag{6.14}$$

Substituting (6.14) and (4.4) into (6.13) yields

$$T = \frac{\sqrt{2}\pi}{4} k_\sigma P_r \lambda D_o S W_{st} L B_t \eta . \tag{6.15}$$

6.4 Parameter Study

Since both machines have the same stator and winding arrangement, the only difference is the pole number, which means all the parameters in (6.15) are the same for both machines except P_r, B_t and k_σ. This section will investigate how the different poles P_r influence the torque parameters of B_t and k_σ.

6.4.1 Flux density in the stator teeth

To study B_t, different magnet materials with remanence flux density B_r from 0.6 to 1.2 T are used in these two initial machines and 2D-FEM analysis is employed. Fig. 6-10 shows the flux density B_t of both machines with different magnet materials. It is observed that the value of B_t in the 12/10 machine is always higher than that in the 12/14 one with the same magnet material. This is because the shorter rotor pole pitch of the 12/14 machine, which is inversely proportional to P_r, leads to an increased leakage flux from the neighbor stator teeth to the rotor as clearly seen in Fig. 6-8.

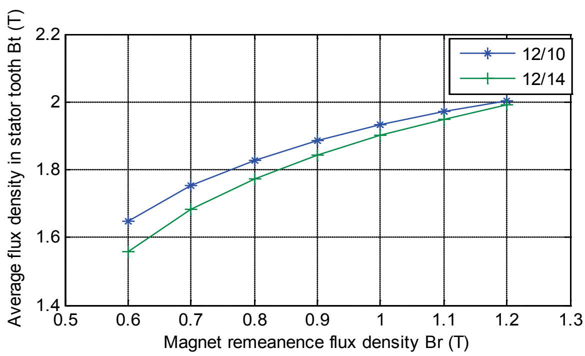

Fig. 6-10 Flux density B_t of both machines at d-axis position with different magnet material

6.4.2 Flux leakage factor

Fig. 6-11 presents the leakage factor k_σ of both machines at different flux density of B_t by FEM simulations. The leakage factor of the 12/10 pole machine is also always greater than that of the 12/14 one at the same B_t value because of the increased flux leakage afore-mentioned. And for both machines k_σ decreases along with an increase of B_t due to the increased saturation in the stator teeth.

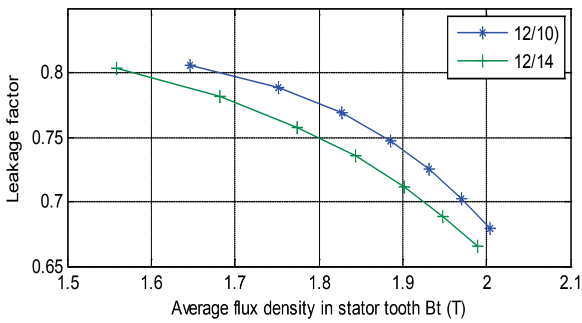

Fig. 6-11 Leakage factor k_σ of the two machines at d-axis position at different flux density B_t

6.4.3 Product of B_t and k_σ

Since the output torque given by (6.15) depends on both B_t and k_σ, their product value directly indicating the torque capability of the machines is provided in Fig. 6-12 as the function of B_t. It is shown that the product value reaches its peak when B_t is around 1.85 T for the 12/14 machine, whilst it is around 1.9 T for the 12/10 machine. With a further increased B_t, the corresponding effective flux in each machine begins decreasing due to the rapidly increased leakage flux caused by the iron saturation even the total flux through the tooth top increases as shown in Fig. 6-13.

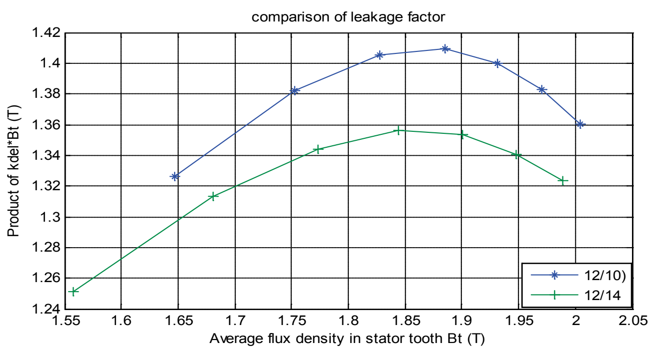

Fig. 6-12 Product of k_σ and B_t at different B_t of 12/10 and 12/14 machines

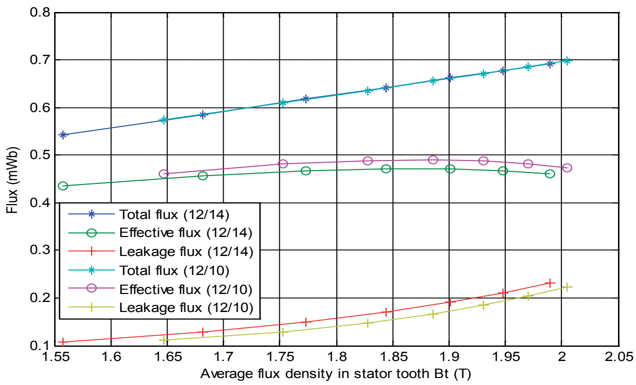

Fig. 6-13 The total, effective and leakage flux at *d*-axis position at different flux density B_t of 12/10 and 12/14 machines

6.5 Study of Two Prototype Machines

Since we do not know so much about the characteristics of both topologies, a 12/14 pole machine is simply built based on an existing 12/10 pole machine prototype presented in [62] in order to study and compare the two machine topologies practically. The 12/10 pole machine prototype has a wider diameter and lower rated speed than the discussed case as shown in Table 6-1, and has been optimized according to the research presented in [53] and [56]. The 12/14 machine is made by simply replacing a 14 pole rotor instead of the 10 pole one, keeping the rotor tooth width unchanged. In order to easily assemble the machine, a thin stator iron bridge with a thickness of 1.5 mm was added between U-shape stator cores as shown in Fig. 6-14. The FEM simulations show the bridges just slightly degrade the machine output torque 1.1%, caused by the leakage flux through the highly saturated iron bridges.

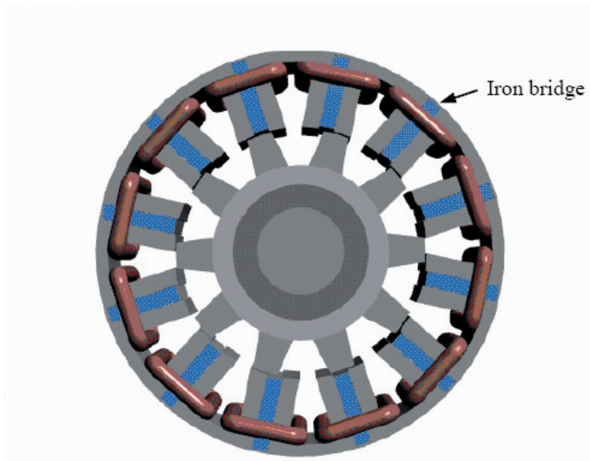

Fig. 6-14 3D view of the 12/10 pole prototype

6.5.1 Simulations and Measurements

Fig. 6-15 shows the machine prototypes made in laboratory. The characteristics of these two prototypes are firstly investigated by 2D FEM simulations and then compared with experimental measurements. For the discussed machines having a relatively small axial length, the influence of end effect that is not included in the 2D FEM simulations is significant and can decrease the flux linkage, the phase back EMF, and the output torque by ~10% according to the research presented in [53]. To simply take the end effect into account, the presented simulation values of the back-EMF and the output torque have been corrected by multiplying 0.9.

Table 6-1 PROTOTYPE PARAMETERS

Phase number	3
Number of stator pole	12
Number of rotor pole	10 or 14
Outer stator diameter	210 mm
Inner stator diameter	130 mm
Stator back iron width	6.3 mm
Stator tooth width	8.9 mm
Stator iron bridge	1.5 mm
Rotor tooth height	18.3 mm
Rotor tooth width top/bottom	13/18 mm
Air gap length	1 mm
Active axial length	50 mm
Rated speed	400 rpm
Rated phase current (rms)	3.4A
Number of turns per pole	174
Magnet width	8 mm
Magnet remanence	1.16T
Magnet relative permeability	1.05
Specific iron loss factor	2.2W/kg

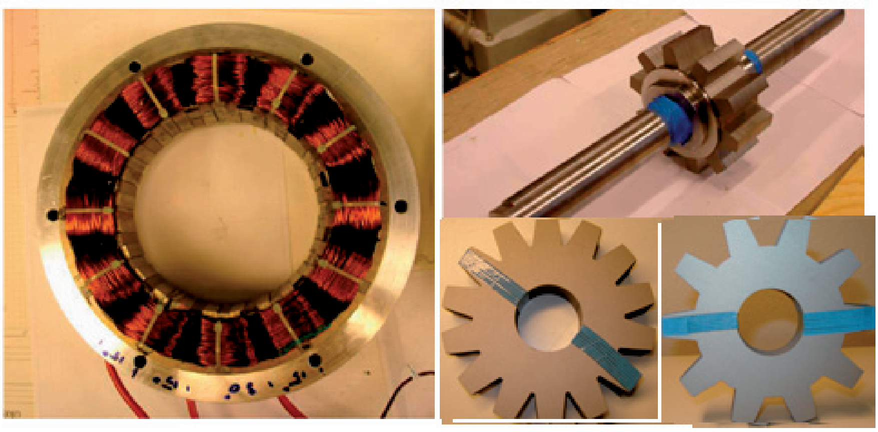

(a) (b)

Fig. 6-15 Machine prototype (a) stator (b) rotors

6.5.2 Back EMF

Fig. 6-16 and Fig. 6-17 respectively show the induced back EMFs at no-load condition for the 12/10 pole and 12/14 pole prototype machines by both FEM calculations and experimental measurements. Both machines have essentially sinusoidal back EMF waveforms and they are symmetrical for three phases. Their total harmonic distortions (THD) are investigated by Fourier analysis and are respectively around 1.5% and 1.2%. It is also observed that the induced back EMF of the 12/14 pole machine is only ~10% higher than the 12/10 pole machine. It should be mentioned that the rotor tooth width was optimized for the 12/10 pole machine to improve the torque, which results in that the top width of the rotor tooth is 46% wider than the stator teeth width [62]. For the 12/14 machine, such wide rotor width leads to enormous flux leakage and hence reduces the torque capability. This will be presented later in the subsection of *Optimization of 12/14 pole machine*.

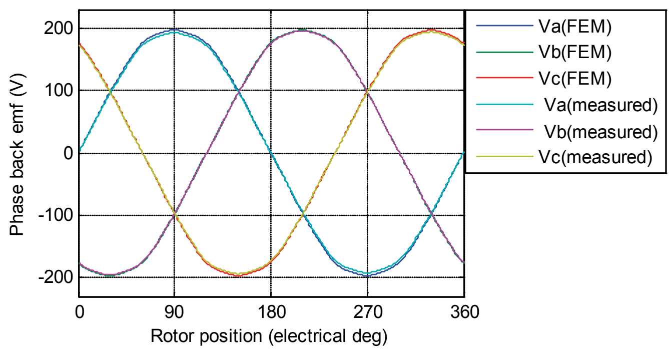

Fig. 6-16 Induced phase back EMF of the 12/10 pole machine

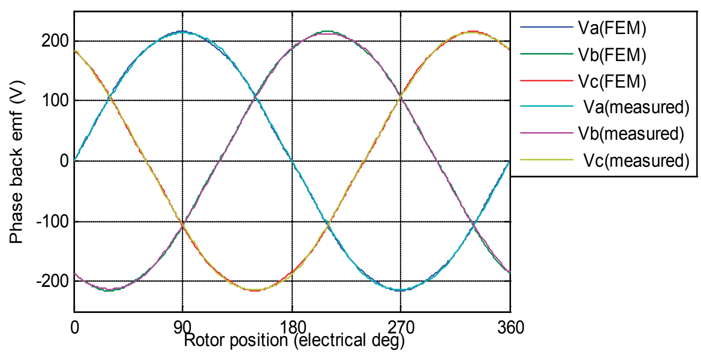

Fig. 6-17 Induced phase back EMF of the 12/14 pole machine

6.5.3 Cogging torque

Though the cogging torque does not contribute to the average output torque, it causes torque ripple and further speed pulsation, mechanical vibration and acoustic noise, particularly at low inertia and low speed, so it is necessary to investigate it.

Fig. 6-18 and Fig. 6-19 individually depict the cogging torque of the 12/10 and 12/14 pole machines by both FEM calculations and measurement with respect to the rotor position. The result shows that both machines have a similar maximum cogging torque around 1 Nm (the 12/14 pole machine has slightly less cogging torque).

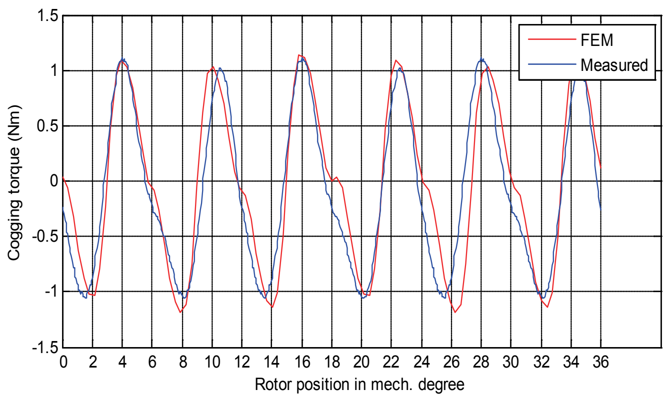

Fig. 6-18 Cogging torque of the 12/10 machine

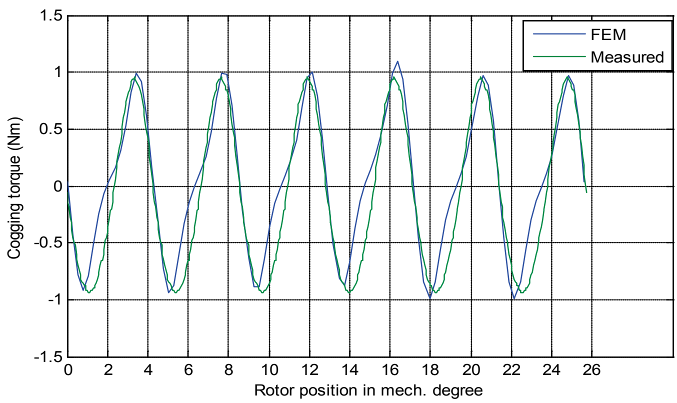

Fig. 6-19 Cogging torque of the 12/14 machine

6.5.4 Output torque

Fig. 6-20 and Fig. 6-21 separately present the output torques of both prototype machines at the rated current of 3.4A by FEM calculations and measurements. The average torque of the 12/14 pole machine is around 11% higher than that of the 12/10 pole machine. And the former, having a peak to peak torque ripple in percentage of 5.1%, is also less than the latter, 8.5%.

Comparing Fig. 6-20 and Fig. 6-21 respectively with Fig. 6-18 and Fig. 6-19, it is observed that the torque ripple waveform of each machine is similar to its corresponding cogging torque waveform, which indicates that the torque ripple is mainly caused by the cogging torque.

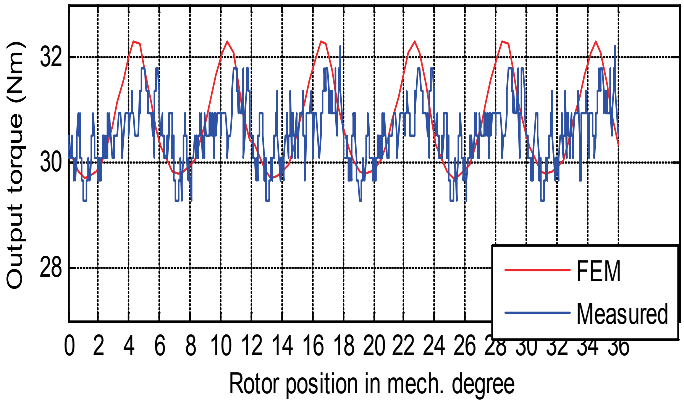

Fig. 6-20 Output torque of the 12/10 machine

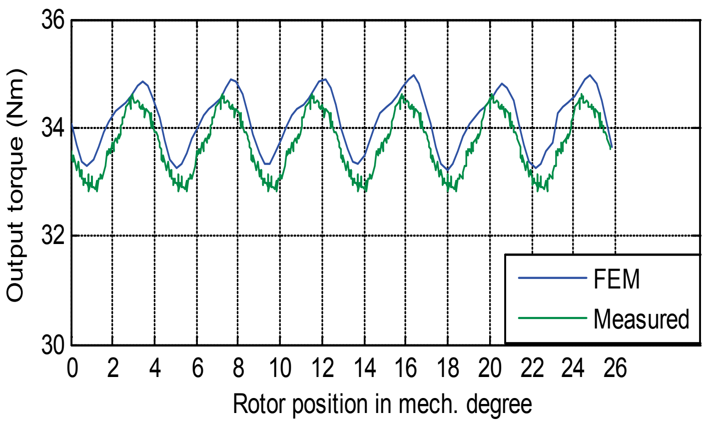

Fig. 6-21 Output torque of the 12/14 machine

6.5.5 Inductance

The machine inductance is investigated by the method presented in [98] and the details were given in [62]. Fig. 6-22 and Fig. 6-23 respectively show the *d*- and *q*-axis inductances of the two machines by both FEM simulations and measurements. Due to the additional rotor iron area along the rotor circumference in the 12/14 pole machine, its inductance is about 15% higher than that of the 12/10 pole one.

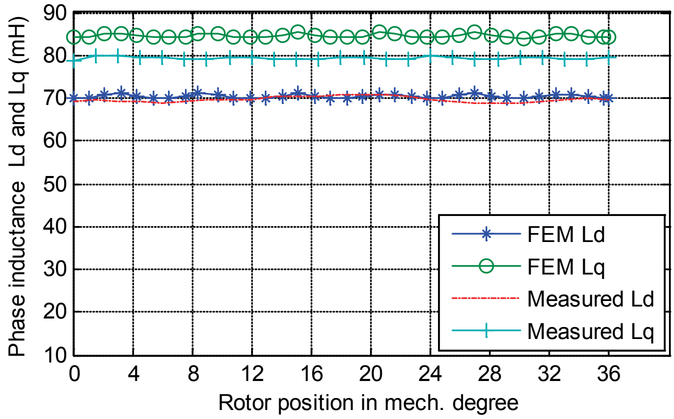

Fig. 6-22 Inductance of the 12/10 pole machine

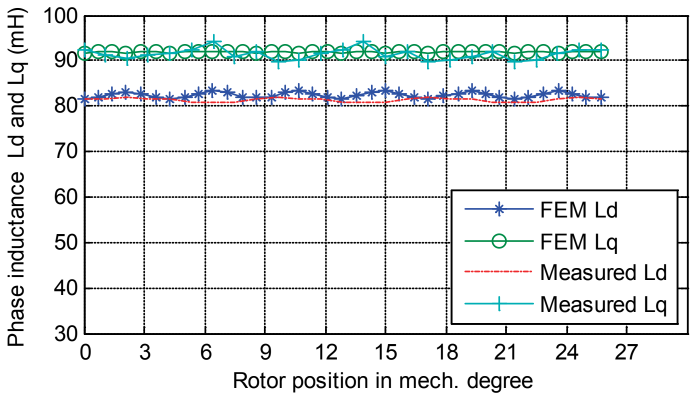

Fig. 6-23 Inductance of the 12/14 pole machine

6.5.6 Efficiency

Both machine efficiencies are also measured at the rated speed and current. The 12/14 pole machine has an efficiency of 85%, which is slightly higher than that of the 12/10 pole machine, 84%.

6.6 Optimization of 12/14 Pole Machine

It is clearly shown in Fig. 6-24 that the flux leakage from the neighbor stator teeth to the rotor in the 12/14 pole machine is high at the *d*-axis position (here phase *a*) due to the high flux saturation (2.1T) in the stator tooth tops and the relatively small space between the rotor teeth. The performance of the 12/14 pole machine can be improved by optimization.

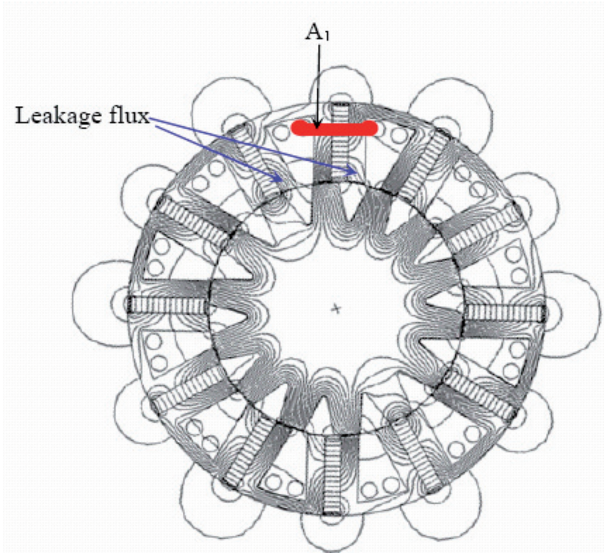

Fig. 6-24 Flux distribution in the 12/14 pole prototype machine at *d*-axis position of coil A

For simplification, in the presented optimization procedure the stator slot width, phase winding and phase current are kept unchanged, so the copper loss is the same as before the optimizations. And the total loss of each machine is assumed to keep unchanged during the optimization for calculating the output torque by FEM simulations. This is because the iron loss is relatively small at a low-speed application of 400 rpm, and during the optimization procedure the parameter variations that influence the iron loss, which are B_t, W_{st} and W_{rt}, are also relatively small.

The flux leakage can firstly be reduced by lessening the magnet thickness to decrease the flux saturation in the stator teeth. On the other hand, the total magnetic flux produced by the magnets also decreases along with a reduction of the magnet thickness. So there is an optimal magnet thickness providing the highest output torque. Fig. 6-25 shows the output torques with respect to different magnet thicknesses by FEM simulations. Their average torques and peak to peak torque ripples have also been presented in Fig. 6-26. It is shown that with 7 mm magnet thickness the machine provides the highest average output torque of 35.3 Nm, whilst with 6 mm magnet thickness the machine has the lowest torque ripple of 2.4%.

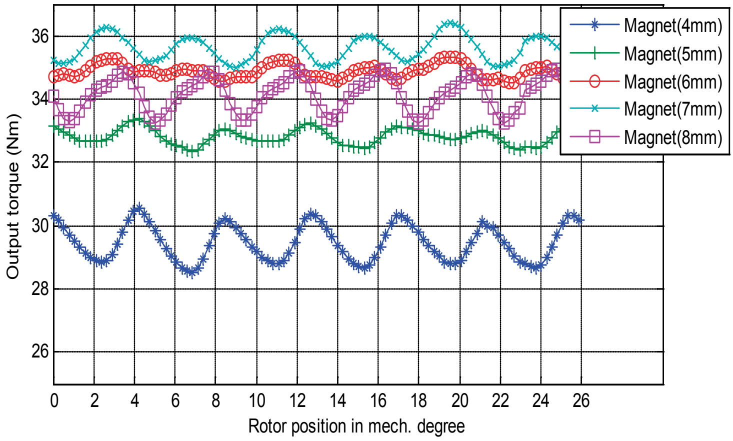

Fig. 6-25 Output torque with different magnet widths

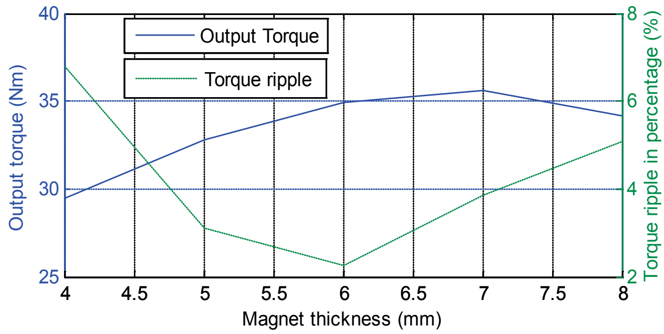

Fig. 6-26 Average torque and torque ripple in Fig. 6-25

Reducing the rotor tooth width to increase the space between rotor teeth can further reduce the flux leakage. Meanwhile the flux saturation in the rotor teeth will increase along with a decrease of the rotor tooth width. So there is an optimal rotor tooth width providing the highest output torque. The output torques from FEM simulations with respect to rotor tooth width are illustrated in Fig. 6-27 while the magnet thickness is fixed to 7 mm. Their average torques and torque ripples are provided in Fig. 6-28. It is observed that with 11 mm rotor tooth width the machine has both a high output torque of 38.3 Nm and a small torque ripple of 2.3%. Compared to the 10/12 pole machine, the output torque is ~23.5% higher and the torque ripple is also further reduced.

The optimized machine efficiency can be approximated by (6.16) and is around 87%.

$$\eta = T_{out}\omega_m / \left(T_{out}\omega_m + P_{cu} + P_{Fe}\right) \tag{6.16}$$

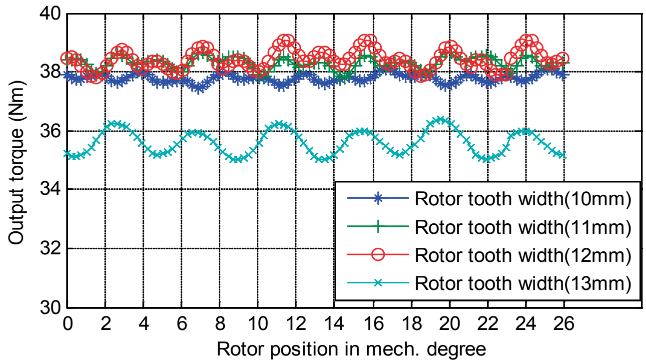

Fig. 6-27 Output torque with different rotor widths (fixed 7 mm magnet thickness)

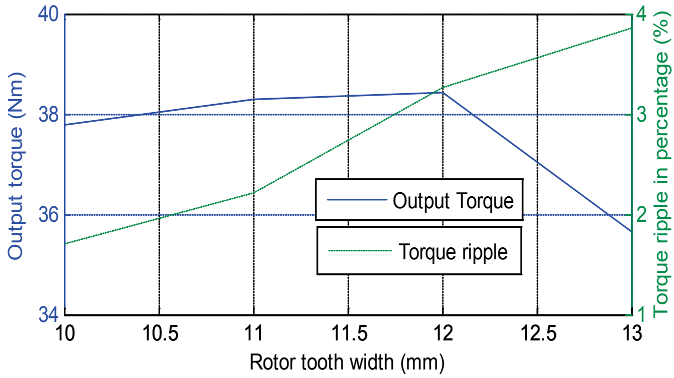

Fig. 6-28 Average torque and torque ripple in Fig. 6-27

6.7 Conclusion

Both 12/10 and 12/14 pole FSPM machines have been investigated by FEM analysis and experimental measurements. Compared to the 12/10 pole machine, the results show that the 12/14 pole machine has the following characteristics:

1. It has a sinusoidal EMF waveform like the 12/10 pole machine.
2. With the same copper loss, the 12/14 pole machine can provide higher output torque. Both the FEM simulations and the experimental measurements show the original 12/14 pole machine prototype can provide 11% higher torque than the optimized 12/10 pole machine. FEM simulations show that the optimized 12/14 pole machine could provide ~23.5% higher torque.
3. Less toque ripple is achieved. The 12/14 pole prototype has a torque ripple of 5.1% less than that of the 12/10 pole machine, 8.5%. The FEM analysis shows the torque ripple can be further reduced to 2.3% after optimization.

4. Higher efficiency is expected for low speed applications where the copper loss is the dominant loss in machines.
5. Higher inductance than the 12/10 pole machine with the same stator and winding design.

7. Preliminary Design of a 12/14 pole FSPM machine

In the previous chapter the 12/14 FSPM machine has been investigated. Compared with a 12/10 pole machine, this machine can provide higher torque density with less torque ripple. Currently FSPM machines are generally designed as an initial machine, in which $H_{sb} = l_{pm} = W_{rt} = W_s = W_{st} = \tau_s /4$ as shown in Fig. 6-3 and Fig. 6-4. Thereafter, the optimal parameters and /or performance were studied by either finite element method (FEM) simulations or lumped parameter magnetic circuit model [56]. Such initially designed FSPM machines usually have highly saturated stator iron teeth, which is normally beneficial for a 12/10 pole machine to improve the output torque. But for a 12/14 pole machine, the high saturation will lead to a torque reduction due to the increased flux leakage between the stator and rotor. So a new approach is required to design a high-torque 12/14 pole machine. This chapter newly introduces a simplified lumped parameter magnetic circuit model to analytically design the machine, which has been presented in [5]. Firstly the machine design parameters are studied addressing on high output torque. Then the flux distribution of a typical 12/14 FSPM machine is investigated by FEM simulations, based on which a lumped parameter magnetic circuit model is built up for finding optimal design parameters. Finally, the analytically designed machine is verified by FEM simulations.

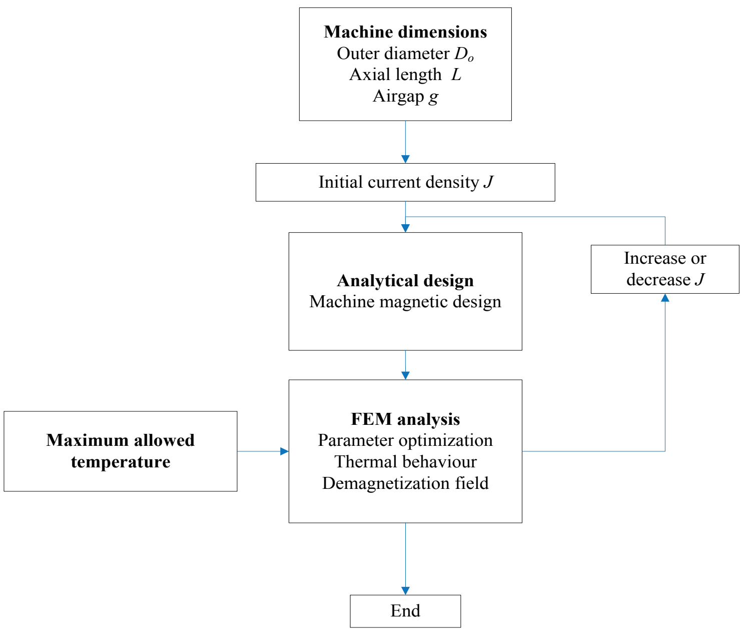

Fig. 7-1 Machine design process

Fig. 7-1 provides the general design process of the machine. This chapter is only focused on the analytical design part with a fixed current density. The current density is dependent on the maximum allowed internal temperature and the demagnetization field, which will be discussed in the FEM analysis part and presented in next chapter.

7.1 Machine magnetic design

As presented in the previous chapter, the coil-flux linkage of each phase in a 12/14 pole machine is essentially sinusoidal with respect to the rotor position. It reaches the peak value when the rotor is at the *d*-axis position as shown Fig. 7-2, and at this position the flux in the four coils of the phase is the same as shown in Fig. 7-4.

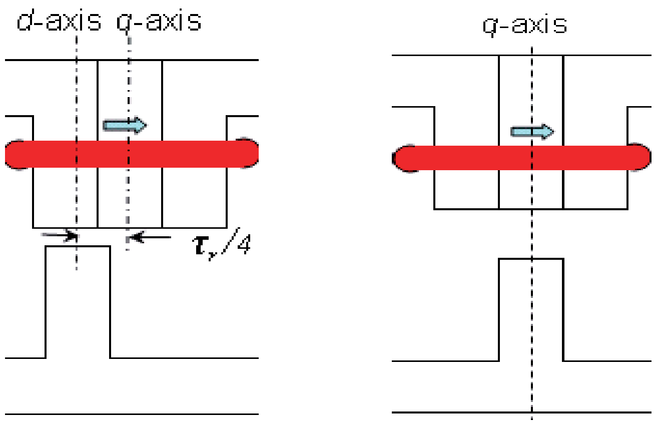

(a) (b)

Fig. 7-2 Rotor at (a) *d*- axis (b) *q*-axis positions

When neglecting machine losses, the torque equation (6.15) can be re-written as

$$T = \frac{\sqrt{2}\pi^2}{4p_s} k_\sigma P_r B_t \lambda^2 D_o^2 L S c_s \,. \tag{7.1}$$

where c_s is the ratio of the stator tooth width to the stator pole pitch, and k_σ is the leakage factor representing the effective flux at the *d*-axis position and can be evaluated here by

$$k_\sigma = \frac{\Phi_{p3} - \Phi_{p4}}{\Phi_{p3}} \,. \tag{7.2}$$

where Φ_{p3} and Φ_{p4} are respective the flux through the teeth *P3* and *P4* shown in Fig. 7-4 and Fig. 7-5.

7.1.1 Design parameters

The stator outer diameter D_o and axial length L are generally constrained by the available volume of a specific case and are therefore fixed.

B_t is an important design parameter. Ideally without considering iron saturation, higher B_t would produce higher torque according to (7.1). In reality, along with an increase of B_t the value of k_σ will decrease because of the increased iron saturation as shown in Fig. 7-3. This has been presented in the previous chapter. It is observed that the product reaches its peak value when B_t is 1.8 ~1.9 T. Here B_t is chosen to be 1.8 T, which is typically the saturation flux density of iron materials.

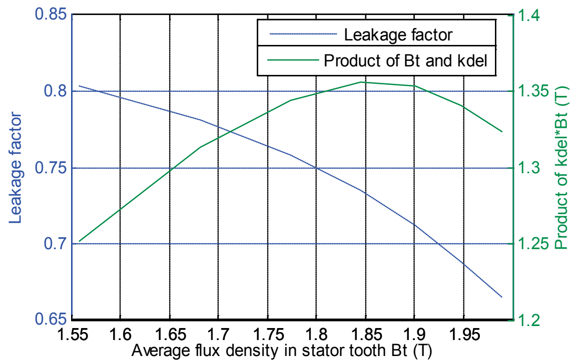

Fig. 7-3 Leakage factor k_σ and the product of k_σ and B_t at different B_t

If λ and c_s are selected as design variables here, then the other machine parameters can be expressed in terms of them as follows:

The tooth width is calculated as

$$W_{st} = \tau_s c_s . \tag{7.3}$$

where τ_s is the stator pole pitch and calculated by

$$\tau_s = \frac{\pi D_o \lambda}{P_s} . \tag{7.4}$$

The magnet width is determined by

$$W_{pm} = \frac{(1-\lambda) D_o}{2} . \tag{7.5}$$

The stator iron-back thickness H_{sb} is chosen in such a way that the maximum flux density in the stator iron back is the same as B_t. In this way, the iron does not get saturated and the copper can have the maximum available area. FEM simulations show that the stator back iron thickness should be around 70% of the stator tooth width to avoid saturation. The value is the same as that presented in [56]. The rotor iron-back thickness H_{rb} is chosen to be the same as H_{sb}.

The height of the rotor tooth H_{rt} determines the rotor saliency. Generally the reluctance torque of the machine is negligible. However, the output torque can be slightly increased with higher H_{rt}. The research based on a 12/10 pole machine shows the maximum torque is obtained when the rotor tooth height is around twice the stator tooth width [56]. Further increasing the radial height reduces the torque, due to the increase in the magnetic potential drop in the rotor tooth body because of magnetic saturation and an increase in flux leakage. This conclusion is employed for this machine design because of the similar construction of the two machines and the negligible reluctance torque value.

$$H_{rt} = 2W_{st} \tag{7.6}$$

The magnet thickness l_{pm} may be started with a small initial value, for example, 1 mm here, so that B_t is less than 1.8 T. Its final value will be found out later in the subsection of *design procedure*. Then the electrical loading S is determined by the available copper area from (4.36), in which A_{cu} is the copper area in the stator and calculated by

$$A_{cu} = \pi\left(\frac{D_o}{2} - H_{sb}\right)^2 - \pi\left(\frac{\lambda D_o}{2}\right)^2 - P_s H_t\left(2W_{st} + l_{pm}\right). \tag{7.7}$$

where H_t is the stator tooth height and given by

$$H_t = \frac{(1-\lambda)}{2} D_o - H_{sb}\,. \tag{7.8}$$

The rotor tooth width W_{rt}, unlike the stator parameters, can be freely chosen without influencing other design parameters. Although W_{rt} does not directly appear in torque equation (7.1), it affects the air-gap reluctances, further the leakage factor k_σ and the output torque. The principle for selecting W_{rt} is to make k_σ value as big as possible. For a 12/14 machine with $l_{pm} = W_{st} = \tau_s /4$, the optimal W_{rt} is found to be $\tau_r /3$ [117]. In the discussed case both l_{pm} and W_{st} are varied with different λ and c_s, the rotor tooth width here is chosen so that the left edge of the rotor tooth at the *d*-axis aligns with the left edge of the stator tooth as *T2* and *P3* shown in Fig. 7-5. In this way, the maximum overlapped area between the stator and rotor teeth is obtained for the chosen W_{st} and W_{rt} at the d-axis. Then the rotor teeth width is determined by (7.9). If necessary, the rotor tooth width can be optimized afterwards by FEM analysis.

$$W_{rt} = 2W_{st} + l_{pm} - \frac{\tau_r}{2} \tag{7.9}$$

where

$$\tau_r = \frac{(\lambda D_o - 2g)\pi}{P_r} \tag{7.10}$$

7.1.2 Flux distribution and lumped parameter model

So far all the machine parameters in (7.1) are known except k_σ. Since B_t and k_σ are calculated at d-axis position, it is of interest to investigate the flux distribution at that position. Fig. 7-4 shows the flux distribution of a typical 12/14 pole machine at the d-axis (phase a here). The four coils of phase a have the same flux linkage, and the flux in each coil is mainly from the three magnets near the phase coil as shown in Fig. 7-5 (a). So it is sufficient only to analyze the flux paths of these three magnets for evaluating B_t and k_σ. The flux distributions in the air gap between the stator and rotor teeth are approximated in Fig. 7-5 (b). The flux distributions in the air gap are slightly varied depending on the specific values of W_{st}, W_{rt}, and l_{pm} (see Appendix A). Fig. 7-6 shows the lumped parameter magnetic circuit model of the flux paths in Fig. 7-5 at no-load condition.

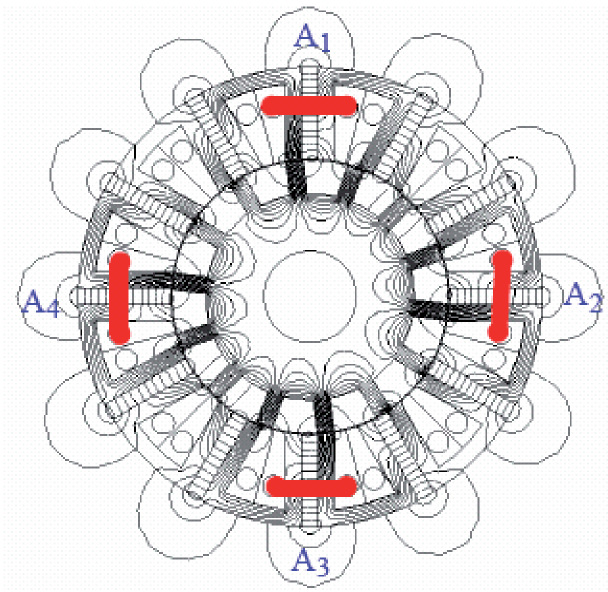

Fig. 7-4 Flux distribution at the d-axis position of phase a

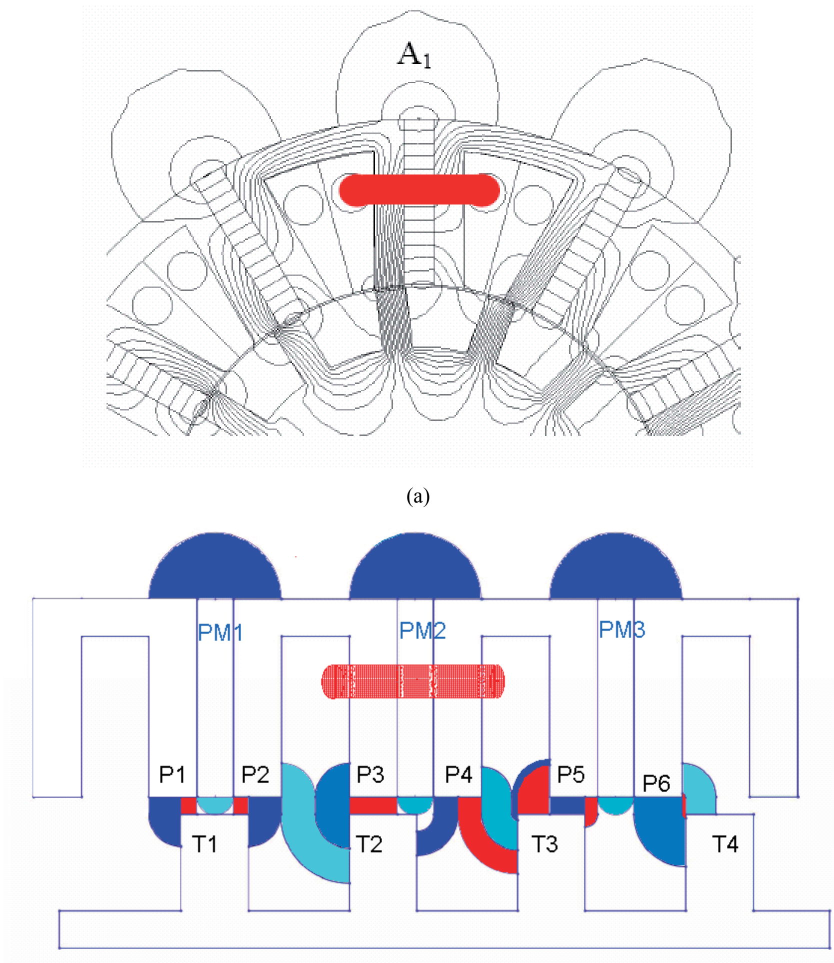

(a)

(b)

Fig. 7-5 Flux distribution in the air gap at the *d*-axis position

(a) Flux distribution from FEM simulations (b) the approximation for analytical calculations.

7.2 Lumped parameter magnetic circuit model

Based on the flux paths in Fig. 7-5, a lumped parameter magnetic circuit model of one fourth of the machine is built up at no-load condition as shown in Fig. 7-6. Compared with the model in [53] and [117] where half the machine is modeled, this model is simplified. In the presented model the end effect is not considered since the machine axial length is relatively long compared with its diameter (L/D_o=2).

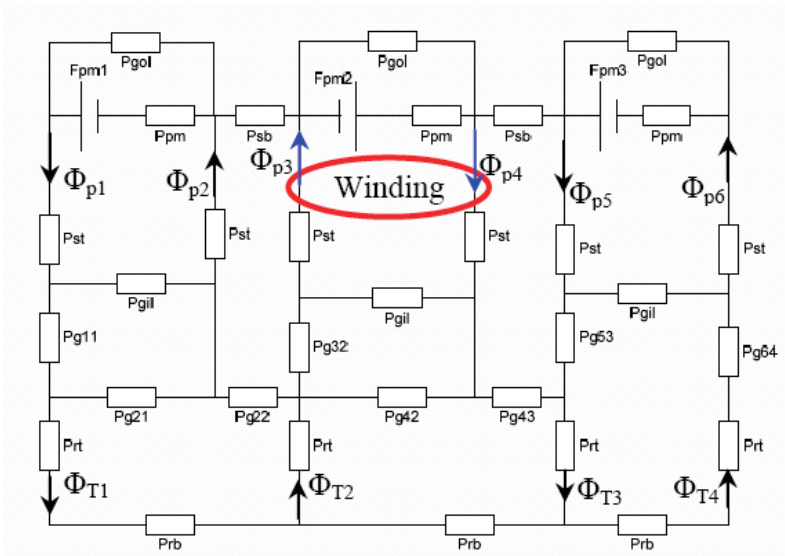

Fig. 7-6 Lumped parameter models of the flux paths in Fig. 7-5 at no load

The permanent magnets are simply modeled as a MMF by (7.11) and their permeances are calculated by (7.12) .

$$F_{pm} = l_{pm} B_a / (\mu_{pm} \mu_0) \tag{7.11}$$

where B_a is determined by (4.32).

where B_r is the magnet remanence at room temperature T_0, and k_{pm} is the magnet temperature coefficient.

$$P_{pm} = \mu_{pm} \mu_0 L W_{pm} / l_{pm} \tag{7.12}$$

The permeances of the iron parts, P_{st}, P_{rt} and P_{sb}, are determined by

$$P = \mu_r \mu_0 A / l \,. \tag{7.13}$$

where A and l are respectively the cross-sectional area and the length of the corresponding iron part, μ_r is the relatively permeability of the iron part and determined by iteration form the B-H curve of the lamination material.

To calculate the air-gap permeances P_g, P_{gil} and P_{gol} the method presented in [53] is employed here, and they are presented in Appendix A.

7.3 Approximation of Magnetization curve

An expression for the relation between the flux density and the field intensity (B-H curve) is required for calculating the magnetic reluctance of the iron. In reality, it is very difficult to find an expression that can exactly represent the curve.

Fortunately, equation (7.14) can be used to approximate the magnetization curve [120].

$$B_i(H_i) = \mu_0(H_i + M_s(\coth(\frac{H_i}{a}) - \frac{a}{H_i})) \tag{7.14}$$

where M_s is saturation magnetization, and α is a material dependent parameter, B_i and H_i are respectively the flux density and field intensity in the corresponding iron part.

By varying the values of M_s and α, the shape of the curve obtained from (7.14) can be changed. After several iterations, the curve with M_s =1.5 MA/m and α =550 shown in Fig. 7-7 can be used as an approximation of the iron magnetization curve.

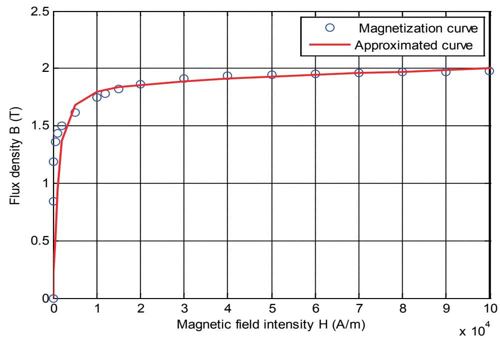

Fig. 7-7 Magnetization curve and its approximation

7.4 Magnetic circuit equations

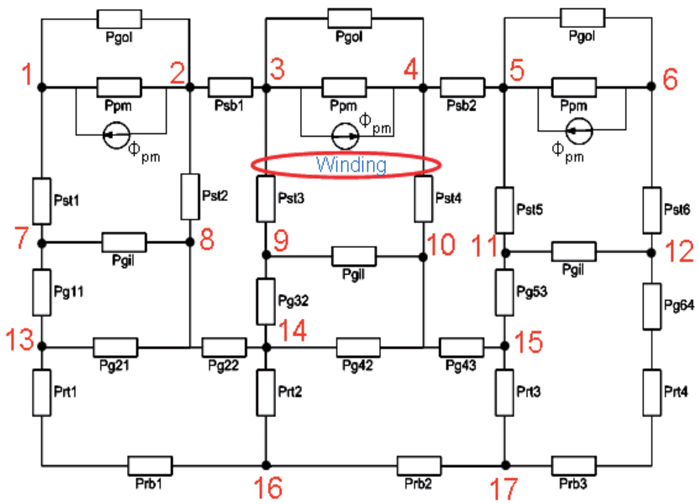

Fig. 7-8 Magnetic circuit with PMs represented by flux sources

Nodal analysis is employed to solve the magnetic circuit. Each permanent magnet is represented by a flux source and a flux resistance in parallel as shown in Fig. 7-8, in which Φ_{pm} is given by

$$\Phi_{pm} = P_{pm} F_{pm} . \qquad (7.15)$$

There are totally 17 nodes in the magnetic circuit and the equations between the relationship of the these magnetic variables are established as

$$\begin{bmatrix} \Phi_s(1) \\ \Phi_s(2) \\ . \\ . \\ . \\ \Phi_s(17) \end{bmatrix} = \begin{bmatrix} P(1,1) & P(1,2) \ldots P(1,17) \\ P(2,1) & P(2,2) \ldots P(2,17) \\ . & . \quad \ldots \quad . \\ . & . \quad \ldots \quad . \\ . & . \quad \ldots \quad . \\ P(17,1) & P(17,2) \ldots P(17,17) \end{bmatrix} \begin{bmatrix} F(1) \\ F(2) \\ . \\ . \\ . \\ F(17) \end{bmatrix} . \qquad (7.16)$$

where

$\Phi_s(1)$ - $\Phi_s(17)$ respectively represent the flux flowing into the corresponding nodes from the flux sources, here $\Phi_s(1) = \Phi_s(4) = \Phi_s(5) = \Phi_{pm}$ and $\Phi_s(2) = \Phi_s(3) = \Phi_s(6) = -\Phi_{pm}$, while the others are zero.

$P(m,n)$, $m \neq n$, is the negative permeance value between nodes m and n.

$P(m,m)$ is the sum of the permeance of those branches connected to node m.

$F(1)$- $F(17)$ are respectively the magnetic potential at nodes 1-17.

When solving (7.16), the initial permeance value of each iron part is set μ_r = 4000. Afterwards, μ_r^k for k^{th} iteration of each iron part is updated based on previous calculation as follows:

Calculating the magnetic field intensity over the corresponding iron part by

$$H_i^{k-1} = \frac{\Delta F_i^{k-1}}{l} . \qquad (7.17)$$

where ΔF_i^{k-1} is the magnetic potential drop over the corresponding iron part, whose value can be calculated from the magnetic potentials at the nodes.

Updating μ_r according to the magnetization curve in Fig. 7-7 by

$$\mu_r^k = \frac{(H_i^{k-1} + M_s(\coth(\frac{H_i^{k-1}}{a}) - \frac{a}{H_i^{k-1}}))}{H_i^{k-1}} . \qquad (7.18)$$

Repeating the procedure with the updated μ_r value until B_i^k and H_i^k fulfill (7.14). B_i^k is obtained from

$$B_i^k = \Delta F_i^k P / A . \tag{7.19}$$

It should be mentioned that the magnetic saturation over teeth T4 is underestimated since the flux from P7 is not considered. Fortunately, the saturation is negligible due to the large air-gap reluctance because of the small or even no overlapped iron area between teeth P6/P7 and T4 as shown in Fig. 7-5.

7.4.1 Design procedure

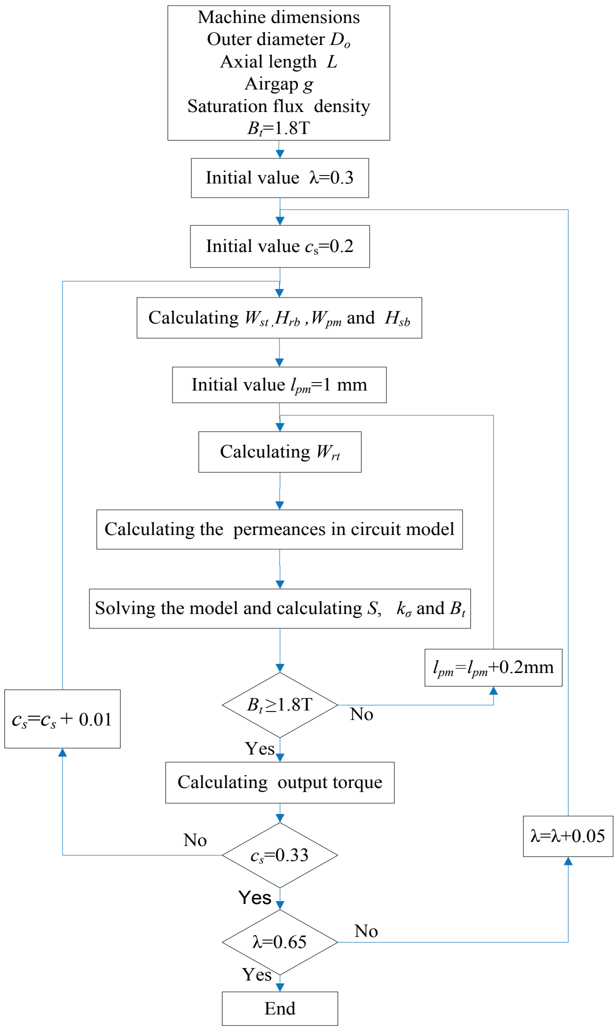

Fig. 7-9 Magnetic design process of the machine

To calculate the maximum output torque from (7.1) with certain λ and c_s, the value of k_σ should be known when B_t is 1.8 T. This is achieved by gradually increasing l_{pm} based on the given initial value, then recalculating W_{rt} from (7.9) and further all the permeances in Fig. 7-8. Thereafter, solving the model to figure out Φ_{p3} and Φ_{p4} and further k_σ and B_t. Repeating the process until B_t = 1.8 T. Now l_{pm} and k_σ are known and the output torque can be evaluated by (7.1). Fig. 7-9 presents the design procedure.

Fig. 7-10 shows the leakage factor as function of λ and c_s. For each c_s the value of k_σ increases along with an increase of λ, and for each λ there is an optimal c_s where k_σ reaches its maximum value.

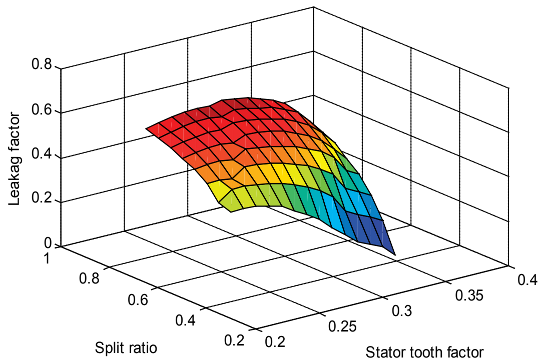

Fig. 7-10 Leakage factor k_σ as function of split ratio λ and stator tooth factor c_s

Fig. 7-11 presents the output torque as function of λ and c_s. There is an optimal λ and c_s giving the maximum output torque. Fig. 7-12 and Fig. 7-13 respectively show the maximum output torque with respect to split ratio λ and stator tooth factor c_s. It is found that the optimal λ is around 0.5 and c_s is around 0.25 for the case discussed here. Table 7-1 lists the parameters of the designed machine.

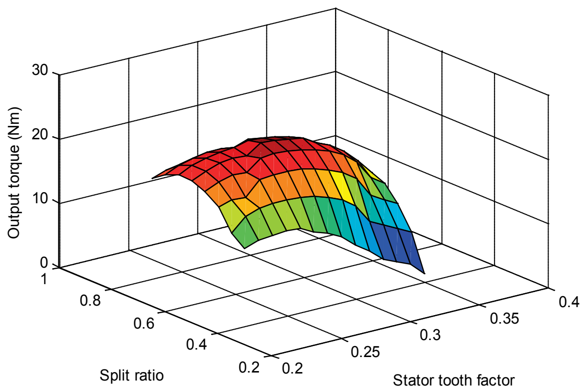

Fig. 7-11 Output torque as function of split ratio λ and stator tooth factor c_s

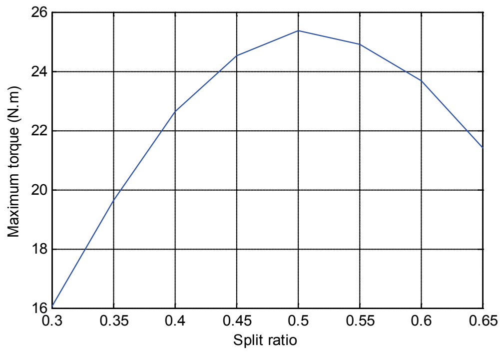

Fig. 7-12 Maximum output torque at different split ratio λ

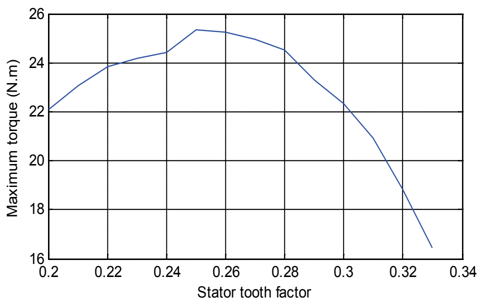

Fig. 7-13 Maximum output torque at different stator tooth factor c_s

Table 7-1: Machine parameters of preliminary design

Parameter	Value
D_o	100 mm
L	200 mm
g	0.5 mm
λ	0.5
c_s	0.25
P_s	12
P_r	14
W_{rt}	3.4 mm
W_{st}	3.2 mm
H_{sb}	2.2 mm
H_t	23 mm
H_{rt}	6.4 mm
l_{pm}	2.4 mm
B_r	1.16 T
k_f	0.6
J	4 A/mm^2
T_θ	150º
k_{pm}	-0.00045 K^{-1}

7.5 FEM verification

In order to verify the analytical results and also to optimize the rotor tooth width, 2D FEM simulations are performed in this section. Firstly the designed machine is studied by the FEM simulations and the results are compared with those from the analytical ones. The torque capability of the machines with varied W_{st} and W_{rt} are also investigated afterwards.

7.5.1 Simulation of the designed machine

The machine with the parameters given in Table 7-1 is investigated by FEM simulations, in which the *B-H* curve in Fig. 7-7 is employed for the iron material and B_a determined by (4.32) is set to 1.09 T to take the temperature influence into account. Fig. 7-14 shows the flux distribution of the machine at the *d*-axis position with no load (J = 0), from which B_t and k_σ are obtained. Fig. 7-14 presents the output torque from the simulation. And Table 7-2 lists the results from both the lumped parameter magnetic circuit model and the FEM simulations. The torque calculated from the circuit model is about 3.3% higher than that from the FEM simulations.

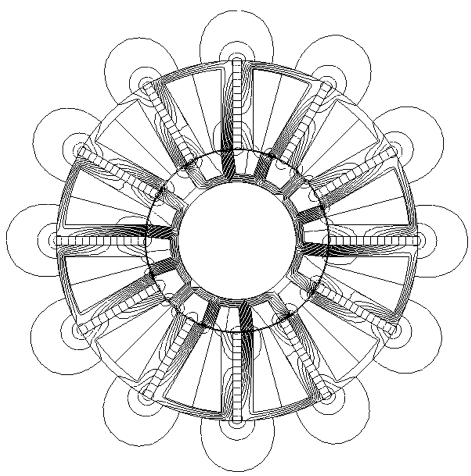

Fig. 7-14 Flux distribution of the designed machine at no load

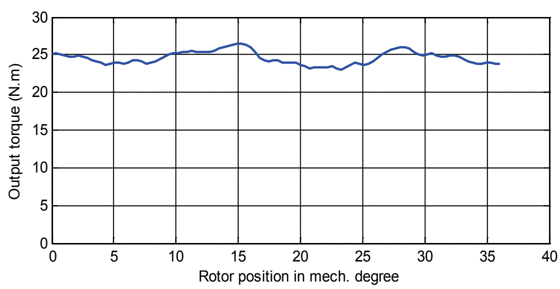

Fig. 7-15 The output torque from FEM simulations

Table 7-2: Flux density B_t, Leakage factor k_σ and torque for preliminary design

	Analytical	FEM
B_t (T) (no load)	1.8	1.8
k_σ (no load)	0.67	0.69
T (Nm)	25.4	24.6 (average)

7.5.2 Machines with varied W_{st} and W_{rt}

The torque capability of the machines with varied W_{st} and W_{rt} are studied base on the following conditions:

1. Keeping W_s, J, g and λ unchanged.

2. Keeping the relation of $H_{sb}= H_{rb}= 0.7\ W_{st}$.

3. W_{st} varied from 3.0 to 3.6 mm. As a consequence, l_{pm} decreases along with an increase of W_{st}.

4. For each W_{st}, W_{rt} varied from 3.2 to 3.8 mm.

Fig. 7-16 shows the output torque as function of stator and rotor tooth width. The maximum torque, 25.2 Nm, is obtained when W_{st} = 3.2 mm and W_{rt} = 3.6 mm. Compared with the analytical designed machine, the stator tooth width is the same and the rotor tooth width is slightly (5.9 %) wider and the torque is only 2.4% higher. So the presented simplified magnetic parameter circuit model can be used to preliminarily design the high torque machine.

It is observed from the figure that the optimal W_{st} for maximum torque is almost independent of W_{rt} in the case discussed here. So the selection of W_{rt} does not significantly affect the selection of the stator parameters, but it does influence the maximum torque value.

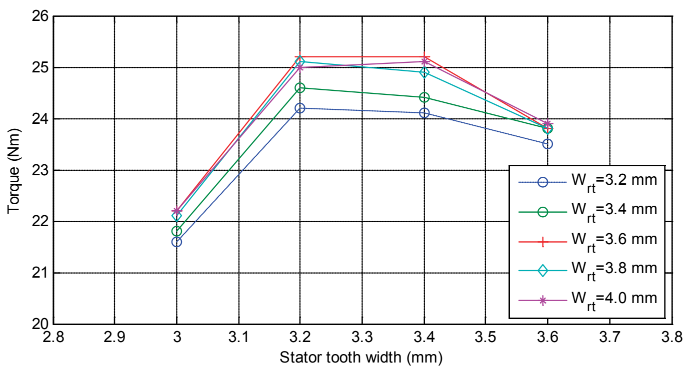

Fig. 7-16 Output torque as function of stator and rotor tooth width

k_σ and B_t are also investigated at no load condition and presented in Fig. 7-17 and Fig. 7-18, respectively. Along with an increase of W_{st}, the value of B_t decreases in

Fig. 7-18 due to the shorter l_{pm}, consequently, k_σ increases as shown in Fig. 7-17. In the presented case, B_t is mainly determined by W_{st}, but slightly influenced by W_{rt}. B_t increases when W_{rt} increases. But k_σ is going to decrease for a wide W_{rt}, for example, W_{rt} =4.0 mm here. The maximum torque is obtained when B_t is around 1.8 T, which is the same value as that employed in the analytical design procedure.

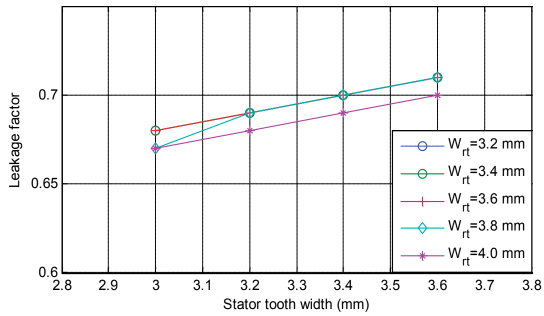

Fig. 7-17 k_σ as function of stator and rotor tooth width

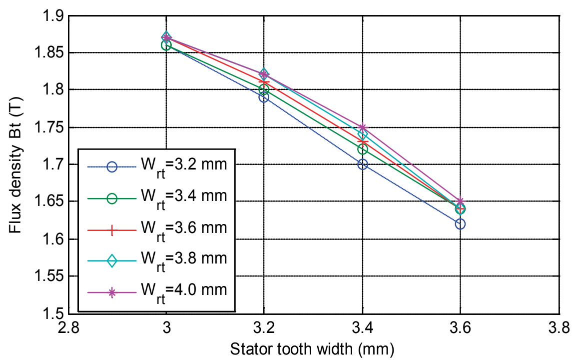

Fig. 7-18 B_t as function of stator and rotor tooth width

7.6 Conclusion

This chapter has newly introduced a simplified lumped parameter magnetic circuit model for analytically designing a high-torque 12/14 pole FSPM machine. And the design procedure of how to find out the optimal design parameters is also presented. The designed machine has been verified by FEM simulations.

8. Performance study of the machine by FEM simulations

In the previous chapter the magnetic design of a 12/14 pole machine has been has presented. This chapter will investigate the performance of the machine in downhole applications where the ambient temperature is assumed to be 150°C and no external forced cooling is available. The maximum temperature in the machine should not be over 200°C, limited by both the PM material and winding insulation. Firstly, the number of turn and machine inductance are studied. Later, the output torque, machine losses, power factor and efficiency are investigated based on finite element method (FEM). Additionally, the magnet demagnetization field and machine thermal phenomenon are also presented. Most of the results in this chapter have been published in [6].

8.1 Inductance and number of turns

The accuracy of calculating the steady-state performance of permanent magnet machines depends on the accuracy of calculating the synchronous reactance in the *d*- and *q*-axis. In [99]-[101] different analytical approaches and FEM analysis have been introduced. For the discussed machine it is not easy to analytically calculate the reactance due to the complexity of the flux paths and leakage in the air gap. Additionally, the reactances are sensitive to the iron saturation. Here FEM analysis is employed.

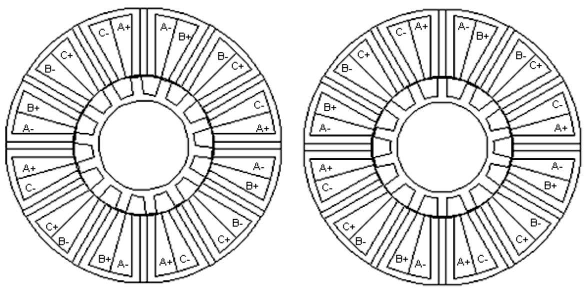

(a) (b)

Fig. 8-1 (a) *d*-axis position (b) *q*-axis position of phase *a*

Considering the position where the rotor is aligned with the *d*- or *q*- axis of phase *a* as shown in Fig. 8-1 and the injected three-phase currents are

$$\begin{cases} i_a = I_{\max}\cos(P_r\omega t) = \dfrac{\sqrt{2}A_{coil}k_f J}{n_{coil}}\cos(P_r\omega t) \\ i_b = i_c = -\dfrac{1}{2}I_{\max}\cos(P_r\omega t) = -\dfrac{\sqrt{2}A_{coil}k_f J}{2n_{coil}}\cos(P_r\omega t) \end{cases} . \quad (8.1)$$

where A_{coil} is half the slot area, n_{coil} is the number of turns of each coil, it is one fourth the phase-coil turns, n_s.
Then L_d and L_q of each phase can be calculated by [100]

$$L_d = \left.\frac{\psi_{d-\max} - \psi_{pm}}{I_{\max}}\right|_{d-axis} = n_{coil}^2 \left.\left(\frac{\left(\Phi_{d-\max} - \Phi_{pm}\right)}{\sqrt{2} A_{coil} k_f J}\right)\right|_{d-axis}$$

or

$$L_q = \left.\frac{\psi_{q-\max}}{I_{\max}}\right|_{q-axis} = n_{coil}^2 \left.\left(\frac{\Phi_{q-\max}}{\sqrt{2} A_{coil} k_f J}\right)\right|_{q-axis} \tag{8.2}$$

where $\Phi_{d\text{-}max}$ and $\Phi_{q\text{-}max}$ are respectively the maximum summary flux in four phase-*a* coils at *d*- and *q*-axis positions. $\psi_{d\text{-}max}$ and $\psi_{q\text{-}max}$, are separately the peak flux-linkage at *d*- and *q*-axis, ψ_{pm} and Φ_{pm} are individually the flux linkage and flux produced by PM alone.

As can be seen from (8.2), the inductances are proportional to the square of the turn numbers. If assuming the machine has one-turn coil, its one-turn inductance $L_{1\text{-}d/q}$ is directly given by (8.2) with $\Phi_{d\text{-}max}$, $\Phi_{q\text{-}max}$ and Φ_{pm} obtained from FEM simulations as shown in Fig. 8-2, and Φ_{pm} = 3.22 mWb. Then the inductance with n_{coil} turns is:

$$L_{d/q} = n_{coil}^2 L_{1-d/q} \tag{8.3}$$

where $L_{1\text{-}d/q}$ is the phase inductance with one-turn coil in the *d* or *q*-axis, and they are respectively $L_{1\text{-}d}$=4.27 uH and $L_{1\text{-}q}$=5.27 uH from the FEM simulations.

It is observed from Fig. 8-2 that due to the iron saturation the peak flux at the *d*-position is not symmetrical at the positive and negative current, so the average between them is employed.

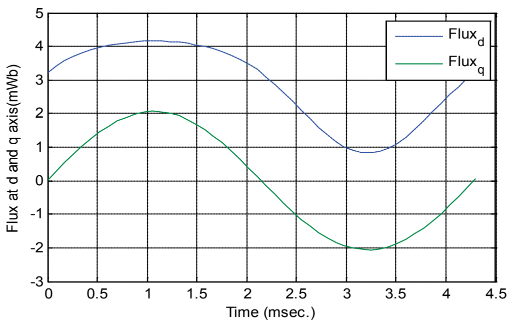

Fig. 8-2 Flux at *d* and *q* axis from FEM simulations

The number of phase-coil turns is limited by the voltage limitation $V_{\max}$ of the converter used for control. A typical equivalent circuit of one phase in electrical machines is shown in Fig. 8-3.

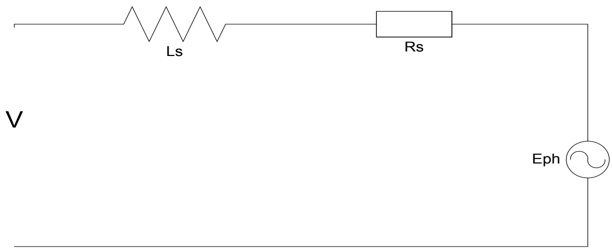

Fig. 8-3 Equivalent circuit of one phase of an electrical motor

$$V = E_{ph} + I_{ph}(jX_s + R_s) \le V_{\max} \tag{8.4}$$

where E_{ph} is the phase back EMF (*rms* value) proportional to n_{coil}, the phase EMF with one-turn coil, $E_{1\text{-}turn}$, is obtained by FEM simulations shown in Fig. 8-4 and its *rms* value is 3.5 V. R_s is the copper resistance and evaluated from (8.5), X_s is the phase reactance and calculated by (8.7). I_{ph} is the phase current (*rms*) determined by (8.8).

$$R_s = \frac{8n_{coil}\rho_{cu}L_{cu}}{(A_{coil}k_f / n_{coil})} = \frac{8n_{coil}^2\rho_{cu}(L + l_{end})}{A_{coil}k_f} \tag{8.5}$$

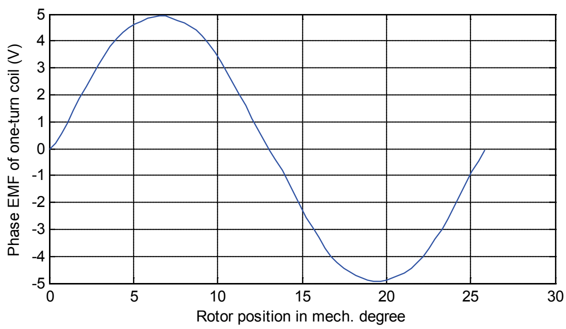

Fig. 8-4 Phase back EMF with one-turn coil

where l_{end} is approximated by

$$l_{end} = \pi^2(\lambda D_o + H_t)/2p_s \tag{8.6}$$

$$X_s = P_r\omega_m L_s \tag{8.7}$$

Assuming the FSPM machine is controlled to only have q-axis current I_q (I_d=0), and it is determined by

$$I_q = I_{ph} = \frac{A_{coil} k_f J}{n_{coil}} \tag{8.8}$$

Substituting (8.5), (8.7) and (8.8) into (8.4) yields

$$\begin{aligned} V_{\max} &\geq E_{ph} + I_q (jP_r \omega_m L_q + R_s) \\ &\geq E_{1-turn} n_{coil} + 8n_{coil} J \rho_{cu} L_{cu} + jP_r \omega_m A_{coil} k_f J n_{coil} L_{1-q} \end{aligned} . \tag{8.9}$$

The turn number of each coil is limited by

$$n_{coil} \leq \sqrt{\frac{V_{\max}^2}{(E_{1-turn} + 8J\rho_{cu} L_{cu})^2 + \left(P_r \omega_m A_{coil} k_f J L_{1-q}\right)^2}} . \tag{8.10}$$

Here $V_{\max}$ = 415V and n_{coil} is selected to be 96.

Then the cross-sectional area of the conductor is calculated by (8.11) and it is around 0.72 mm^2.

$$A_{con} = \frac{A_{cu} k_f}{24 n_{coil}} \tag{8.11}$$

8.2 Losses and machine efficiency

In order to investigate the machine efficiency and the thermal behavior, the machine losses that contribute to heating are studied. The losses considered here are the iron loss in stator and rotor, the copper loss in the stator winding including the end parts, (only the ohmic losses are considered, eddy current loss in the copper is neglected) and the magnet eddy current loss.

8.2.1 Iron losses

The iron loss significantly depends on the iron material. Fig. 8-5 depicts the specific losses of M330-35A. The loss is frequency dependent and the curve in the considered case is the one at 233 *Hz* ($P_r\omega_m$). Then the iron loss in each part is determined by

$$P_{fe} = WG . \tag{8.12}$$

where W is the specific loss in the corresponding iron part dependent on the peak flux density that can be obtained by FEM simulations, and G is the weight of the corresponding iron part. For calculating the loss in the teeth where the peak density at the top and bottom may be different, its average peak value is employed.

The weight of the stator back iron part G_{sb} is figured out as

$$G_{sb} = \rho_{fe} L \left(\pi (D_o - H_{sb}) - P_s l_{pm} \right) H_{sb} \,. \tag{8.13}$$

The weight of the stator teeth is expressed as

$$G_{st} = 2 P_s H_t W_{st} \rho_{fe} L \,. \tag{8.14}$$

The weight of the rotor teeth part is evaluated as

$$G_{rt} = P_r H_{rt} W_{rt} \rho_{fe} L \,. \tag{8.15}$$

The weight of the rotor back iron is

$$G_{rb} = \rho_{fe} L \pi \left((1-\lambda) D_o - 2g - 2H_{rt} - H_{rb} \right) H_{rb} \,. \tag{8.16}$$

Table 8-1 lists the peak flux densities and the calculated loss.

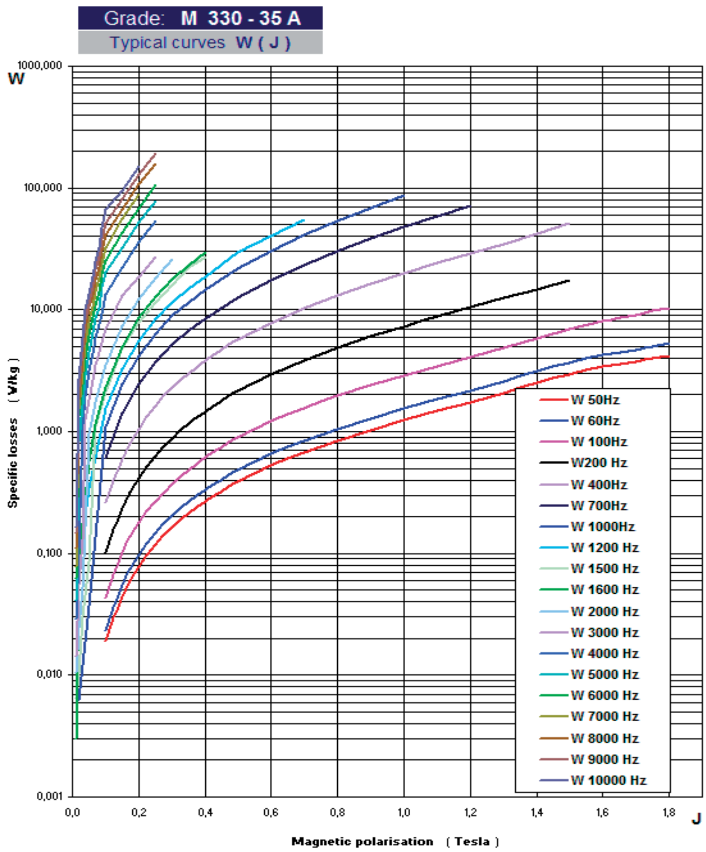

Fig. 8-5 Characteristics curve of M330-35A [82]

Table 8-1 Peak flux density in iron parts with $J = 4$ A/mm^2

Iron parts	Weight (kg)	Peak flux density (T)	Specific loss (W/kg)	Loss (W)
Stator tooth top /bottom	2.70	1.9 /1.3	28	75
Stator back iron	0.99	1.7	35	35
Rotor tooth top /bottom	0.54	1.7/1.7	35	19
Rotor back iron	0.37	1.6	28	11

8.3 Copper loss

The copper loss is calculated at 200 °C and it is determined by (8.17). The calculated loss P_{cu} is 185 W.

$$P_{cu} = I_{ph}^2 R_{s\_200} \tag{8.17}$$

where $R_{s\text{-}200}$ is the copper resistance at $T_\theta = 200$°C and given by

$$R_{s\_200} = R_s\left(1+(T_\theta - 20)\alpha_{cu}\right). \tag{8.18}$$

8.4 Magnet eddy current loss

In analysis and design of PM machines, the eddy-current effect in the permanent magnet is usually neglected. This assumption is acceptable for ferrite magnets because their conductivity is very low or for low-speed applications. Rare-earth magnets exhibit much higher conductivity and the magnet properties are more sensitive to temperature variation than other magnets. The eddy-current loss in the machines with such magnets can be comparable to the iron losses in some applications [83][84], particularly for machines with concentrated winding, the eddy current loss is much larger than that in distributed winding motor due to the wider slot opening [89].

The eddy current loss is caused by the flux variation in the magnets. In FSPM machines the eddy-current loss variation caused by the current is negligible [87]. So the loss at no load condition is investigated. This is done by FEM simulations in COMSOL as follows:

1. Setting the current density J=0 (no load) and the PM conductivity $\sigma = 7.1\times10^5$ S/m.
2. Setting the machine speed ω_m = 1000 rpm, then the rotor position is time dependent.
3. Running the simulation with *the solver of time dependent* to calculate the resistive heating density in W/m^3 in the PMs at different positions as the example shown in Fig. 8-6.
4. Integrating the resistive heating density over the PM volumes to get the total loss.

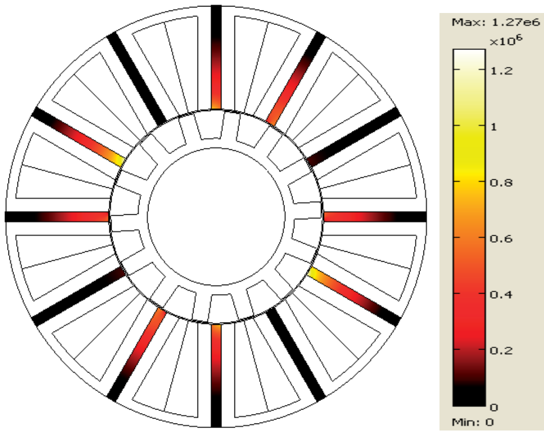

Fig. 8-6 The resistive heating density [W/m^3] in the PMs when t=0.006s

The total magnet eddy current loss at different rotor positions is presented in Fig. 8-7. Its average value P_{pm} is 26 W.

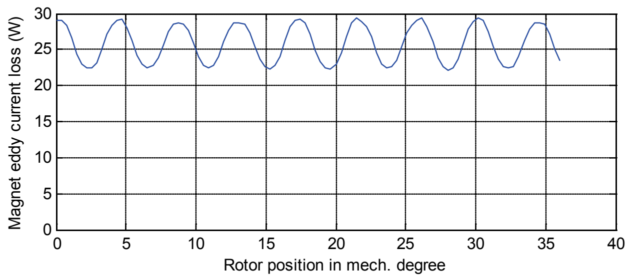

Fig. 8-7 Eddy-current loss from FEM simulations

8.5 Machine Efficiency and power factor

The machine efficiency is evaluated by (8.19).

$$\eta = \left(3E_{ph}I_{ph} - P_{fe} - P_{cu} - P_{pm}\right) / \left(3E_{ph}I_{ph}\right) \tag{8.19}$$

The power factor is determined by

$$PF = \left(E_{ph} + I_{ph}R_{s\_200}\right) / V \; . \tag{8.20}$$

8.6 Output torque and torque density

The output toque is obtained from FEM simulations and shown in Fig. 8-8, in which the magnet temperature coefficient has been taken into account using (8.21) with $T_\theta = 200$ °C. The average torque is 25.2 Nm.

$$B_m = B_r\left(1 + (T_\theta - 20)k_{pm}\right) \tag{8.21}$$

where B_m is magnet flux density used in the FEM simulations.

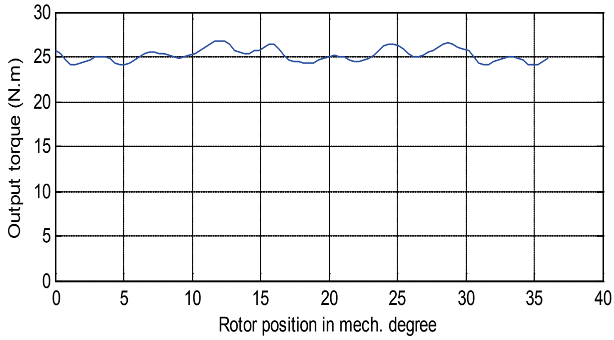

Fig. 8-8 The output toque from FEM simulations

The torque density is calculated by (4.23).

8.7 *Machine performance*

Table 8-2 presents the machine performance parameters from the investigations.

Table 8-2 Machine performance parameters

Parameter	Value
V	412 V
E_{ph}	336 V
I_{ph}	2.88 A
n_s	384 turns
L_d	39.4 mH
L_q	48.6 mH
R_s	4.4 Ω
P_{out}	2.7 kW
T	25.2 Nm
ξ_T	14.6 kNm/m^3
η	87.9%
PF	0.87

8.8 *Thermal investigation*

Insulation is the weakest part of a machine and hence can be easily destroyed by overheating, which depends on the maximum winding temperature in the machine. For this machine, the chosen insulation temperature class of the winding is 200°C (IEC317-13), its continuous work temperature is 200°C, and maximum allowable hot-spot temperature is 320°C [102].

For FEM simulations, it is quite laborious to draw all the separate conductors in the geometry. In order to simplify the slot presentation, the mixed copper conductor method presented in [121] is used. In this method all the materials in each slot except the main insulation, such as the copper conductors, the varnish in the slot and the turn insulations, are lumped together into a single equivalent material. The thermal conductivity for this material (needed for thermal simulations) is empirically determined and is between 2 and 5 times the thermal conductivity of air.

Table 8-3 The thermal conductivities for materials

Materials	Steel	Copper	Air	Aluminum	Magnet	Varnish	Equivalent material
Thermal conductivity (W/m/K)	44.5	400	0.03	201	9	0.4	0.1

The machine is installed within an aluminum frame with 1 cm thickness. Since this frame is not an active part of the machine and has no contribution for torque production, this part is therefore not considered during the machine design procedure.

For downhole applications the machine outer surface is surrounded by liquid and the temperature is assumed to be constant, for example, 150°C here. Fig. 8-9 shows the temperature distribution of the machine from the static-state FEM simulation with the calculated losses. The maximum temperature in the coil parts is around 200°C.

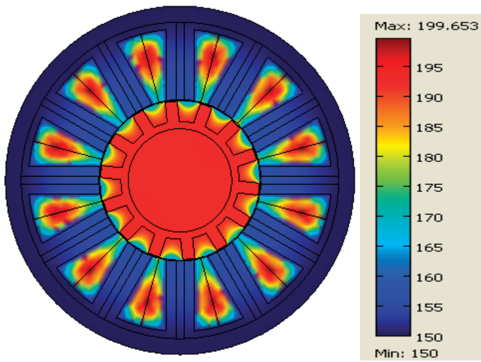

Fig. 8-9 Temperature distribution in the machine from FEM simulation

8.9 Demagnetization field

The torque capability of a PM machine is not only dependent on the cooling of the machine and the current capability of the inverter. Its torque capability is also dependent on the strength of the demagnetization field that the magnets can withstand. In the last section, the machine was designed without considering the demagnetization of the magnets and the phase current was only determined by the available copper area in the stator according to (4.36). In any PM machine, there is a risk of demagnetization of the magnets due to the high currents that produce a reverse field. A typical demagnetization characteristic for *Ne-Fe-B* and *Sm-Co* magnet materials is shown in Fig. 8-10. This characteristic is essentially linear with a slope $\mu_{pm}\mu_0$ from its residual flux density B_r to a flux density B_D. In this linear region, the recoil line coincides very closely with the demagnetization line. As long as the demagnetizing field intensity does not exceed the magnitude H_D, the recoil line will fall along the original demagnetization line and the torque capability of the machine will be preserved. So the phase current in the stator must be constrained so that no part of the magnet has its flux density reduced beyond the value B_D.

The critical point (B_D, H_D) on the demagnetization curve is temperature dependent. For *Ne-Fe-B* magnet material, B_D is around 0.05 T at 150 °C, and for *Sm-Co* magnet material, it is normally lower than 0 at 200 °C.

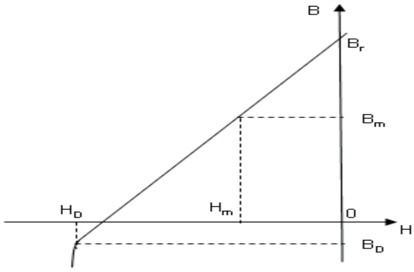

Fig. 8-10 Demagnetization characteristic of PM material

According to [70]-[72], to prevent demagnetization of the magnet the stator current must be limited so that

$$B_D < B_m - B_c\,. \tag{8.22}$$

where B_m is flux density over the magnet at no load condition, in which the stator current is zero, and B_c is the peak flux density over the magnet with stator current acting alone. Both the values can be investigated by FEM simulations.

8.9.1 B_m at no load condition

B_m is rotor position dependent value as shown in Fig. 8-11 and Fig. 8-12 when θ is respectively at 0, 6.5 and 13 mechanical degrees. When considering the demagnetization, only the *x* component of the flux that is against the magnetization direction of the magnets is considered. In order to know the flux density distribution over the whole magnets, the *x* component of the flux density along three different lines in the radial directions, which are marked as Line 1 (left edge of the magnet), Line 2 (middle line of the magnet) and Line 3 (right edge of the magnet), are investigated and presented in Fig. 8-12, in which "Y" at the x-axis in the figures are the distance from the machine center point to the point where the flux density is given along the lines.

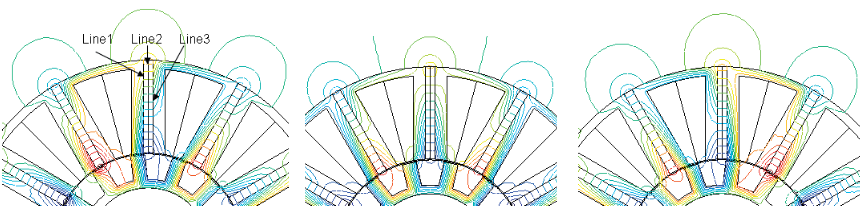

(a) (b) (c)

Fig. 8-11 (a) Zero position (b) 6.5 degree position (c) 13 degree position

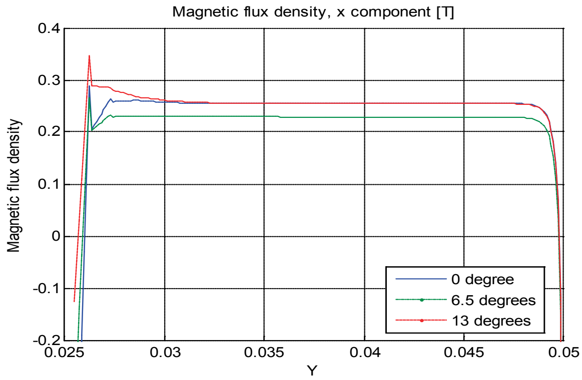

(a)

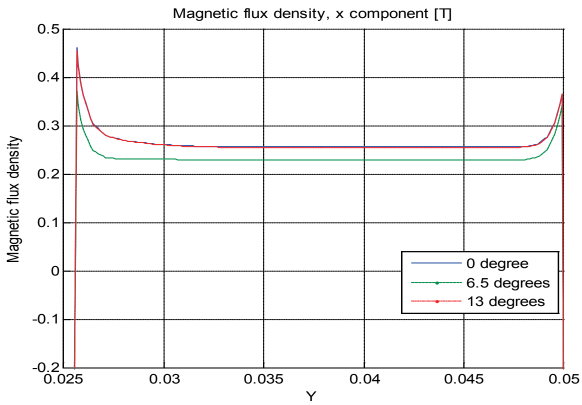

(b)

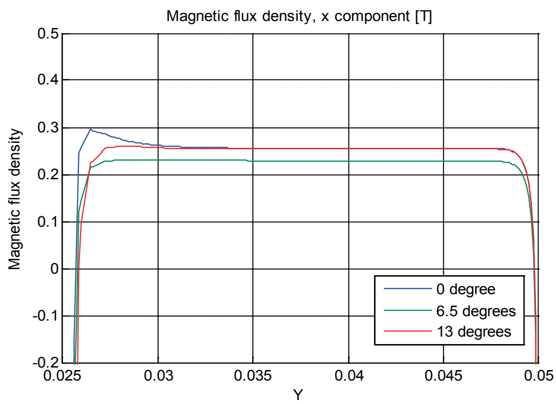

(c)

Fig. 8-12 X components of the flux densities in the magnet at different positions along (a) Line 1 (b) Line 2 (c) Line 3

It is observed that the flux in the magnets is evenly distributed in the magnet except at the inner and outer boundary edges. And the values are dependent on the rotor position. Here the average flux density (*x* component) along the middle line is employed as B_m. and its value as function of the rotor position is shown in Fig. 8-15.

8.9.2 Evaluation of B_c

The B_c value is investigated with only stator current by setting the magnet as free space. These three phase currents are rotor position dependent and determined by (8.23).

$$
\begin{aligned}
I_a &= \sqrt{2} I_{ph} \sin\left(P_r \theta - \pi/2\right) \\
I_b &= \sqrt{2} I_{ph} \sin\left(P_r \theta - 7\pi/6\right) \\
I_c &= \sqrt{2} I_{ph} \sin\left(P_r \theta + \pi/6\right)
\end{aligned}
\tag{8.23}
$$

Fig. 8-13 shows the flux distributions in the magnet when θ is at 0, 6.5 and 13 mechanical degrees, respectively. Fig. 8-14 presents the *x* component of the flux density along the three lines. The flux is also evenly distributed in the magnet except at its inner and outer boundary edges and the flux density varies at different rotor positions. For simplicity, the average flux density along the middle line is employed as B_c, and its value as function of the rotor position is presented in Fig. 8-15.

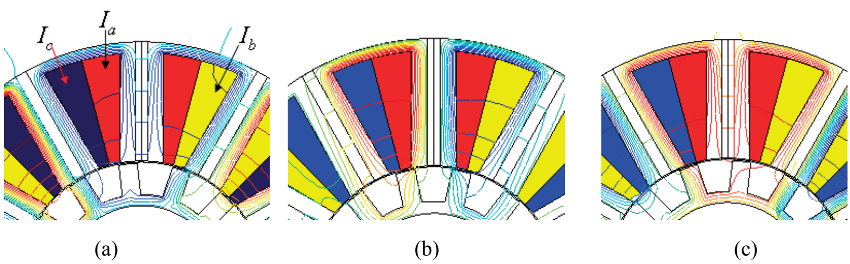

Fig. 8-13 (a) Zero position (b) 6.5 degree position (c) 13 degree position

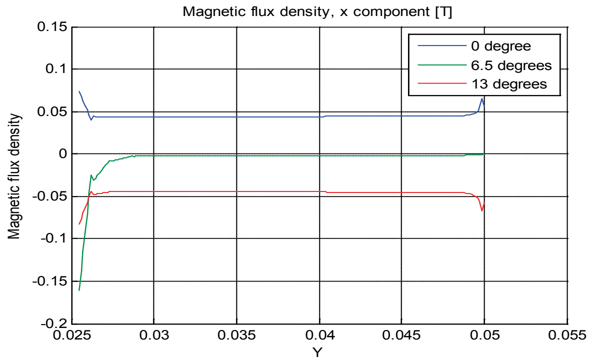

(a)

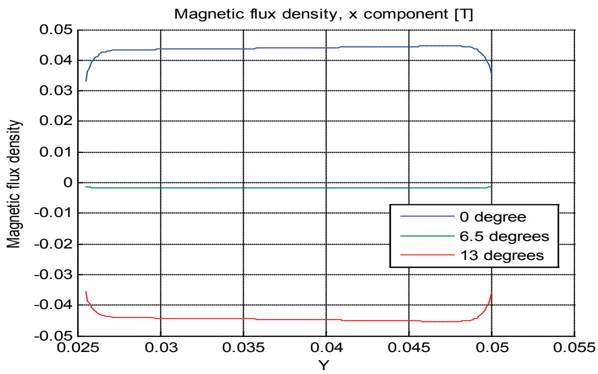

(b)

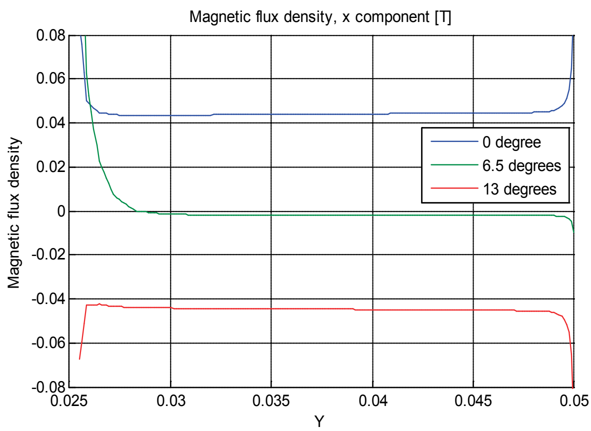

(c)

Fig. 8-14 X components of the flux densities in the magnet at different positions along (a) Line 1 (b) Line 2 (c) Line 3

It is observed that the minimum B_m is 0.23 T, which is independent of stator current, is much higher than the peak value B_c, 0.05 T. So there is no risk of demagnetization of the magnet with the given current density.

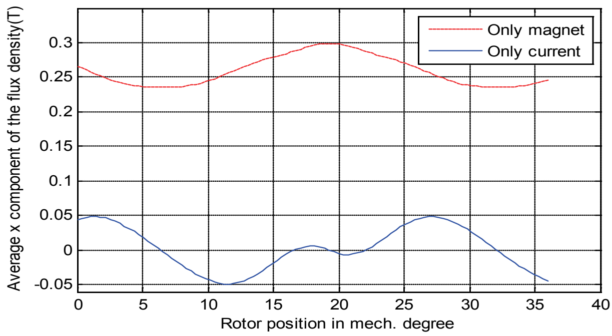

Fig. 8-15 Flux density in the magnet from FEM simulations

8.10 Conclusions

This chapter investigates a flux-switching permanent magnet with 12 stator poles and 14 rotor poles for downhole application where the ambient temperature is around 150 °C. This machine has an outer diameter of 100 mm and an active axial length of 200 mm. The investigations show that the machine can provide ~ 2.7 kW power with the output torque up to 25 Nm, an efficiency of ~ 88%, and a power factor of 0.87. The maximum temperature in the machine is around 200 °C without external cooling.

9. Machine Prototype and Measurement

The prototype of the machine presented in the previous chapter is built in the laboratory. The detail about the machine construction and the test bench are provided along with the measurement results. The machine is only tested in room temperature. Based on the measured results the machine performance at an ambient temperature of 150°C is predicted.

9.1 Prototype construction

Fig. 9-1 shows the prototype machine made in the Laboratory. In this section, the detailed construction of the machine is explained.

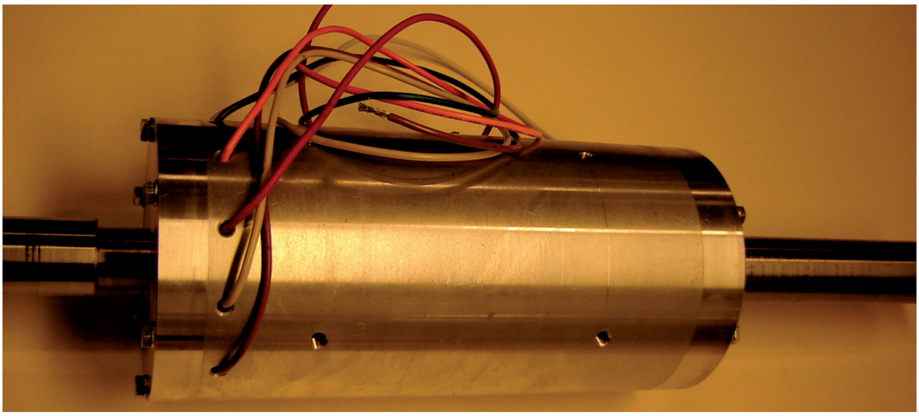

Fig. 9-1 Prototype machine

9.1.1 Stator

This machine stator consists of 12 stacked U-shaped stator laminations and 48 pieces of permanent magnets as shown in Fig. 9-2. The laminations are laser cut and the iron material is M330-35A bonding varnish [118]. The laminations dimensions are given in Fig. 9-3. The magnets are glued to the side surface of each stator lamination. After assembly the inner stator diameter increases from 51 to 51.3 mm. This results in an air gap of 0.65 mm between the stator and rotor, instead of 0.5 mm from the analytical design. How the air gap increment influences the machine performance will be presented later in the subsection of *measurements and analysis.*

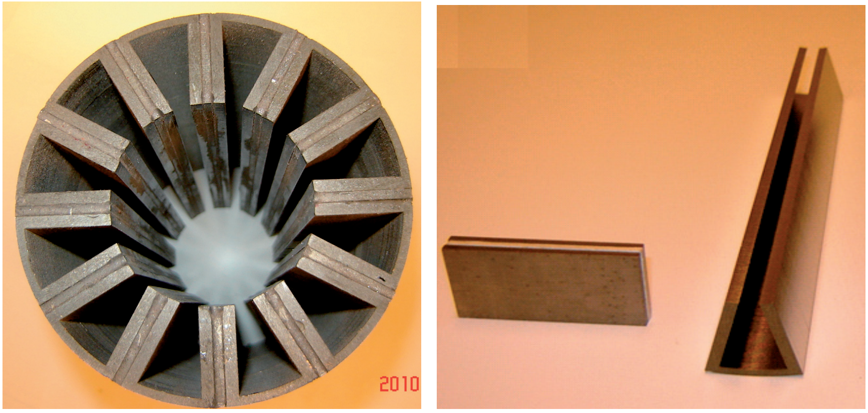

(a) (b)

Fig. 9-2 (a) Stator (b) U-shaped stacked stator lamination and permanent magnet

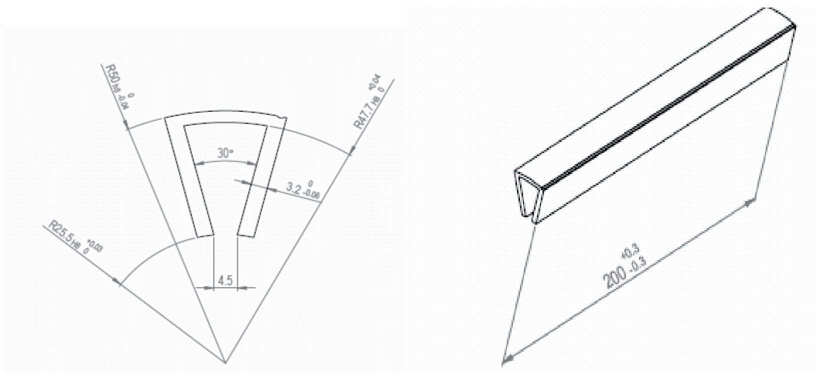

Fig. 9-3 Dimensions of the stator laminations (a) cross-section (b) stack axial length

The magnet dimensions are given in Fig. 9-4 and the material used in the prototype is *Ne-Fe-B Neorem* 593a, which has a high temperature coefficient than *Sm-Co* magnet material. Fig. 9-5 presents its characteristics. Since the machine is only going to be tested at room temperature, the machine performance influenced by the temperature coefficient is negligible. Each piece of the magnets is 50 mm long (one fourth of the machine axial length), so there are four pieces of magnets glued between two U-shaped stator stacks along the axial direction, which means that the magnets are axially segmented. Due to this, not only is the eddy current loss in the magnets partly reduced, it also makes it easier to assemble the machine due to avoiding the strong magnetic force from a big piece of magnet.

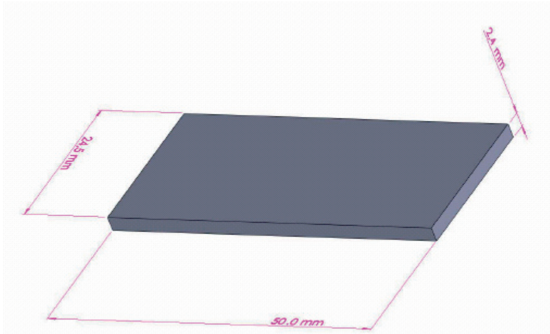

Fig. 9-4 Magnet dimensions

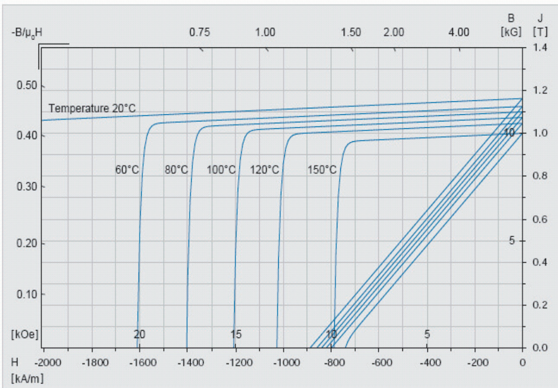

Typical demagnetization curves B(H) and J(H) at different temperatures

B_r	1.16 T	11.6 kG
$_BH_c$	890 kA/m	11.2 kOe
$_JH_c$	2100 kA/m	26.4 kOe
$(BH)_{max}$	260 kJ/m³	33 MGOe

Nominal values at 20°C

B_r	1.12 T	11.2 kG
$_BH_c$	830 kA/m	10.4 kOe
$_JH_c$	1800 kA/m	22.6 kOe
$(BH)_{max}$	240 kJ/m³	30 MGOe

Minimum values at 20°C

Fig. 9-5 Characteristics of magnet *Ne-Fe-B Neorem* 593a

9.1.2 Rotor

As mentioned previously there is rotor iron loss in this machine. In order to reduce the loss, the rotor is also made of lamination with the same iron material as the stator. Fig. 9-6 shows the stacked rotor lamination and the dimensions. Fig. 9-7 shows the rotor with the shaft.

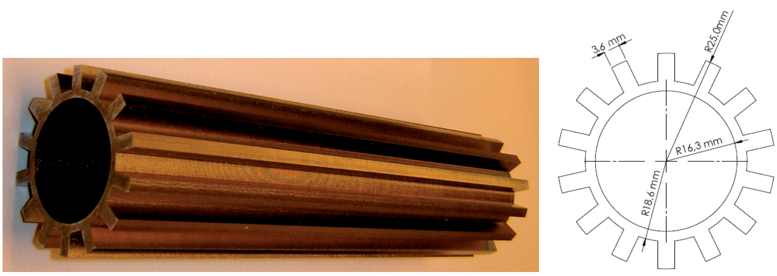

Fig. 9-6 Rotor

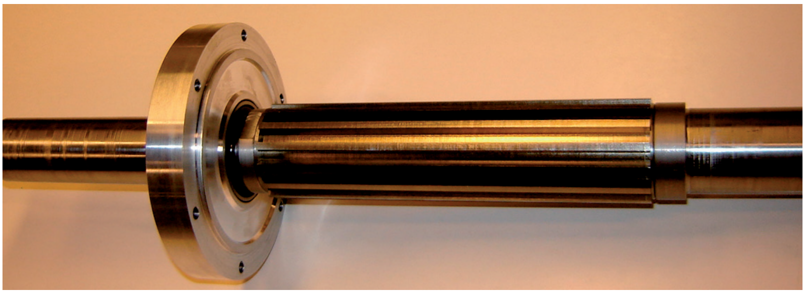

Fig. 9-7 Rotor with the shaft

9.1.3 Winding

The concentrated windings are pre-wound in the laboratory and then inset into the stator slots. According to the design requirement, the wire cross-sectional area should be 0.72 mm^2 to achieve a winding factor of 0.6. But due to the technical limitation in the laboratory, the wire used has a cross-sectional area of 0.5 mm^2, resulting in a smaller winding factor equal to 0.42 and an increased stator winding resistance of 6.0 Ω. Fig. 9-8 shows the stator with the windings and the winding connections are shown in Fig. 9-9.

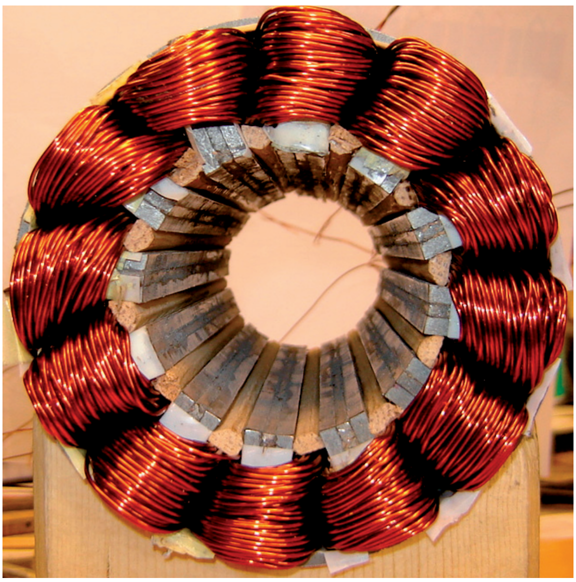

Fig. 9-8 Stator with windings

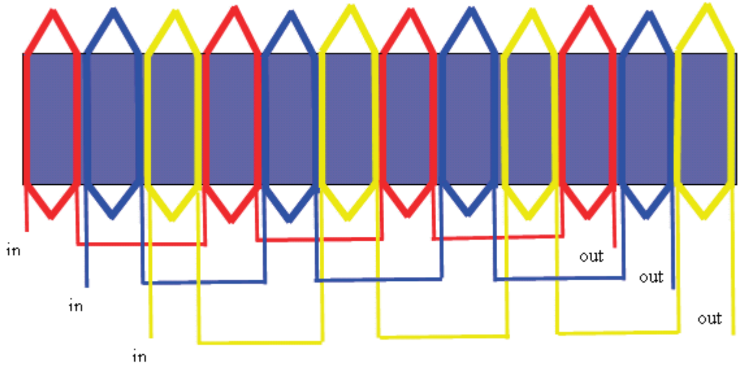

Fig. 9-9 Winding connection

9.1.4 Frame

An aluminum frame is added outside to house the stator as shown in Fig. 9-10. This frame is not an active part of the machine and has no contribution to torque production. So this part was not considered during the machine design procedure. Actually, the aluminum frame may introduce extra eddy current loss that has been studied in [91]. Opening a slot along each magnet on the frame as shown in Fig. 9-11 can partly reduced the loss. Due to the complexity of digging such a long slot inside, the frame here is made without the slots.

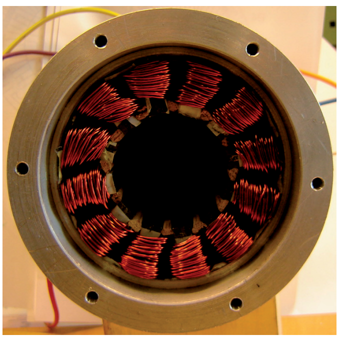

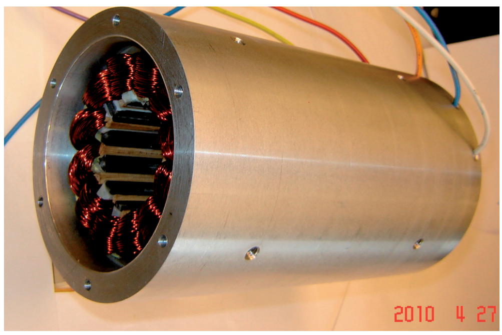

Fig. 9-10 Stator with the aluminum frame

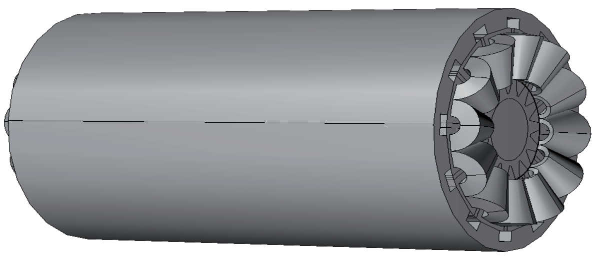

Fig. 9-11 (Original planed) slotted frame

9.2 Test bench

The machine is installed on a test bench as shown in Fig. 9-12, where the FSPM machine is connected to a DC motor with a torque meter in between. The DC machine can operate either as motor to drive the FSPM machine or as a generator to load it. During the open circuit test, the FSPM machine is driven by the DC machine for measuring the back EMF and cogging torque. During the no-load and loaded tests the FSPM machine is driven by a standard three phase converter, ACS 850 from ABB Company, which has a maximum power of 3 kW, maximum output current of 8 A and output voltage up to the input voltage of the power supply (here 400V). It can be remotely controlled from a PC as shown in Fig. 9-13.

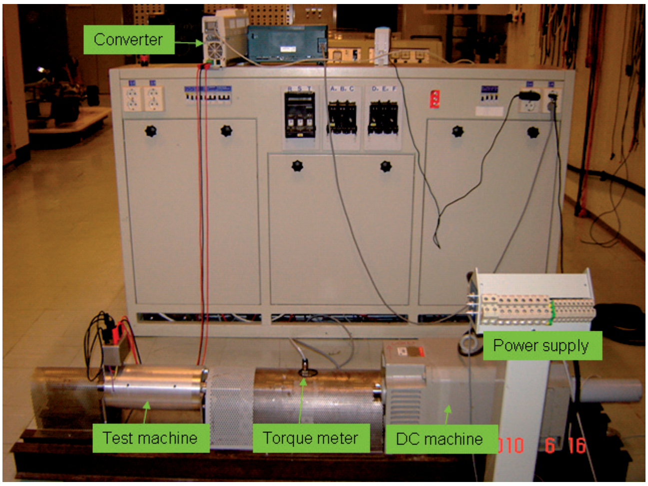

Fig. 9-12 Test bench: machine installation

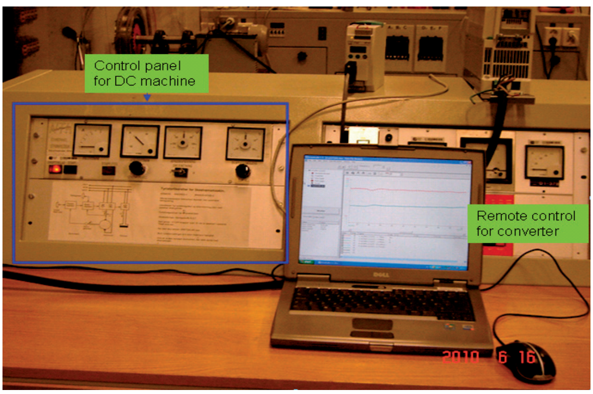

(a) (b)

Fig. 9-13 (a) Test bench: Control part (b) Converter

9.3 Measurement results and analysis

In this section, the machine inductance, resistance, back EMF, machine loss, and the output torque are measured. Since the air gap length and winding factor of the prototype have varied from the original design, the machine performance is re-investigated by 2D- FEM calculations with the new values. The re-calculated results are compared with the measured.

9.3.1 Inductance and stator resistance

The inductance and resistance are re-calculated by FEM simulations as mentioned in the previous chapter. Here the iron saturation is neglected by setting the PMs in the machine as free space.

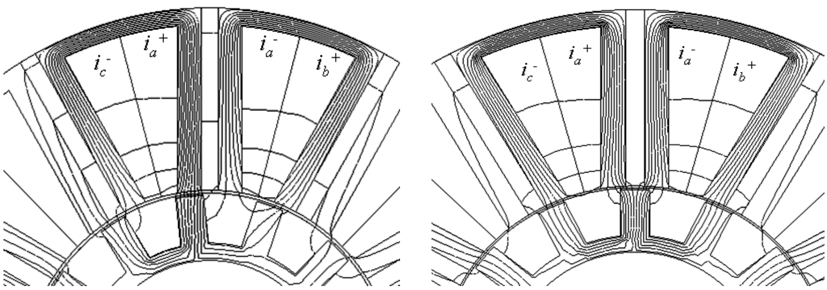

(a) (b)

Fig. 9-14 (a) *d*-position (b) *q*-position of phase *a*

Fig. 9-14 shows the flux distribution at the *d*-and *q*-position and Fig. 9-15 provides the flux variation. It is observed that the magnetic field produced by the current is in parallel with the magnetization direction of the magnets and very little part crosses the magnets, so the effective air gap is relatively small, which results in high machine inductance, as a consequence. Both the simulated and measured values are listed in Table 9-1, where the measured values are directly given from the converter after identification (*ID*) running. Due to the smaller winding factor, here the current density is 4.8 A/mm^2, more than the preciously used value of 4 A/mm^2. It is also noticed the measured inductances are slightly higher than the simulation results. The difference is most likely the leakage inductance from the end winding which is not included in the simulation result from 2D-FEM analysis. This is not verified due to the computation limitation (3D- FEM analysis is required).

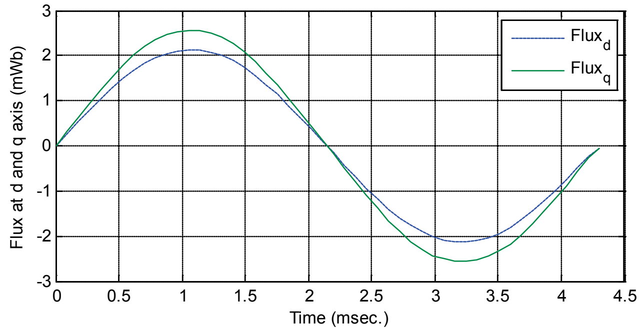

Fig. 9-15 Flux at *d* and *q*-position from FEM with setting PMs as free space

Table 9-1 Machine parameters

Parameter	FEM (neglecting saturation)	Measured
g	0.65 mm	0.65 mm
J	4.8 (A/mm^2)	4.8 A/mm^2
n_s	384	384
k_f	0.42 A	0.42 A
I_{ph}	2.4 A	2.4 A
L_d	58 mH	66 mH
L_q	70 mH	84 mH
R_s	6.25 Ω	6 Ω

9.3.2 Back EMF

Fig. 9-16 and Fig. 9-17 respectively present the FEM calculated back and the measured EMF.

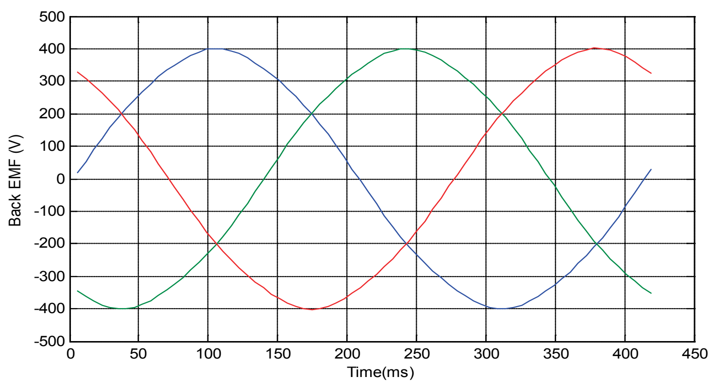

Fig. 9-16 Back EMF of the machine with an air gap of 0.65 mm

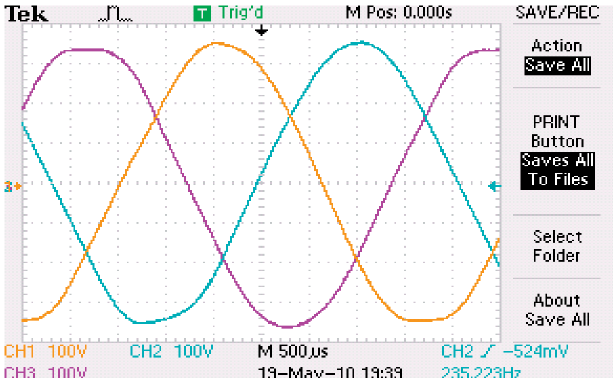

Fig. 9-17 Back EMF from measurement at speed of 1000 rpm

The measured back EMF having a peak value of 360 V is about 10% smaller than that from the FEM simulations, ~400V. The latter is from 2D-FEM simulation, in which the end effect is not taken into account. To investigate the end effect, 3D FEM simulation is required. Due to the computation limit of the available computer, this could not be successfully performed. Compared to the back EMF of the machine with g = 0.5 mm (peak value is 480 V) presented in the previous chapter, the recalculated EMF is 17% less due to the air gap increase. This implies that this machine is very sensitive to the air gap length. The smaller the air gap, the better the machine performance. In reality, the air gap length is constrained by manufacturing tolerance.

9.3.3 No load loss

No load test is carried out to investigate the no-load loss of the machine, including iron loss and magnet eddy current loss. The test machine is decoupled from the DC machine and driven by the converter. The power needed to run the machine at certain speed is the no-load loss at that speed, which can be directly read from the PC screen. Fig. 9-18 gives the measured no-load losses at different speeds.

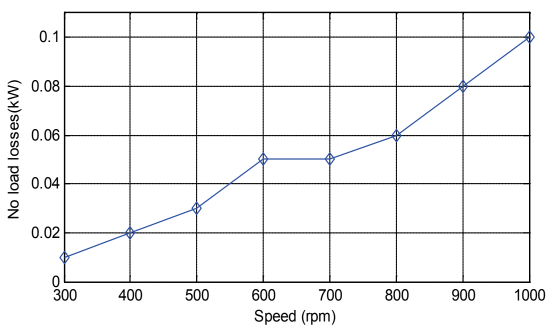

Fig. 9-18 No load losses from measurements

The iron loss and the magnet eddy current loss of the prototype are also investigated by FEM calculations as presented in the previous chapter. Table 9-2 lists the specific iron loss and the magnet eddy current loss in the magnets is around 23.4 W. The summary of the losses, 118.5W, is slightly higher than the measured no-load loss at 1000 rpm, 100W.

Table 9-2 Specific iron loss

Iron parts	Weight (kg)	Peak flux density [T]	Specific loss (W/kg)	Loss (W)
Stator tooth top /bottom	2.70	1.7 /1.3	21	56.7
Stator back iron	0.99	1.4	17	17
Rotor tooth top /bottom	0.54	1.6/1.7	28	15.1
Rotor back iron	0.37	1.4	17	6.3
Total	4.6	-----	-----	95.1

9.3.4 *Copper loss and total loss*

Fig. 9-19 presents the copper loss, no load loss and the total loss from both FEM simulations and measurement at room temperature. Since this machine has relatively low electrical loading (low winding factor and low current density), the iron loss and PM eddy current loss variations caused by the armature field are neglected. So they are assumed to be the same at the discussed current range.

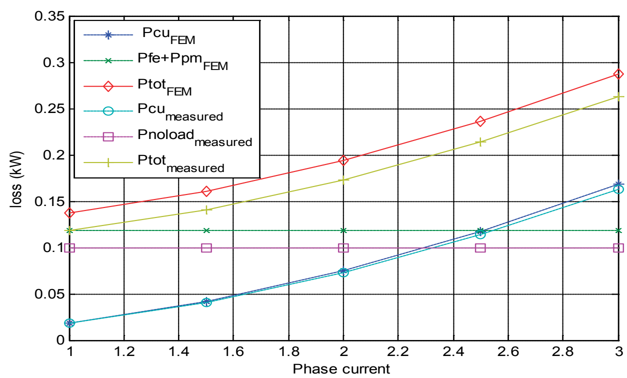

Fig. 9-19 Copper loss and total loss at room temperature and 1000 rpm

9.3.5 *Torque capability*

To measure the torque capability, the FSPM machine is mechanically coupled with the DC machine that is used as variable load by adjusting its armature current with constant field current. The torque as function of current is presented in Fig. 9-20 and compared with the simulated result. The values from 2D FEM simulations, where the end effect is neglected, are slightly higher.

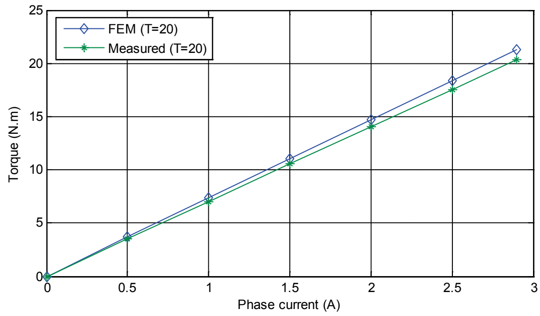

Fig. 9-20 Output torque as function of phase current

9.3.6 *Cogging torque and torque ripple*

The machine cogging torque is also measured and shown in Fig. 9-21. The display resolution is such that 1 V is equivalent to 2 Nm. The machine has a very small cogging torque, less than 0.04 Nm.

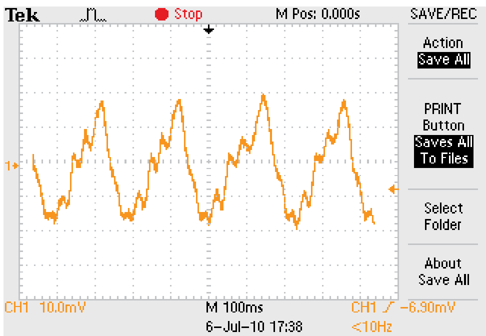

Fig. 9-21 Measured cogging torque

Fig. 9-22 presents the measured shaft torque when I_{ph}=2.4 A, as can be seen that the toque ripple is almost zero.

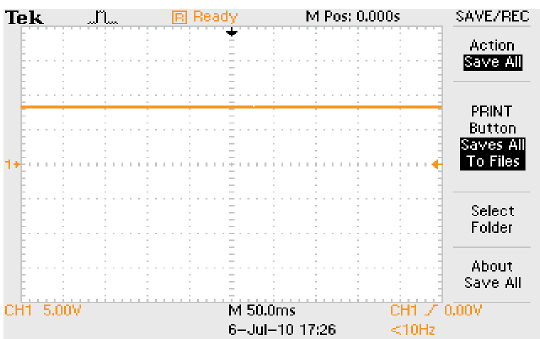

Fig. 9-22 Measured torque when I_{ph}=2.4 A

9.4 Machine torque and losses at 150 °C

In this section, the performance of the prototype machine at an ambient temperature of 150 °C and 1000 rpm is investigated based on the measured values at room temperature by neglecting the variations of the no-load loss and machine inductance at different temperatures and currents. The maximum internal temperature is assumed to be 200 °C, based on which the torque variation due to the temperature coefficient has been taken into account according to (9.1), same to the back EMF. The copper loss is calculated from (8.18).

$$T_{out\_\theta} = T_{out}\left(1+(T_\theta-20)k_{pm}\right) \tag{9.1}$$

Fig. 9-23 and Fig. 9-24 show the torque and machine losses at 200°C and 1000 rpm, respectively. They are compared with those from room temperature.

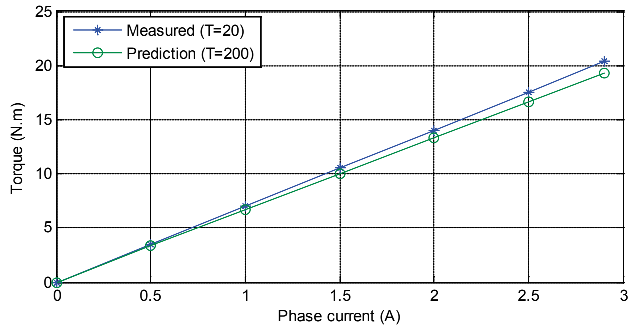

Fig. 9-23 Torque comparison (1000 rpm) at T=20°C and T=200°C

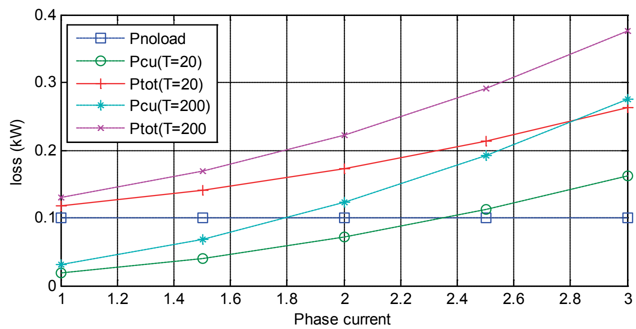

Fig. 9-24 Loss comparison (1000 rpm) at T=20°C and T=200°C

In order to find out the maximum working current of the machine, at which the maximum temperature should not be more than 200°C, the machine temperature distribution is also investigated by FEM simulations at various currents. Since it is impossible to specify the measured no-load iron loss to the different machine parts, the losses given in Table 9-2 from the FEM calculations are employed even though they are slightly higher than the measured values. The losses are assumed to be independent of current. The copper loss as function of current at T_θ =200 °C is provided in Fig. 9-24. By trying different copper loss it is found that when I_{ph} = *2.4* A (P_{cu_200}= 179W), the maximum temperature in the coil is around 200 °C as shown in Fig. 9-25. This current value is only 83% of that of the machine with k_f = 0.6 presented in the previous chapter.

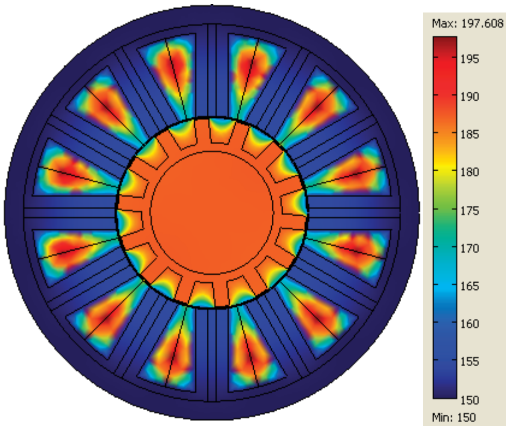

Fig. 9-25 Temperature distribution in the machine with I_{ph}=2.4 A

9.5 Result comparison

Table 9-3 lists the machine parameters at room temperature from the FEM simulations and the prototype measurements together with the predicted results at 200 °C.

Table 9-3 Summary of the machine parameters

Parameter	FEM (T_θ =20°C)	Measured (T_θ =20°C)	T_θ= 200°C
ω_m (rpm)	1000	1000	1000
g (mm)	0.65	0.65	0.65
k_f	0.42	0.42	0.42
E_{ph} (rms) (V)	288	257	244
I_{ph} (rms) (A)	2.4	2.4	2.4
L_d (mH)	58	66	66
L_q (mH)	70	84	84
R_s (Ω)	6.25	6	10.2
η %	85.4	84.9	83.7
T_{out} (Nm)	17.9	16.8	16.0
ξ_T (kNm/m^3)	10.4	9.8	9.3
PF	0.78	0.69	0.66

9.6 Conclusion

In this chapter, a prototype machine is built in the laboratory and tested in room temperature. Based on the measured values the machine performance at an ambient temperature of 150°C is investigated. The studies show that the prototype machine can provide a high torque density of 9.3 kNm/m^3, an efficiency of 83.7%, and a power factor of 0.66 with the maximum internal temperature no more than 200 °C. The machine has a relatively high inductance, which may be a benefit for applications where field-weakening is required. However, the high inductance results in a relatively low power factor compared to conventional RFPM machines. This should be taken into account when designing the control system. The machine torque capability and efficiency can be improved by increasing the winding factor and decreasing the air gap length.

10. Conclusion and future work

10.1 Conclusion

The current standard electrical downhole machine is the induction machine which has relatively low efficiency. With the development of advanced power electronic technologies and applications of high temperature magnets, the PM machine is likely to become preferable for downhole applications, in which the outer diameters are limited by well sizes and the axial lengths can be relatively long. Due to the harsh HPHT condition downhole and the extremely high cost for the replacement in a failure situation for offshore applications, the reliability of any downhole machine is demanded to be high, while high torque density, high efficiency and good controllability are also desired.

Concerning the demand for highly reliable machines, three types of robust machine concepts, IM, PMSM and SRM, are firstly reviewed. It is concluded that the PMSM offers the best power density, efficiency and controllability. This permits a high power machine with small volume, which is preferable for downhole application. Whilst the IM features the best reliability at low production cost, but it has inherently lower efficiency and torque density than the PMSM. Moreover, a complicated and expensive field-oriented control is required to reach high power. The SRM is comparable in power density and efficiency with the IM, but inferior in the others.

The PMSM is classified into RFPM, AFPM and TFPM machines according to the flux direction in the air gap. Each of them has many construction variations depending on specific applications. In the considered case for downhole applications with a speed of 1000 rpm, this thesis has studied the conventional RFPM machine, multi-stage AFPM and three-phase TFPM machines in details by analytical approach. Their reliability, torque density, efficiency and power factor are compared. The presented investigation results show that the RFPM machines have a high torque/ power density, high efficiency and reliability, and therefore present the best characteristics for downhole applications. The multi-stage AFPM machines have a low torque density and low efficiency, and are not suitable for the downhole applications. This is mainly due to the relatively large end winding existing in each stage and the small radial space confining the active winding length. A high-pole TFPM machine may compete with the RFPM machine, but its low power factor limits the machine to very low-speed applications (This is not studied in this thesis).

The RFPM machine can be further categorized into rotor-PM and stator-PM machines. The former is most popular and has several magnet arrangements. Disregarding the different rotor PM arrangements, they can offer the common advantage of high torque density and high efficiency, and some of them have already been presented for downhole applications. However, the magnets on the rotors usually need to be protected from the centrifugal force by employing a retaining sleeve which is made of either stainless steel or non-metallic fiber. This degrades the cooling capability and hence limits the power density. The stator-PM machine with both windings and PMs located in the stator reduces the problem. This thesis has presented the study of three different stator-PM machine topologies, DSPM, FRPM and FSPM machines. Among them the FSPM machine topology presents the highest torque capability thanks to the bipolar flux variation in the phase coils and the flux focusing, whilst the unipolar flux variation in the DSPM machine and the limited air-gap flux density by magnet remanence in the FRPM machine result in a lower torque density than the FSPM machine. The investigations indicate that the FSPM has high reliability, high torque /power density, and relatively high efficiency, and therefore presents promising potential for downhole applications as an alternative to rotor-PM machine topologies.

Due to the doubly salient construction, the FSPM machine performance is very sensitive to the combination of the stator pole and rotor pole numbers. After reviewing various FSPM machine constructions, two FSPM machines, which are 12/10 and 12/14 pole machines, have been selected for investigation based on FEM simulations because both machines have a symmetrically sinusoidal back EMF and high torque. In this thesis, the two machines have been investigated analytically and the design parameters have also been studied for both machines with the same stator and winding arrangement. Two prototype machines were built and tested. The research results show the 12/14 machine can provide higher torque density with the same copper loss and less torque ripple.

Typically FSPM machines are often designed with the stator back thickness, magnet thickness, stator slot opening, stator tooth width and rotor tooth width chosen to be the same as one fourth of the stator pole pitch. This method was originally developed for the design of a 12/10 pole machine. Such FSPM machines usually have highly saturated stator iron teeth, which is beneficial for the 12/10 pole machines to improve their output torques. But for a 12/14 pole machine, the high saturation leads to a reduction of the output torque due to the high flux leakage between the stator and rotor. In this thesis, a simplified lumped parameter magnetic circuit model is newly introduced to analytically design a high-torque, three-phase FSPM machine, and a design procedure of how to figure out the optimal design parameters is also presented. The designed machine with a diameter of 100 mm and axial length of 200 mm is verified by FEM simulations.

The performance of the designed machine is further investigated in the thesis for downhole applications where the ambient temperature is assumed to be 150 °C and the maximum temperature in the machine should not be over 200 °C limited by both the PM material and winding insulation without external forced cooling. To verify the results, a machine prototype was built in the laboratory and tested at room temperature. Thereafter, the performance of the prototype machine at high ambient temperature has also been predicted. Due to the technical limitation in the workshop, the prototype machine has a slightly larger air gap and smaller winding factor than the analytically designed one, which causes the degradation in the machine performance.

The investigations carried out in this thesis show that the reliable 12/14 pole FSPM machine can provide a high torque/ power density, relatively high efficiency with small torque ripple. However, this machine has a relatively high inductance that leads to a lower power factor than conventional RFPM machines.

In short, the RFPM machines are the best for most downhole applications, particularly for high-speed applications. Among them the rotor-PM machine topology is a better choice from the efficiency-stand point. While considering machine reliability, the FSPM machine is a promising candidate with a slight compromise on efficiency and power factor.

10.2 Future work

This thesis presents comparisons among different machine prototypes for general downhole applications, in which RFPM machines are recommended for downhole applications. However, choosing between the conventional rotor-PM machine topology and the FSPM machine topology is significantly requirement dependent and detailed studies between them are not performed in this thesis. In the future, this should be investigated for specific applications where the FSPM machine may be beneficial.

Since there is only steel on the rotor, a FSPM machine has more freedom for the rotor design. This may be beneficial for certain downhole applications, which should be studied in the future.

This prototype machine has only been tested in room temperature. The next step is to test it at a high temperature environment to verify the predicted results.

Appendix A: Calculation of air-gap permeances

A1. Flux distribution

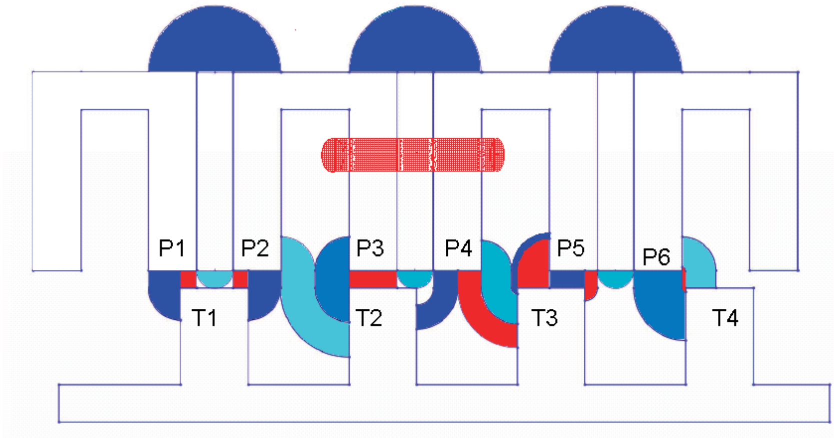

Fig. A-1 General approximation of the flux distribution in the air gap

$$P_{gol} = 0.26\mu_0 L + \mu_0 \frac{L}{\pi}\ln\left(1+\frac{D_o\pi - P_s l_{pm}}{l_{pm}P_s}\right) + \mu_0 \frac{L}{\pi}\ln\left(1+\frac{2\left(D_o\pi - l_{pm}P_s\right)}{D_o\pi + l_{pm}P_s}\right)$$

$$P_{g11} = \frac{\mu_0 L\left(\tau_r + W_{st} - \tau_s\right)}{g} + \frac{2\mu_0 L}{\pi}\ln\left(1+\frac{\pi(\tau_s - \tau_r)}{2g}\right)$$

$$P_{pm} = \frac{\mu_{pm}\mu_0 L W_{pm}}{l_{pm}}$$

$$P_{gil} = 0.26\mu_0 L$$

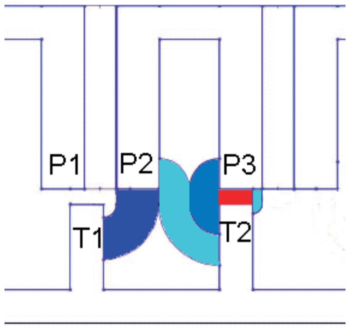

Fig. A-2 Flux distribution approximation between P2 and T1 when $W_{rt}+W_s+W_{rt}<\tau_r$ and between P3 and T2 when $W_{rt}<W_{st}$

$$P_{g21}=\begin{cases}\dfrac{\mu_0 L\left(W_{rt}+W_s+W_{st}-\tau_r\right)}{g}+\dfrac{2\mu_0 L}{\pi}\ln\left(1+\dfrac{\pi(\tau_r-W_s-W_{rt})}{2g}\right) & \text{when } W_{rt}+W_s+W_{st}\geq\tau_r \text{ (see Fig. A-1)}\\ \\ \dfrac{2\mu_0 L}{\pi}\ln\left(1+\dfrac{\pi W_{st}}{\pi\left(\tau_r-W_{rt}-W_s-W_{st}\right)+2g}\right) & \text{when } W_{rt}+W_s+W_{st}<\tau_r \text{(see Fig. A-2)}\end{cases}$$

$$P_{g32}=\begin{cases}\dfrac{\mu_0 L W_{st}}{g}+\dfrac{\mu_0 L}{\pi}\ln\left(1+\dfrac{\pi W_s}{g}\right) & \text{when } W_{rt}\geq W_{st} \text{ (See Fig. A-1)}\\ \\ \dfrac{\mu_0 L W_{rt}}{g}+\dfrac{\mu_0 L}{\pi}\ln\left(1+\dfrac{\pi W_s}{g}\right)+\dfrac{2\mu_0 L}{\pi}\ln\left(1+\dfrac{\pi(W_{st}-W_{rt})}{2g}\right) & \text{when } W_{rt}<W_{st} \text{ (See Fig. A-2)}\end{cases}$$

The rotor tooth width determined by (7.9) can not be wider than $W_{st}+l_{pm}$ when c_s (the maximum considered value 0.35) is less than 0.43, so P_{g42} is calculated by :

$$P_{g42}=\frac{2\mu_0 L}{\pi}\ln\left(1+\frac{\pi W_{st}}{\pi(l_{pm}+W_{st}-W_{rt})+2g}\right)$$

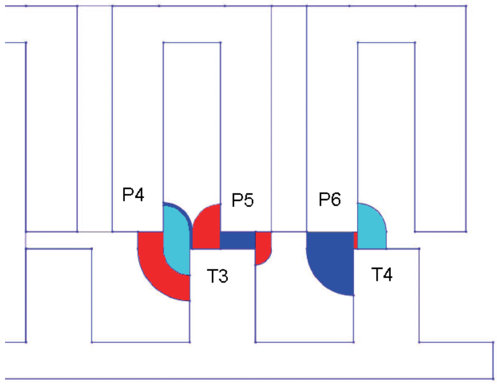

Fig. A-3 Flux distribution approximation in the air gap between P4 and T3, between P5 and T3 and between P6 and T4

when τ_s- τ_r >W_s/2

$$P_{g43} = \begin{cases} \dfrac{2\mu_0 L}{\pi}\ln\left(1+\dfrac{\pi W_{st}}{\pi(\tau_r - 2W_{st} - l_{pm}) + 2g}\right) + \dfrac{2\mu_0 L(\tau_r - 2W_{st} - l_{pm})}{\pi(\tau_r - 2W_{st} - l_{pm}) + 2g} & \text{when}\, \tau_s - \tau_r \le \dfrac{W_s}{2} \ \text{(see Fig. A-1)} \\ \dfrac{2\mu_0 L}{\pi}\ln\left(1+\dfrac{\pi W_{st}}{\pi(\tau_r - 2W_{st} - l_{pm}) + 2g}\right) + \dfrac{2\mu_0 L(\tau_r - 2W_{st} - l_{pm})}{\pi(\tau_r - 2W_{st} - l_{pm}) + 2g} & \\ \quad + \dfrac{2\mu_0 L}{\pi}\ln\left(1+\dfrac{\pi(\tau_s - \tau_r - \frac{W_s}{2})}{\pi(\tau_r - 2W_{st} - l_{pm}) + 2g}\right) & \text{when}\, \tau_s - \tau_r > \dfrac{W_s}{2} \ \text{(see Fig. A-3)} \end{cases}$$

$$P_{g53}=\begin{cases}\dfrac{\mu_0 L\left(\tau_r+W_{rt}-\tau_s\right)}{g}+\dfrac{2\mu_0 L}{\pi}\ln\left(1+\dfrac{\pi\left(\tau_s-\tau_r\right)}{2g}\right)+\dfrac{2\mu_0 L}{\pi}\ln\left(1+\dfrac{\pi\left(\tau_s+W_{st}-\tau_r-W_{rt}\right)}{2g}\right)+\\ \dfrac{\mu_0 L}{\pi}\ln\left(1+\dfrac{2\pi\left(\frac{1}{2}W_s+\tau_r-\tau_s\right)}{\pi\left(\tau_s-\tau_r\right)+2g}\right) \qquad \text{when}\,\tau_s-\tau_r\le W_s/2 \text{ (See Fig. A-1)}\\ \\ \dfrac{\mu_0 L\left(\tau_r+W_{rt}-\tau_s\right)}{g}+\dfrac{2\mu_0 L}{\pi}\ln\left(1+\dfrac{\pi W_s}{4g}\right)+\dfrac{2\mu_0 L}{\pi}\ln\left(1+\dfrac{\pi\left(\tau_s+W_{st}-\tau_r-W_{rt}\right)}{2g}\right)\\ \text{when}\,\tau_s-\tau_r>W_s/2 \text{ (See Fig. A-3)}\end{cases}$$

$$P_{g64}=\begin{cases}\dfrac{2\mu_0 L}{\pi}\ln\left(1+\dfrac{\pi W_{st}}{(\pi(2\tau_r+W_s-2\tau_s)+2g}\right)+\dfrac{2\mu_0 L(2\tau_r+W_s-2\tau_s)}{\pi(2\tau_r+W_s-2\tau_s)+2g}\\ +\dfrac{2\mu_0 L}{\pi}\ln\left(1+\dfrac{\pi(\frac{1}{2}W_s-2\tau_r-W_s+2\tau_s}{\pi(2\tau_r+W_s-2\tau_s)+2g}\right) \qquad \text{when}\,\tau_s-\tau_r\le\dfrac{W_s}{2} \text{ (See Fig. A-1)}\\ \\ \dfrac{\mu_0 L(2\tau_s-2\tau_r-W_s)}{g}+\dfrac{2\mu_0 L}{\pi}\ln\left(1+\dfrac{\pi(W_{st}+W_s+2\tau_r-2\tau_s)}{2g}\right)\\ +\dfrac{2\mu_0 L}{\pi}\ln\left(1+\dfrac{\pi W_s}{4g}\right) \qquad \text{when}\,\tau_s-\tau_r>\dfrac{W_s}{2} \text{ (See Fig. A-3)}\end{cases}$$

Appendix B: Symbols and Abbreviations

Symbols

a	Machine phase
A_m	Magnet surface area
A_{cu}	Copper area
b	*Machine phase*
B_{Fe}	*Peak flux density in iron part*
B_g	Flux density in air gap.
B_{g1}	Fundamental flux density in air gap
B_r	Magnet remanence
B_{sat}	Iron saturation flux density
B_t	Average flux density in the top of stator teeth.
c	*Machine phase*
c_s	*Ratio of stator tooth to stator pole pitch*
D_o	Machine outer diameter
E_{ph}	*rms* value of phase voltage
f_e	Electrical frequency
F_{pm}	Magnet MMF
F_s	Slot MMF
g	Airgap length
G_{Fe}	Iron part weight
h_m	Magnet thickness
H_b	Back iron width
H_c	Magnet coercivity
H_s	Tooth opening
H_{rb}	Rotor back iron thickness
H_{sb}	Stator back iron thickness
H_t	Tooth height
i	Current
I_d	*d*-axis current

I_q	q-axis current
I_{ph}	*rms* value of phase current
J	Current density
k_c	Carter's coefficient
k_f	Winding fill factor
k_{pm}	Magnet temperature coefficient
k_t	Machine constant
k_σ	Flux leakage factor or fringing factor
l_a	Machine axial length without back iron of AFPM machines
l_{cu}	Total winding length
l_{ea}	Axial length of end winding
l_{end}	End winding length
$l_{end\text{-}RF}$	End winding length of RFPM machines
$l_{end\text{-}NN}$	End winding length of NN-type AFPM machines
$l_{end\text{-}NS}$	End winding length of NS-type AFPM machines
l_m	Magnet depth
l_{ns}	Total axial length of a NS-type AFPM machine
l_{pm}	Magnet thickness
L	Machine active axial length
L_d	Inductance in d-axis
L_q	Inductance in q-axis
L_{tot}	Total machine length
L_s	Phase inductance
m	Phase number
n_{coil}	Number of turns in one coil
n_s	Number of turns in one phase
n	Stage number
N_s	Number of turns
p	Pole number
P	Power
P_{cu}	Copper loss

PF	Power factor
P_{Fe}	Iron loss
P_g	Air-gap permeance
P_{gab}	Air-gap permeance between stator tooth P_a and rotor tooth T_b
P_{gil}	Magnet inner air-leakage permeance
P_{gol}	Magnet outer air-leakage permeance
P_{lk}	Leakage permeance
P_{pm}	Magnet permeance
P_r	Rotor pole number
P_{rb}	Rotor back permeance
P_{rt}	Rotor tooth permeance
P_s	Stator pole number
P_{sb}	Stator back permeance
P_{st}	Stator tooth permeance
q	Slots per pole per phase
R_g	Air-gap reluctance
R_{so}	Radius of stator
S	Electrical loading
S_{in}	Apparent power
t	Time
T	Torque
T_θ	Temperature
W	Specific loss factor
W_c	co-energy
W_{pm}	Magnet width
W_{rt}	Rotor tooth width
W_s	Slot opening
W_{st}	Stator tooth width
$W_{st\text{-}total}$	Summary of the total stator tooth width
α_{cu}	Copper temperature coefficient

α_{pm}	Magnet coverage
α_{tooth}	Tooth width in radian
λ	Ratio of stator outer diameter to inner diameter
τ_r	Rotor pole pitch
τ_s	Stator pole pitch
τ_{slot}	slot pitch
ω_e	Electrical angular speed
θ	Mechanical angle
$\theta_{\tau r}$	Rotor pole pitch in mechanical angle
ω_m	Machine synchronous angular speed
μ_0	Permeability of free space
μ_{pm}	Magnet relative permeability
ξ_T	Torque density
$\psi_{d\text{-}max}$	Peak flux-linkage at *d*-axis
$\psi_{q\text{-}max}$	Peak flux-linkage at *q*-axis
ψ_{pm}	Flux linkage from magnet only
$\Phi_{d\text{-}max}$	Peak flux at *d*-axis
$\Phi_{\max}$	Peak flux value
Φ_{pm}	Flux produced by magnet only
$\Phi_{q\text{-}max}$	peak flux at *q*-axis

Abbreviations

AF	Axial flux
AFPM	Axial flux permanent magnet machine
BHA	Bottom-hole assembly
BLDC	Brushless direct current machine
DOWS	Downhole oil/water separation
DSPM	Doubly salient permanent magnet
EMF	Electromotive force
ESP	Electrical submersible pump
FEM	Finite element method

FRPM	Flux-reversal permanent magnet
FSPM	Flux-switching permanent magnet
HPHT	High pressure and high temperature
HPU	Hydraulic power unit
IM	Induction machine
MMF	Magneto-motive force
PCP	Progressing cavity pump
PDM	Positive displacement motor
PM	Permanent magnet
PMDC	Permanent magnet direct current
PMSM	Permanent magnet synchronous machine
rms	Root mean square
RF	Radial flux
RFPM	Radial flux permanent magnet
SRM	Switched reluctance machine
SSV	Subsurface valve
TF	Transverse flux
TFPM	Transverse flux permanent magnet
VSD	Variable speed drive
2D	Two-dimensions
3D	Three-dimensions

References

[1] Anyuan Chen, Ummaneni, R.B., Nilssen, R., Nysveen, A. " Review of electrical machine in downhole application and the advantages", in the proceeding of *EPE-PEMC 2008*, 1-3 Sep., 2008, Poznan, Poland.

[2] Anyuan Chen, Robert Nilssen and Arne Nysveen, "Performance comparisons among radial flux, multi-stage axial flux and three-phase transverse flux PM machines for downhole applications", in the proceeding of *IEMDC2009*, 6-9, May,2009, Miami, USA.

[3] Anyuan Chen, Njål Rotevatn, Robert Nilssen and Arne Nysveen, "Characteristic Investigations of a New Three-Phase Flux-Switching Permanent Magnet Machine by FEM Simulations and Experimental Verification" in the proceeding of *ICEMS2009*,15-18, Nov., 2009 Tokyo, Japan.

[4] Anyuan Chen, Robert Nilssen and Arne Nysveen, "Performance comparisons among radial flux, multi-stage axial flux and three-phase transverse flux PM machines for downhole applications", *IEEE Trans. Ind. Appl*., vol 46, No.2, pp 779-789.

[5] Anyuan Chen, Robert Nilssen and Arne Nysveen, "Analytical design of a high-torque Flux-Switching Permanent magnet machine by a Simplified Lumped parameter magnetic circuit model", in the proceeding of *ICEM 2010*, 6-8, Sep. 2010, Rome, Italy.

[6] Anyuan Chen, Robert Nilssen and Arne Nysveen, "Investigation of a Three-Phase Flux-Switching Permanent Magnet Machine for Downhole Applications ", in the proceeding of *ICEM 2010*, 6-8, Sep. 2010, Rome, Italy.

[7] "World Energy Lookout 2008", OECD/IEA, ISBN 978-92-64-04560-6

[8] "Oil and Gas Industries Technology master plan", European oil and gas innovation forum, February 2004.

[9] www.electricwell.com

[10] Ivar Sandrea and Rafael Sandrea, "Global Oil Rederves – Recovery factors Leave Vast Target fpr EOR Technology", Oil and Gas Journal, part 1: Novermber 05 and part 2: Novermber 12, 2007.

[11] "High Volume Down-Hole Progressing Cavity Pumps with Electrical Submersible Motors", R&M energy systems, a unit of tobbins and myers inc, Paper 18, ESP WORKSHOP, 1998

[12] Roy Fleshman and Harryson Obren Lekic, "Artificial lift for High-Volume Production", Oil review, spring 1999.

[13] Tom Proehl and Fred Sabins, "Drilling and completion gaps for HPHT wells in deep water final repor", 21, June, 2006.

[14] Ron Bates, Charlie Cosad, Lance fielder, Alex Kosmala, Steve Hudson, George Romero and Valli Shanmugam, "Taking the Pulse of Producing Wells-ESP Surveillance", 2004.

[15] John A Veil, Bruce G. Langhus and Stan Belieu, "Feasibility Evaluation of Downhole Oil/Water separator (DOWS) Technology", report for U.S department of energy, office of fossil energy and national petroleum technology office, January 1999.

[16] Jesus R. Rodriguez, Fathi Finaish, Shari Dunn-Norman, "Parametric study of Motor/Shroud Heat Transfer Performance in an Electrical Submersible Pump", Transactions of the ASME, Vol.122, September 2000.

[17] William D. Holmes, Monty D. Corbett, Daniel B. Wells, "Successful Downhole Oil Water Separator Installation", 2003 ESP Workshop, May 9, 2003.

[18] "Downhole gas compression", PTAC technical information session, 27, November 2003.

[19] Dan Turner, Philip Head and Mike Yuratich, "New DC motor for Downhole Drilling and Pumping Applications", Society of petroleum engineers paper 68489, March 2001, Houston, Texas.

[20] Ummaneni Ravindra Babu, Nilssen Robert and Brennvall, J.E, "Force Analysis in Design of High Power Linear Permanent Magnet Actuator with Gas Springs in Drilling Applications", Electric Machines & Drives Conference, 2007, *IEMDC'07*, IEEE International.

[21] D.R Turner, T.W.R Harris, M. Slater, M.A. Yuratich and P.F. Head, "Electric Coiled Tubing: A Smart CT Drilling System", Society of petroleum engineers paper 52791, March 1999, Amsterdam, Holland.

[22] Timothy F. Price, "Development of a High-Pressure/High-Temperature Downhole Turbine Generator", Dexter Magnetic Technologies Inc., DE-FC26-05NT42655, March 27, 2007.

[23] J.R.Smith, D.M.Grant, A-AI-Mashgari and R.D.Slater, "Operation of subsea electrical submersible pumps supplied over extended length cable systems*", IEE Proc.-Electr, Power Appl*., Vol. 147, No. 6, November 2000.

[24] Bernardo Maldonado, ""Extreme" wells: Meeting the Next big Challenge for HPHT completions", *Baker oil tools magazine*, August, 2005.

[25] Wood group ESP, www.woodgroup-esp.com.

[26] M. W. Hooker, C. S. Hazelton, K. S. Kano and M. L. Tupper, "High-Temperature Electrical Insulations for EGS Downhole Equipment", Proceeding, Thirty-Fifth workshop on geothermal reservoir engineering, Stanford, California, February 1-3, 2010.

[27] N. Griffiths and S. Breit, " The world's First Wireline Retrievable Electric Submersible Pumping System" Presented at the Eropean Artificial Lift Forum, Aberdeen, Scotland, February 28, 2008.

[28] www.slb.com/~/media/Files/artificial_lift/product_sheets/.

[29] NTK-BP Technology magazine, October-November 2007, Russian, pp.27-31.

[30] www.boretscompany.ru

[31] M. Solesa and V. Sagalovskiy, "Direct Current Motors with Permanent Magnets – More Downhole Flexibility", at *MEALF* , Sultanate of Oman, 19-20, February 2007.

[32] A. Bydzan, A. Strokolist, CJ Affeld, A. Hagelaars, A. Zanimonsky, A. Mabian, Y. Nikulin, "ESPs with Permanent Magnet Motor in Salym, West Siberia", *European artificial lift forum 2008*, Aberdeen, February, 2008.

[33] Zhang Binyi, Liang Binxue, Feng Guihong and Zhuang Fuyu, "Research of Multipolar permanent Magnet Synchronous Submersible Motor for Screw pump", Proceedings of 2007 *IEEE International Conference on Mechatronics and Automation*, August 5-8, 2007 Harbin, China, pp.1011-1016, 2007.

[34] Kelly Piers, "Coping with Water from Oil & Gas Wells", Presentation, June 14, 2005.

[35] www.motioncontrol.com/index.cfm/dc-motor

[36] Dan Turner, Philip Head and Mike Yuratich, "New DC motor for Downhole Drilling and Pumping Applications", *Society of petroleum engineers,* paper 68489, March 2001, Houston, Texas.

[37] Joao S. D. Garcia, Mauricio V. Ferreira da Luz, Joao Pedro A. Bastos and Nelson Sadowski, "Transverse Flux Machines: What for?", IEEE Multidisciplinary Engineering Education Magazine, Vol. 2, NO.1, March 2007, pp 4-6.

[38] Kartik Sitapati and R. Krishnan, "Performance comparisons of radial and axial field, Permanent-magnet, Brushless Machines", *IEEE Trans. Ind. Appl*., VOL. 37, NO. 5, pp 1219-1226. September/October 2001,

[39] Andrea Cavagnino, Mario Lazzari, Francesco Profumo and Albert Tenconi, "A Comparison between the Axial Flux and the Radial Flux Structures for PM Synchronous Motors", *IEEE Trans. Ind. Appl.,* VOL. 38, NO. 6, pp 1517-1524, November/December 2002.

[40] Metin Aydin, Surong Huang and Thomas A. Lipo, "Torque Quality and Comparison of Internal and External Rotor Axial Flux Surface-Magnet Disc Machines", *IEEE Transactions industrial electronics*, VOL. 53, NO. 3, June 2006.

[41] A. Parviainen, M. Niemelä, J. Pyrhönen and J. Mantere, "Performance Comparison between Low-speed Axial-Flux and Radial-Flux Permanent-Magnet Machines Including Mechanical Constraints". pp 1695-1702.2005 IEEE

[42] Thomas A. Lipo, "Introduction to AC Machine Design", 2nd Edition, University of Wisconsin-Madison, ISBN 0-9745470-1-8I, 2004.

[43] Federico Caricchi, Fabio Crescimbini, Onorato Honorati, Giulia Lo bianco and Ezio Santini, "Performance of Coreless-Winding Axial-Flux Permanent Generator with Power Output at 400Hz, 3000 r/min", *IEEE Trans. Ind. Appl*, VOL. 34, NO.6 ,pp 1263-1269, November/December 1998.

[44] Chandur Sadarangani, "Electrical machines", ISBN 91-7170-627-5, KTH Högskoletryckeriet, August, 2000, Stockholm, Sweden

[45] W. M. Arshad, T. Bäckström and C. Sadarangani, "Analytical Design and Analysis Procedure for A Transverse Flux Machine", 2001 IEEE.

[46] S. Huang, J. Luo, F. Leonardi and T. A. Lipo, "A Comparison of Power Density for Axial Flux Machines Based on General Purpose Sizing Equations", *IEEE Transactions on Energy Conversion*, Vol.14, No.2, pp. 185-1192, 1999.

[47] G. Henneberger, M. Bork, "Development of a New Transverse Flux Motor", printed and published by the *IEE*, Savoy Place, London WCPR OBL, UK.

[48] G. Henneberger and M. Bork, " Development of a Transverse Flux Traction Motion in a Direct Drive System" in *ICEM 2000*, Helsinki, August, 2000. pp. 1457-1460.

[49] Jack F. Gieras and Michell Wing, "Permanent Magnet Motor Technology", 2nd Edition, ISBN: 0-8247-0739-7, printed in the United States of America, 2002.

[50] Ion Boldea, "Variable Speed Generators", ISBN: 0-8493-5715-2, Taylor & Francis group, 2006.

[51] Jack F. Gieras, Rong-Jie Wang and Maarten J. Kamper, "Axial Flux Permanent Magnet Brushless Machines", 2nd Edition, ISBN: 978-1-4020-6993-2, Springer, 2008.

[52] Ion Boldea and Syed A. Nasar, "The Induction Machine Handbook", ISBN: 0-8493-004-5, CRC Press LLC, 2002

[53] Z. Q. Zhu, Y. Pang, D. Howe, S. Iwasaki, R. Deodhar, and A. Pride, "Analysis of electromagnetic performance of flux-switching permanent magnet machines by non-linear adaptive lumped parameter magnetic circuit model," *IEEE Trans. Magn.,* Vol.41, No.11, pp.4277-4287, November 2005.

[54] J. Zhang, Z. Chen and M. Cheng, "Design and comparison of a novel stator interior permanent magnet generator for direct-drive wind turbines", *IET Renewable Power Generation*, December, 2007, Vol.1 pp 203-210.

[55] J. T. Chen, Z. Q. Zhu, A. S. Thomas and D. Howe, "Optimal combination of stator and rotor pole numbers in flux-Switching PM brushless AC machines", the proceeding of *ICEMS 2008*, Vol. 44 pp 4659 – 4667.

[56] Z.Q. Zhu, Y. Pang, J. T. Chen, Z. P. Xia, D. Howe, "Influence of design parameters on output torque of flux-switch permanent magnet machines", IEEE Vehicle Power and Propulsion Conference (VPPC), September 3-5, 2008, Harbin, China.

[57] W. Z. Fei and J. X. Shen, “Comparative study and optimal design of PM switching flux motors”. *UPEC’06*, 6-8 Sept. 2006, Vol.2 pp 695-699.

[58] Emmanuel Hoang, Michel Lecrivain, Mohamed Gabsi, “A new structure of a switching flux synchronous polyphased machine with hybrid excitation”, the proceeding of *Power electronics and applications, 2007* European conference, pp 1-8.

[59] Wei Hua, Ming Cheng, Z. Q. Zhu and D. Howe, “Design of flux-switching permanent magnet machine considering the limitation of inverter and flux –weakening capability”. *IEEE 2006*, pp 2403-2410.

[60] Jiangzhong Zhang, Ming Cheng and Zhe Chen, “Optimal design of stator interior permanent magnet machine with minimized cogging torque for wind power application”, *Energy Conversion and management* 49, 2008, pp 2100-2105.

[61] Wei Hua, Ming Cheng, Z. Q. Zhu and David Howe, “Analysis and optimization of back EMF waveform of a flux-switching permanent magnet motor”, *IEEE Transactions on Energy Conversion*, VOL. 23, NO. 3, September 2008, pp 727-733.

[62] Njål Rotevatn, “Design and testing of flux switched permanent magnet machines”, Master thesis, Jul. 2009, Norwegian University of Science and Technology, Trondheim, Norway.

[63] F. Feudale, A. Odorico, M. Sica, F. Caricchi, F. Giulii and F. Crescimbini, “Multi-stage Axial-flux PM machine for Direct-Drive Railway Traction Applications”, ISBN: 0-7803-8305-2.

[64] Joǎo S. D. Garcia, Mauricio V. Ferreira da Luz, Joǎo Pedro A. Bastos and Nelson Sadowski, “Transverse Flux Machines: Whar for?” *IEEE multidisciplinary engineering education magazine*, VOL. 2, NO. 1, March 2007.

[65] P. Anpalaham, “Design of Transverse flux machines using analytical calculations & finite element analysis”, Tech. licentiate thesis, Royal institute of technology, Stockholm, 2001.

[66] Y. Liao, F. Liang and T. A. Lipo, “A Novel Permanent Magnet Motor with Doubly Salient Structure”, *IEEE Trans. on Ind. Appl.,* Vol. IA-31, No. 5, Sept/Oct 1995, pp. 1069-1078.

[67] Xiaogang Luo, Dinyu Qin, Thomas A. Lipo, “A novel two phase doubly salient permanent magnet motor”, *IEEE 1996*, pp 808-815.

[68] W. Hua, Z. Q. Zhu, M. Cheng ,Y. Pang and D. Howe, “Comparison of flux-switching and double-salient permanent magnet brushless machines”, the proceeding of *ICEMS 2005*, Vol. 1 pp 165-170

[69] Y. Pang, Z. Q. Zhu, D. Howe, S. Iwasaki, R. Deodhar, A. Pride, “Comparative Study of Flux-Switching and Interior Permanent Magnet Machines”, the proceeding of *ICEMS 2007*, Oct. 8-11, Seoul, Korea.

[70] Tomy Sebastian and Gordon Slemen, “Transient Torque and Short Circuit Capabilities of Variable Speed Permanent Magnet Motors”, *IEEE Trans. Magn.,* Vol.Mag-23, NO.5, September 1987.

[71] Gordon R. Slemon, “On the Design of High-Performance Surface-mounted PM motors”, *IEEE Trans. Ind. Appl*., VOL.30, NO.1, January/February 1994.

[72] Tomy Sebastian and Gordon Slemen, “Transient modeling and Performance of Variable Speed Permanent Magnet Motors”, *IEEE Trans. Ind. Appls*, Vol.25, NO.1, January/February 1989.

[73] D. Schobinger, O. Gutfleisch, D. Hinz, K. H. Müller, L. Schultz, G. martinek, “High temperature magnetic properties of 2:17 Sm-Co magnets”, *Magnetism and Magnetic Materail* 242-245 (2002) pp 1347-1349.

[74] Christina H. Chen, Marlin S. Walmer, Michael H. Walmer, Sam Liu and G. Edward Kuhl, “Thermal Stability of Sm-TM high Temperature Magnets at 300-550°C”, *IEEE Trans. magn.*, VOL. 36. NO.5, September 2000.

[75] Yi Liu, David J. Sellmyer and Dasuke Shido, “Handbook of Advanced magnetic materials, Volume 4 Property and Applications”, ISBN 978-1402-07983-2, printed in the United States of America, Springer, 2006.

[76] É. du Trémolet de, Lacheisserie, D. Gignoux- M. Schlenker, “Magnetism Materials & Applications”, ISBN 1-4020-7223-6, printed in the United States of America, Springer, 2005.

[77] www. maurermagnetic.ch

[78] T. Oshiyama, H, Miyazaki, Y. Yamasaki and H, Hayashi, “electrical Insulation for Very High-Temperature Motors and Examples of Motor Applications,” Yashikawa Technical Review, 46, 176, pp 192-205, 1982.

[79] S. Matsumura, “New inorganic Insulaton for 350°C Induction Motor,” shiko Debki Giho, 36, 1, pp 46-47, 1991.

[80] H. Mitsui, “Progress in Japan in Electrical Insulation at High Temperatures”, *IEEE Electrical insulation magazine*, pp16-27, 1996.

[81] Alan L. Sheldrake, “Handbook of Electrical Engineering for Practitioners in the Oil, Gas and Petrochemical Industry”, ISBN 0-471-49631-6, Wiley, printed by Antony Rowe Ltd, Eastbourne, 2003

[82] WWW. Arcelormittal.com

[83] F. Deng, “Commutation_Caused Eddy-Currrent Losses in Permanent-Magnet Brushless DC Motors”, *IEEE Trans. Magn*., VOL. 33, pp 4310-4318, September.1997.

[84] H. Polender and M. J. Hoeijmakers, “Eddy-Current Losses in the Segmented Surface-Mounted Magnets of a PM Machine”, in *IEE proc. Electr. Power Appl*., VOL. 146, May 1999, pp. 261-266.

[85] A. Fukuma, S. Kanzawa, Daisuke Miyagi and N. Takahashi, “Investigation of AC Loss of Permanent Magnet of SPM Motor Considering Hysterisis and Eddy-Current Losses”, *IEEE Trans. Magn.*, VOL. 41,NO.5, May 2005.

[86] W. N. Fu and Z. J. Liu, “Estimation of Eddy-Current Loss in Permanent Magnets of Electric Motors Using Network-Field Coupled Multislice Time-Stepping Finit-Element Method”, *IEEE Trans. magn.,* VOL. 38, NO. 2, March 2002.

[87] Z. Q. Zhu, Y. Pang, J. T. Chen, R. L. Owen, D. Howe, S. Iwasaki, R. Deodhar and A. Pride, “Analysis and Reduction of Magnet Eddy Current Loss in Flux-Switching Permanent Magnet Machines”, In the proceeding of the conference *PEMD 2008* , 2-4 April 2008, York, UK.

[88] Katsumi Yamazaki, Masayuki Shina, Masashi Miwa and Jun Hagiwara, “Investigation of Eddy Current Loss in Divided Nd-Fe-B Sintered Magnets for Synchronous Motors Due to Insulation Resistance and Frequency”, *IEEE Trans. magn.,* VOL. 44, NO. 11, November 2008.

[89] Katsum Yamazaki, Yu Fukushima and Makoto Sato, “Loss Analysis of Permanent-Magnet Motors with Concentrated Windings-Variation of Magnet Eddy-Current Loss Due to Stator and Rotor Shapes”, *IEEE Trans. Ind. Appl.,* vol. 45, No.4, July /August 2009.

[90] WWW. Comsol.com

[91] Y. Pang, Z. Q. Zhu, D. Howe, S. Iwasaki, R. Deodhar, and A. Pride, “Eddy Current Loss in the Frame of a Flux-Switching Permanent Magnet Machine”, *IEEE Trans on magn.*, VOL. 42, NO. 10, October 2006.

[92] Wei Hua and Cheng Ming, “Inductance Characteristics of 3-Phase Flux-Switching Permanent Magnet Machine with Doubly-Salient Structure”, proceeding of *IPEMC 2006*, August 14-16, 2006, Shanghai, China.

[93] Fang, Z. X., Wang, Y., Shen, J. X., Huang, Z. W., “Design and analysis of a novel flux-switching permanent magnet integrated-starter-generator” , *PEMD 2008*.

[94] Arwyn S. Thomas, Z. Q. Zhu, Richard L. Owen, Geraint W. Jewell and David Howe, "Multiphase Flux-Switching Permanent-Magnet Brushless Machine for Aerospace Application", *IEEE Trans. Ind. Appl.,* vol. 45, No. 6, pp. 1971-1981, November/December 2009.

[95] Yu Chen, Z. Q. Zhu and David Howe, "Three-Dimensional Lumped-Parameter Magnetic Circuit Analysis of Single-Phase Flux-Switching Permanent-Magnet Motor", *IEEE Trans. Ind. Appl*., vol. 44, No. 6, pp. 1701-1710, November/December 2008

[96] Rajesh P. Deodhar, Svante Andersson, Ion Boldea, and Timothy J. E. Miller, "The Flux-Reversal Machine: A New Brushless Doubly-Salient Permanent-Magnet Machine", *IEEE Trans. Ind. Appl*., vol. 33, No, 4, pp. 925-934, July/August 1997.

[97] Duane Hanselman, "Brushless Permanent magnet motor design", Second Edition, ISBN 1-932133-63-1, printed in the United States of America. 2003

[98] Wei Hua and Cheng Ming, "Inductance Characteristics of 3-Phase Flux-Switching Permanent Magnet Machine with Doubly-Salient Structure", the proceeding of *IPEMC 2006*.

[99] Jacek F. Gieras, Ezio Santini and Mitchell Wing, "Calculation of Synchronous Reactances of Samll Permanent-Magnet Alternation-Current Motors: Comparison of Analytical Approach and Finite Element Method with Measurements", *IEEE Trans. Magn*. vol. 34, no.5, September 1988.

[100] Ping Zheng, Peter Thelin, Anyuan Chen and Erik Nordlund," Influence of Saturation and Saliency on the Inductacne of a Four-Quadrand Transducer Prototype Machine", *IEEE Trans. Magn.* Vol. 42, no.4, April 2006.

[101] Hans-Peter Nee, Lous Lefevre, Peter Thelin and Juliette Soulard, "Determination of d and q Reactances of Permanent-Magnet Synchronous Motors Without Measurements of the Rotor Position", *IEEE Trans. Ind.* Vol. 36, no.5, September 2000.

[102] Handbook "Kvarlitetskomponenter fra Elis Elektro AS" 1998-1999.

[103] K. T. Chau, C. C. Chan and Chunhua Liu, "Overview of Permanent-Magnet Brushless Drives for Electric and Hybrid Electric Vechicles", *IEEE Transactions on Inductrial Electronics*, vol. 55, no. 6 June 2008.

[104] I. Boldea, "Reluctance Synchronoous Machines and Drives", ISBN 0-19-859391-0, Clearendon Press, Oxford University, 1996.

[105] J. F. Gieras and N. bianchi, "Electric Motors for Light Traction", EPE journal, February, 2004, pp. 12-21.

[106] Thmos Finken and Kay Hameyer, "Design of Electric Motors for Hybtid- amd Electric-Vechile Applications", ICEMS 2009, Tokyo, November 15-18, 2009.

[107] Z. Q. Zhu and D. Howe,"electrical Machines and Drives for Electric, Hybrid, and Fuel Cell Vehicles", Proc. IEEE. Vol,95, no. 4, April 2007.

[108] M. Cheng, K. T. Chan and C. C. Chan, "Nonlinear Varying-Network Magnetic Circuit Analysis for Doubly Salient Permanent-Magnet Motors", *IEEE Trans. Magn*. vol. 36, pp.339-348, Jan. 2000.

[109] Ming Cheng, K. T. Chau and C. C. Chan, "Design and Analysis of a New Doubly Salient Permanent Magnet Motor", *IEEE Trans. Magn*. vol. 37, no.4, pp 3012-3020, July 2001.

[110] A. Thomas, Z. Q. Zhu, G. W. Jewell and D. Howe, " Flux-Switching PM Brushless Machines with Alternative Stator and Rotor Pole Combinations", *Journal of Asian Electric Vehicles*, vol. 6, no. 1, pp 1103-1109, Jun. 2008.

[111] Y. Chen, S. Chen, Z. Q. Zhu, D. Howe and Y. Y. Ye, "Starting Torque of Single-Phase Flux-Switching Permanent Magnet Motors", *IEEE Trans. Magn*. vol 42, no .10, pp 3417-3418, Oct. 2006.

[112] W. Hua and M. Cheng, "Comparative Study of 2-Phase Flux-Switching and Doubly-Salient Permanent Magnet Brushless Machines", www.paper.edu.cn.

[113] P. C. Sen, "Principles of Electric Machines and Power Electronics", 2nd, ISBN 0-471-02295-0, John Wiley & Sons, printed in USA, 1997.

[114] Peter Vas, "Sensorless Vector and Direct Toque Control", ISBN 0-19-856465-1, Oxford university press, 1998.

[115] P. Thelin and H-P Nee, "Calculation of the Airgap Flux Density of PM Synchronous Motors with Buried Magnets Including Axial Leakage and Teeth Saturation", *EMD'99*, Canterbury, United Kingdom, September 1999, pp.339-345.

[116] Richard L. Owen, Z. Q. Zhu, Arwyn S. Thomas, Geraint W. Jewell and David Howe, " Alternate Poles Wound Flux-Switching Permanent-Magnet Brushless AC Machines", *IEEE Trans. Ind. Appl*., vol. 46, no. 2, March/April 2010, pp 790-797.

[117] J. T. Chen and Z. Q. Zhu, " Influence of Rotor Pole Number on Optimal Parameters in Flux-Switching PM Brushless AC Machines by Lumped Parameter Magnetic Circuit Model", *IEMDC 2009*, May 3-6, 2009, pp 1451-1458.

[118] www. lcd_lasercut.ch

[119] www.neore.fi

[120] P. Thelin and H-P Nee, "Calculation of the Airgap Flux Density of PM Synchronous Motors with Buried Magnets Including Axial Leakage and Teeth Saturation", *EMD'99*, Canterbury, United Kingdom, September 1999, pp.339-345

[121] Anyuan Chen, "FEM Based Analysis and Optimization of a Longitudinal Flux Free-Piston Generator", X-ETS/EME-0402, Royal Institute of Technology (KTH), 2004, Stockholm, Sweden.

[122] http://www.ti.com/.